Synthesis of nickel sulfide-reduced graphene oxide for application in gas sensors

By

Boitumelo Tlhaole

Student Number: 1872377

BSc (Hons)

A dissertation submitted to the Faculty of Science at the University of the Witwatersrand, Johannesburg in fulfilment of the requirements for the degree of

Master of Science in Chemistry

Supervisor: Dr Ella C. Linganiso

Co-supervisor: Prof Neil J. Coville

Johannesburg, July 2020

DECLARATION

I, Boitumelo Tlhaole, hereby declare that the work covered in this dissertation is my original work and has not been previously submitted to any other institution of higher learning other than the University of the Witwatersrand. Moreover, I declare that any other work that has been taken from other people's work has been cited accordingly.

UNIVERSITY OF THE
WITWATERSRAND,
JOHANNESBURG

Signature:…… …… Date: 3 July 2020

DEDICATION

I dedicate this work to the One who carried me through, Mothathayotlhe.

“Morena, thušo tsa Gago

Fa ke di gopola tšotlhe

O molemo, le tlotlego

O ntsamaisitse sentle.”

AKNOWLEDGEMENTS

Firstly, I thank GOD for being the Alpha and Omega, for His grace, His faithfulness and His unending love.

I would like to extend my gratitude to my supervisors, Dr Ella Linganiso and Prof Neil Coville, for granting me this opportunity of growth and for their guidance, insights, advice and encouragement. I am also very grateful to Jessica Mhlongo, whom I had the privilege of mentoring during her honours project and whose work contributed to the completion of this dissertation. And to all the members in my research group, CATMAT, I am grateful for all the valuable input and for creating a wonderful working environment.

I am grateful to the Microscopy and Microanalysis Unit (MMU WITS) for making their facilities available and the training provided by the staff. I also would like to thank Dr Rudolph Erasmus for his assistance with Raman spectroscopy analysis from the School of Physics at the University of Witwatersrand and Mr Siyasanga Mpelane for assisting with high magnification transmission electron microscopy analysis at the University of Johannesburg.

I also extend my gratitude to Dr Messai Mamo from the Applied Chemistry Department at the University of Johannesburg for hosting me in his laboratory and for granting me an opportunity of using their gas sensing system. I thank Lesego Malepe who helped me with experiments and ensured that my visit was a fruitful learning experience.

I am grateful to the National Research Foundation for funding this research and the DSI-NRF Centre of Excellence in Strong Materials for providing further financial assistance.

I am extremely grateful to the friends I made while on this journey- the brothers and sisters who have shown me kindness, love and support- Lineo Mxakaza, Bonakele Mtolo, Lebogang Mosiane, Bokome Shaku, Nndivhiseni

Ramunenyiwa, Thuli Buthelezi, Joy Masilo, Ditiro Lekgothoane, Ntongazethu Ntonga, Yongezile Mhlana, Thabo Monyatsi, Katlego Mokone, Thapelo Mofokeng, Nkosikhona Nzimande, Kelechi Lebechi and Thokozani Tsoari.

To the people who throughout the years have become family, Boitumelo Thabane, Katlego Jakgosi, Naledi Senokoane, Zizipho Xantini, Nthabeleng Hlaphisi, Puleng Phalole and Obedience Moos, thank you for your prayers, your compassion, your love, and for always reminding me of my potential and mostly importantly of God's power when pushing through was difficult.

To my spiritual family, Rev. Nomsa Mabaso, Mrs Funeka Sobantu and Miss Sinovuyo Jaxa, my parents from the Braamfontein Methodist Church, and from the cell group in Newtown, I appreciate the love, encouragement and support that you showed me throughout this journey. To the teens that I had the privilege of mentoring during my stay in Braamfontein, thank you for enriching my life and assisting my growth. Lastly, I thank the Methodist Student Society at Wits University for being 'a home away from home'.

Last but not least, to the village that has always been there, mama le papa, Mr Matsheliso and Mrs Bahedile Tlhaole le bokgaitsedi ba me, Matshedisho, Lebogang, Kgosimang and Theopilus, ke lebogela dithapelo, lorato, tshegetso le dikeletšo tsa lona. I am also very appreciative of the support and love that I have received from my sisters-in-law and my nieces and nephews. To my aunts, Mane Keneilwe Mazakaza and Mane Linda Soldaat, kea leboga ka karolo e le nang le yona mo botshelong jwa me. A special thank you to my cousins, Ntombizodwa Mazakaza, Lulama Mazakaza and Oarabile Soldaat. You have been there supporting and encouraging me from the very beginning of my tertiary studies and for that I will forever be grateful.

PRESENTATIONS

- **'Microwave synthesis of Ni_3S_2 using H_2O_2 as reducing agent'** Poster Presentation. The 9th Cross-Faculty Postgraduate Symposium, University of the Witwatersrand, Johannesburg, October 2018.
- **'Synthesis of graphene oxide using the Improved Hummers' method'** Poster Presentation. Catalysis Society of South Africa Conference, North-West University, Waterberg, November 2018.
- **'Synthesis of graphene oxide using the Improved Hummers' method'** Poster Presentation. Microscopy Society of South Africa Workshop, University of the Witwatersrand, Johannesburg, December 2018.
- **'The synthesis of reduced graphene oxide from graphite powder'** Poster Presentation. Centre of Excellence Annual Student Workshop, University of the Witwatersrand, Johannesburg, May 2019.
- **'Microwave synthesis of Ni_3S_2 nanostructures: solvent influence'** Poster Presentation. The South African Institute of Physics Conference, University of Venda, Polokwane, July 2019.
- **'Ni_3S_2-rGO composites as a possible ammonia sensing material'** Oral Presentation. The 10th Cross-Faculty Postgraduate Symposium, University of the Witwatersrand, Johannesburg, September 2019.
- **'The synthesis or reduced graphene oxide'** Oral Presentation. The Microscopy Society of South Africa Conference, University of Cape Town, Langebaan, December 2019.

AWARDS

- Postgraduate Merit Award (**February 2019 – December 2019**), University of the Witwatersrand.
- Microscopy Society of South Africa Student Grant (**December 2019**).

PUBLICATIONS

1. Microwave assisted reduction of GO to rGO; the effect of a reducing agent

   B Tlhaole, JT Mhlongo, NJ Coville, EC Linganiso (**in preparation**)

2. Ethanol gas sensing using Ni_3S_2-rGO composites synthesized via wet chemical methods

   B Tlhaole, L Malepe, NJ Coville, MMA Mamo, EC Linganiso (**in preparation**)

ABSTRACT

The detection of toxic substances are crucial for the environment and human health. Recently, composite structures have shown great capabilities in detecting these toxic substances due to their unique chemical and physical properties. In this study, simple microwave-assisted and other wet chemical methods were used to produce nickel sulfide-reduced graphene oxide composites and applied in the detection of acetone, ethanol, methanol and toluene vapours.

Firstly, the influence of different solvents on microwave produced Ni_3S_2 structures was investigated. Water, ethanol, ethylene glycol, a mixture of water and ethanol and a mixture of water and ethylene glycol were used separately as solvents during a microwave reaction that was operated at 600 W for 6 minutes. The as-prepared materials were characterized using X-ray diffraction (XRD), Fourier transform infrared (FTIR) spectroscopy, Laser Raman spectroscopy, Transmission electron microscopy (TEM), X-ray photoelectron spectroscopy (XPS) and Brunauer-Emmett-Teller (BET) surface area analysis. The X-ray diffraction planes obtained for the materials synthesized when using water, ethylene glycol and a mixture of water and ethylene glycol solvents were in alignments with the reported Ni_3S_2 diffraction planes, while a mixture of nickel sulfide phases were obtained when ethanol and the mixture of water and ethanol solvents were used. TEM micrographs revealed that the structures synthesized in water, ethylene glycol and a mixture of water and ethylene glycol produced flowerlike nanostructures. The nanoflowers produced in only water consisted of smaller nanosheets. These nanoflowers also had the highest BET surface area. The materials synthesized in water were also exposed to annealing in a hydrogen gas atmosphere at temperatures between 300 and 500℃. Annealing at 300℃ caused an increase in the crystallinity of the material and a further increase in the annealing temperatures resulted in a decrease in the crystallinity of the material, which was also accompanied by a phase transformation of the materials from

Ni_3S_2 to a mixture of NiS, Ni_3S_2 and Ni_7S_6. This phase transition was also accompanied by a morphological transition from flowerlike structures to a mixture of rod-like flowers or quasi-spherical nanoparticles.

Graphene oxide (GO) was synthesized using the Improved Hummers' method and further reduced with or without the use of a reducing agent by employing a facile microwave technique in order to form reduced graphene oxide (rGO). XRD results showed an increase of the interlayer spacing upon oxidation of graphite due to the incorporated oxygen groups between the layers. After reduction this interlayer spacing decreased. Raman results demonstrated that rGO synthesized without any reducing agent had a comparable defect density with the rGO synthesized in hydrazine hydrate. However, TEM showed that the sheets in the control sample were smaller in diameter and were more agglomerated. XPS analysis showed an increased C/O ratio from 2:1 in GO to 7.8:1 in hydrazine reduced GO.

Thereafter, Ni_3S_2-rGO composites were prepared in situ and ex situ and characterized. XRD and XPS analysis confirmed the formation of the composites. TEM showed that the ex situ prepared composites were made up of 2D-2D junctions whereas the sample prepared in situ consisted of quasi-spherical nickel sulfide nanoparticles (1D) on 2D rGO sheets.

Finally, different sensors were prepared by dispersing the sensing material (Ni_3S_2, rGO, (5%) Ni_3S_2-rGO, (10%) Ni_3S_2-rGO and in situ NS-rGO) in a N,N-dimethylformadide/ethylene glycol solution and drop casted on gold electrodes. Gas sensing results showed that ex-situ prepared (5%) Ni_3S_2-rGO could potentially be used as a room temperature ethanol sensor. This sensor demonstrated a good response, the highest sensitivity and most linear sensing performance when compared with the other fabricated sensors.

TABLE OF CONTENTS

LIST OF FIGURES

CHAPTER 1

CHAPTER 2

CHAPTER 3

CHAPTER 4

CHAPTER 5

SUPPLEMENTARY INFORMATION

LIST OF TABLES

CHAPTER 1

CHAPTER 2

CHAPTER 3

CHAPTER 5

LIST OF SCHEMATICS

CHAPTER 2

CHAPTER 3

CHAPTER 5

ABBREVIATIONS

0D	Zero dimensional
1D	One dimensional
2D	Two dimensional
3D	Three dimensional
ALD	Atomic layer deposition
BET	Brunauer-Emmet-Teller
BHJ	Barett-Joyner-Halenda
CNTs	Carbon nanotubes
CSs	Chemical sensors
CVD	Chemical vapour deposition
DFT	Density Functional Theory
DMF	N,N-dimethylformamide
EG	Ethylene glycol
EtOH	Ethanol
FTIR	Fourier transform infrared
FWHM	Full width at half maximum
GO	Graphene oxide
HCSs	Hollow carbon spheres
HER	Hydrogen evolution reaction
HM-TEM	High magnification transmission electron microscopy
HOMO	Highest occupied molecular orbital
LEDs	Light emitting diodes
LUMO	Lowest unoccupied molecular orbital

MeOH	Methanol
MOS	Metal oxide semiconductor
MW	Microwave
MWCNTs	Multi-walled carbon nanotubes
NMs	Nanomaterials
OER	Oxygen evolution reaction
PLD	Pulse layer deposition
PXRD	Powdered X-ray diffraction
rGO	Reduced graphene oxide
RH	Relative humidity
$R_{baseline}$	Baseline resistance
R_{VOC}	Resistance in presence of volatile organic compound
sccm	standard cubic centimetres per minute
SEM	Scanning electron microscopy
SILAR	Successive ionic layer adsorption and reaction
TEM	Transmission electron microscopy
TMC	Transition metal chalcogenide
TMDs	Transition metal dichalcogenides
TU	Thiourea
VOCs	Volatile organic compounds
vs	versus
wt %	Weight percentage
WHO	World Health Organization
XPS	X-ray photoelectron spectroscopy

Chapter 1: Introduction to study and literature review

1.1. Introduction

This chapter gives the background and motivation for the study and a literature review of nanomaterials in gas sensing with a specific focus on the materials to be used in this study and the different synthesis methods. The aim and the objectives of this study as well as an outline of this dissertation is also presented.

1.2. Background and motivation

Energy is a vital pillar in the modern world - we need it for economic development, to light up our houses, to generate heat and to power machinery needed in our homes, offices and factories. However, the energy used is dominantly produced from fossil fuels. These fuels release carbon dioxide and other greenhouse gases into the atmosphere [1]. Currently, one of the world's biggest problems associated with energy generation is air pollution. Air pollution is caused by an increase of toxic substances in the atmosphere from mining activities; emissions from motor vehicles; power plants; and chemical industries [1-3]. In South Africa, Mpumalanga was listed as a global hotspot for pollution in October 2018 [4]. Satellite data from Greenpeace Africa revealed that most of the world's NO_2 emissions are from this area. Less than a year later, the same area was reported by Greenpeace India as the second highest hotspot for SO_2 emissions [5]. These dangerous substances and others including CO, CH_4, H_2S, NH_3 and VOCs such as ethanol, methanol, formaldehyde, toluene and xylene are hazardous to human health leading to a range of diseases from respiratory infections, cardiovascular diseases, cancer, psychological disorders, morbidity and even mortality [1, 6]. According to data reported by the World Health Organization (WHO) in 2018, 9 out of 10 people in the world breathe polluted air. Annually, 7 million people die from exposure to polluted air globally. In 2016, 4.2 million deaths were attributed to outdoor air pollution and 3.8 million to indoor air pollution [7]. The dirty air also negatively affects ecosystems and agriculture, decreasing the production and quality of food which could possibly lead to a food crisis in the near future [8]. Furthermore, the expenses related to healthcare costs due to pollution are gradually increasing and are estimated to be 0.4 % of the global GDP by 2060 [9]. These negatives often also cause the eruption of conflicts between countries, politicians, environmental stakeholders and agencies such as WHO, United Nations Environment, and Greenpeace.

Researchers together with governments and stakeholders are rigorously searching for ways in which toxic and life-threatening substances in the environment can be detected and monitored. This is not only for environmental protection, but also for energy saving as most available detection measures consume a lot of electricity. The use of nanotechnology has enabled the application of nanostructured gas sensors have been employed in various sectors for monitoring toxic substances [2-3]. A sensor consists of a system that measures the change in a property or a change in the analyte. The sensor element picks up a physical or chemical change from the surrounding environment and induces a signal. The transducer interprets the signal as a particular parameter and converts it into understandable output data [10]. Therefore, gas sensors are devices that are able to change their properties based on their interaction with gaseous species in the environment [11].

Metal oxide semiconductors (MOSs) have been at the forefront of research in sensor applications due to their ease of fabrication, low cost, environmentally friendly nature and relatively good chemical stability [11-12]. Even though they are the most studied materials for sensing, they suffer from drawbacks that make their practical applicability difficult. MOSs operate optimally at high temperatures, usually 100℃ -500℃ [3, 12]. This creates an energy demand as more electrical power is required to reach the optimum working temperatures. The high power demand also makes it difficult to produce miniaturized portable devices. Another challenge with MOSs is their poor ability to recover back to their initial state [3]. These materials are also limited by their low sensitivity and low selectivity, which is the inability to detect a very small volume of the analyte in a specific time and the inability to detect one specie in a mixture of other species, respectively [3, 13].

In an attempt to improve some of the limitations present in MOSs, different physical and chemical modifications have been explored. Tailoring the architecture of a MOS and adding dopants or impurities has the capability of improving the sensitivity as well as selectivity of MOS based sensors [13]. Novel nanomaterials with the potential of performing better than MOSs are also being investigated. Nevertheless, even new materials have limitations and the demand for new gas sensing technologies requires materials to evolve continuously. One idea that has proven to have gained interest recently is the construction of heterostructured nanomaterials [10]. The synergistic effects due to hybridization of the different structures in heterostructured materials have the ability of offering improvements in sensing performance. Ni_3S_2-rGO has been extensively studied for its use in electrochemical applications, such as

water splitting and supercapacitors but its use in chemical gas sensors remains unexplored. Therefore in this study, the use of a heterostructured nanomaterial consisting of a transition metal chalcogenide, Ni_3S_2, and a graphene derivative, reduced graphene oxide (rGO), is explored for its possible application in room temperature gas sensing.

1.3. Nanomaterials

The phenomenal properties that emerge when materials are in nanometre scale have propelled the advancement of nanomaterials in a myriad of applications ranging from energy storage devices used in our smart gadgets to breathalysers used by traffic officers to check if the amount of alcohol in a driver's system exceeds the legal limit or by medical officials to detect certain substances for medical diagnosis. Nanomaterials are known to have exceptional mechanical, optical, electrical, catalytic and magnetic properties, which make them superior when compared with their bulk counterparts [14-15].

Nanomaterials are commonly defined as materials with at least one of their linear dimension being less than 100 nm in size [15-16]. These materials can be classified into four groups according to dimensionality [16]. Zero-dimensional (0D) materials are nanoparticles, quantum dots and carbon dots in which the movement of electrons is confined in all three dimensions [16-19]. Nanowires, nanobelts and nanorods are one-dimensional (1D) because their electrons can only move freely in the X-direction [20]. Thin films like graphene, hexagonal boron nitride and Mxene allow the flow of free electrons in the X and Y planes and are thus two-dimensional (2D) [21]. Finally, three-dimensional (3D) materials such as nanocubes, metal-organic-frameworks and aerogels allow flow of electrons in the X, Y and Z direction [22]. Different desirable properties can be found in the different groups of nanomaterials. For instance, the attractive properties of 0D nanomaterial (i.e. strong quantum confinement that lead to enhanced photoluminescence properties) has inspired the interest for application in light emitting diodes (LEDs), solar cells and lasers [15, 17-19]. 1D nanostructures have shown great potential for electronic applications because of their direct electronic pathways [20] whereas 2D material are well known for their large specific surface areas and abundantly available active sites, which is suitable for sensing and catalysis [21]. The continuous porous network in 3D aerogels structures enhances molecule transport that is beneficial for electrodes in energy storage devices [22].

1.4. Nanostructured gas sensors

Gas sensors are devices that detect the presence and concentration of various hazardous gases and vapours [23]. These devices were historically only used in coal mines [24]. Currently, they are applied in the automotive industry [13], healthcare sector [25], food industry [26], environmental monitoring [27], and indoor safety [28]. Nanomaterial application in gas sensing provide advantageous properties, for instance high surface-to-volume ratios, high adsorptive capacity and high reactive capacity [29]. Their large surface areas enhances catalytic and sensing response by allowing rapid movement of analyte molecules in the material [21, 29]. Additionally, the physical, catalytic and electrical properties of nanomaterials can be easily tuned by reducing spatial dimensions and or confinement of structures in a specific crystallographic direction [15, 29].

Researchers initially classified sensors according to the property measured by the sensor [30]. The measurands were mechanical, thermal, optical, electric, acoustic, chemical, radiation, biological and magnetic properties. In 2012, Liu et al. [31] classified gas sensors in two groups according to their sensing methods, i.e. (i) methods based on electrical variation and (ii) methods based on variation in other properties. Metal oxide semiconductors, polymers, carbon nanotubes and moisture absorbing materials sense gases based on the variation in electrical properties. Optic methods, acoustic methods, gas chromatography and calorimetric methods fall under the second category. Other researchers have also classified gas sensors using various other classifications [32-33]. For the purposes of this study, the focus will only be on chemiresistive gas sensors.

In a chemiresistive gas sensor, a change in electrical resistance is observed due to a change in the chemical environment. Metal oxides semiconductors are the most investigated group of chemiresistive gas sensors proven by the vast amount of literature available [13, 31-33]. A chemiresistive sensor usually consists of a substrate and sensing film that is coated on the interdigitated electrodes (**Fig. 1.1**) [34]. The sensing material has an inherent resistance that can be modulated by the presence or absence of a gas analyte. When exposed to a particular gas, the sensing film interacts with the gas molecules causing changes in the resistance. The resistance changes can indicate a presence of a particular gas and/ or the concentration of the gas.

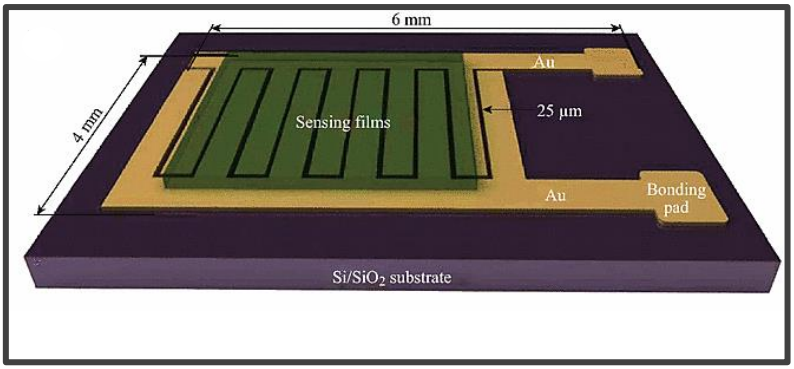

Figure 1. 1. View of a typical chemiresistive gas sensor with sensing film coated on the interdigitated electrodes [34].

1.4.1. Performance parameters of gas sensors

Different parameters are taken into consideration when designing gas sensors [10, 13, 31-33, 35]. These parameters serve as indicators that help determine the performance of the sensor. The sensitivity of a gas sensor is defined as the lowest amount of gas that can be detected by the device. It is given by the ratio R_a/ R_g for reducing gases and R_g/ R_a for oxidizing gases where R_a is the resistance of the gas sensor in the reference gas, which is usually air, and R_g the target gas. Sensitivity is expressed as a percentage that can be calculated using the following equation:

$$\% \text{ Sensitivity} = {(R_a - R_g)}/{R_a} \times 100\ \% \qquad (\mathbf{1.1})$$

Selectivity is the ability to detect a specific gas in the presence of a mixture of other gases. Whether a sensor returns to its original state when the gas concentration returns to normal is known as the sensor's reversibility. The response time can be defined as the time span to reach 90% of the sensor's initial response upon exposure to the gas prior to saturation and the recovery time as the time needed to recover 90% of its initial response. Stability is the capability of the sensor to reproduce results for a certain period. The material's adsorptive capacity is also important as it influences the sensitivity and selectivity of the device. Costs related to fabrication and the energy consumption of the device are also considered. A good sensor must display high sensitivity, selectivity and stability; low response time and recovery time; and low fabrication cost and energy consumption [13, 31].

1.4.2. Principles of gas detection

Since metal oxide semiconductors have been extensively studied in gas sensing, understanding their sensing mechanism can help design and fabricate devices with outstanding performance

using novel materials. A gas sensor can display either n-type or p-type behaviour [13, 23]. This behaviour is reliant on the type of gas, whether it is a reducing or oxidizing gas, and the reactions that occur on the surface of the material upon exposure to the gas. Two processes can occur on the surface of the metal oxide, namely oxygen ion sorption and reduction-reoxidation or oxygen vacancy [2, 13, 23, 32, 35-37].

In oxygen ion sorption, when the material is exposed to air, oxygen is adsorbed on the surface vacancies to form anionic oxygen species. The state of the oxygen specie is temperature dependent. O_2^-, O^- and O^{2-} are found to be stable below 300℃ and O_2^{2-} at higher temperatures [35-37]. In an n-type semiconductor, which has negative electrons as the majority charge carriers, the adsorbed oxygen specie on the surface traps an electron from the conduction band. The trapped electron forms a depletion region between the interfaces of the MOS and the adsorbed oxygen [36] and determines the baseline resistance of the MOS. When exposed to a reducing gas (e.g. CO, NH_3, CH_4, ethanol, etc.), the gas is adsorbed on the surface of the MOS and reacts with the adsorbed oxygen specie which releases the trapped electrons (**Eq. 1.2**) back to the conduction band, increasing the electron mobility consequently reducing the sensor's resistance.

$$CO_{(g)} + O^-_{(ad)} \rightarrow CO_2 + e^- \qquad (\mathbf{1.2})$$

On the contrary, p-type semiconductors have positive holes as majority charge carriers [35]. The holes, created by the formation of the anionic oxygen specie, become occupied by electrons gained from the reducing gas upon exposure to the gas. This decrease in the hole concentration, decreases the electron mobility as a result increasing the resistance. The behaviour of both n- and p-type MOS, when exposed to a reducing gas, is illustrated in **Fig. 1.2**.

When an oxidizing gas such as NO_2 is adsorbed on the MOS surface, the opposite effect is observed. An increase in resistance occurs because of a decrease in the electron mobility for n-type semiconductor and p-type semiconductors experience a decrease in resistance due to an increase in electron mobility.

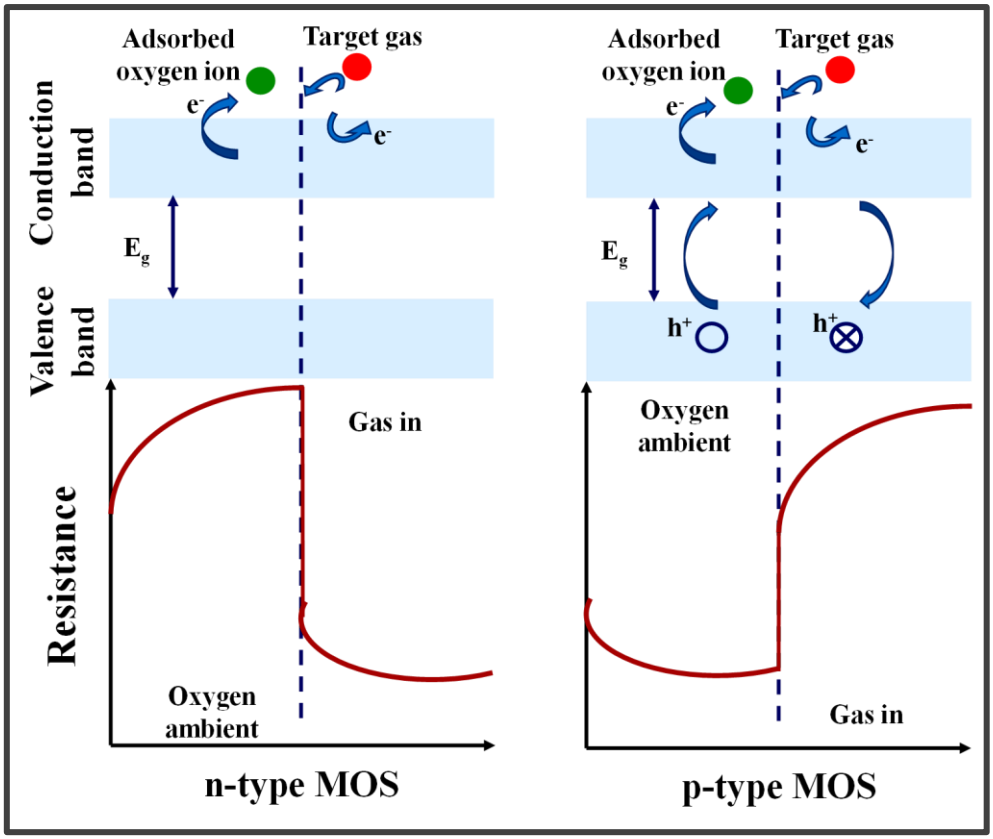

Figure 1. 2. Schematic of resistance changes in n-type and p-type semiconductors upon exposure to a reducing gas [35].

The reduction-reoxidation (oxygen vacancy) mechanism is also used in explaining conductivity in metal oxide semiconductors [35]. The reaction of a reducing gas such as CO with an oxygen on the MOS surface to produce CO_2, creates oxygen vacancies on the MOS surface. In an n-type MOS, these vacancies may be ionized inducing electrons into the conduction band increasing the conductivity of the material. The synthesis procedures of materials may also produce vacancies that may lead to reactions between the material's surface and the analyte molecules that reduce, re-oxidise or form a new molecule as the derivative of the product.

Another gas sensing mechanism that researches recently explained is resistance modulation [36]. This occurs when there are no oxygen species present. It explains the direct interaction between the gas molecules and electrons rather than the interaction of the gas and the adsorbed oxygen species on the sensor surface. The adsorption of reducing gases on the sensing material has been used to study this mechanism. The Lowest Unoccupied Molecular Orbital (LUMO) for ethanol, methanol, acetone and formaldehyde were found to be inversely related to a sensor's response [38]. The authors accounted for this behaviour by explaining how electrons

in the lower energy orbitals are captured better by the analyte gases producing an increase in resistance compared to molecules in the higher energy LUMO. In another study, the sensitivity of a sensor showed an inversely proportional relationship to the ionization energy of three aromatic compounds (benzene. toluene and xylene) [39]. The sensitivity increased from benzene (9.25 eV) to toluene (8.82 eV) and xylene (8.52 eV). In order for one to propose this mechanism for a particular sensor, one must be able to describe the different bonding models for they will assist in accurately explaining the sensing behaviour.

1.4.3. Current trends in gas sensing

Heiland was the first to ever use MOSs in sensing when he employed ZnO as sensing material in 1954 [23]. Eight years thereafter, Tagushi patented and marketed a SnO-based sensor that was able to detect low concentrations of combustible and reducing gases [40]. Today, over sixty years since their first use as gas sensitive material, metal oxide semiconductors are still dominating the field of sensing. However, since nothing is perfect, they suffer from a few limitations (high operating temperatures, poor recovery, and long response and recovery times) [2, 35]. These limitations have encouraged the investigation of new material for application in this field. Such a group of newly investigated materials is transition metal chalcogenides because of their relative low cost, easy fabrication and low surface activation energy [41]. A transition metal chalcogenide (TMC) consists of transition metal and chalcogen (sulfur, selenium or tellurium) atoms.

1.5. Metal sulfides as alternative sensing materials

Metal sulfide nanomaterials have promising potential for investigation because they are relatively inexpensive, some of them are abundant in nature and have low to non-toxicity [42-44]. These semiconductors have been used in many applications, among others, dye-sensitized solar cells [45], photo catalysis [46], water splitting [47] and sensing [48]. The use of metal sulfides as gas sensing candidates carries a few advantages. Firstly, metal sulfides have lower band gaps than MOSs [49]. This means the activation of the intrinsic surface reactions occurs at lower working temperatures hence requiring less power supply. Therefore, a reduction in the amount of energy consumed for operation of these sensing devices is expected. Additionally, a different catalytic mechanism occurs on the surface reactions of metal sulfides due to the absence of oxygen in the crystal lattice [49-51]. This absence may solve some of the constant drift issues in metal oxides, which has been ascribed to the diffusion occurring in and out of oxygen vacancies [50].

Quite a number of reports are available on the application of zinc, cadmium, tungsten, lead, molybdenum and tin sulfides as plausible candidates in the field of sensing [42, 44, 48-63]. ZnS has been used for the detection of VOCs with high selectivity and high response [52]. PbS thin films have been applied for the fast electrochemical detection of NO_2 at room temperature [53]. Chemiresistive sensors made up of WS_2 [54], MoS_2 [44, 54], and CdS [56] thin films have also been used for low temperature NH_3 and NO_2 sensing. In order to better the performance of metal sulfides, strategies such as using different morphologies, changing the method of synthesis, making porous material, doping with noble metals and forming heterostructures or composites with other materials have been implemented [60-62]. These strategies have been able to address the challenges related to sensitivity, recovery and stability.

SnS_2 is often preferred over other metal sulfides due to its non-toxicity [44, 57]. Therefore, different SnS_2 nanostructures have been synthesized including nanoparticles [42], nanorods [50], nanoflakes [57] and flowers [59, 61]. Xiong et al. [59] used flower-shaped SnS_2 nanostructures for NH_3 detection at 200℃. Their sensor displayed high selectivity and high response time. The use of 2D SnS_2 by another group reduced the operating temperature to room temperature and enhanced the response/recovery speed [55]. In an attempt to improve the hydrogen sensing performance of MoS_2, Suh and colleagues decorated the surface of MoS_2 with Pd and Au nanoparticles [60]. The decoration of MoS_2 with Pd nanoparticles was able to enhance the selectivity of hydrogen by forming Pd-hydride. The Au nanoparticles improved the overall sensing performance to all the tested gases. They also noticed that the sensor displayed either n- or p-type behaviour depending on the gas species and operating temperatures.

Leonardi et al. [49] synthesized SnS_2-SnO_{2-x} for the detection of 50 ppm NH_3 at 130℃. This heterostructured sensor had a response and recovery time of 60 s and 300 s, respectively. They attributed this to the physisorption of the NH_3 gas on the surface of the SnS_2, the reaction of the gas molecules with the chemisorbed oxygen species on the SnO_2 surface, as well the new properties that the heterostructure presented. WS_2-ZnS heterostructures were applied for the room temperature detection of NO_2 [63]. These heterostructures showed great selectivity towards NO_2 in the presence of NH_3 and some VOCs, improved the sensitivity, higher recovery/response speed, good recoverability and stability unlike pure WS_2. The formation of p-n heterojunctions, the increased number of active sites available for adsorption and the accelerated charge transfer all accounted for the improved performance.

1.6. Nickel sulfide

1.6.1. Nickel sulfide nanostructures

Among the metal sulfide family, nickel sulfide structures have attracted much interest because of their good catalytic performance, ease of fabrication coupled with their low cost and low toxicity [43, 64-65]. Nickel sulfide consists of a complex family with different nickel and sulfur ratios [43, 65-67]. A large number of nickel and sulfur rich phases occur at low temperatures such as NiS, Ni_3S_2, Ni_3S_4, Ni_7S_6 and Ni_9S_8 [66]. The properties of nickel sulfide has promoted its application in water splitting [64, 66], solar energy [67], Li-ion batteries [68] and other energy storage devices [69]. In terms of sensing, nickel sulfides have been mostly investigated for electrochemical sensing, with very few reports available on their chemiresistive sensing application [70-73].

NiS films were prepared by electrodeposition for the electrochemical sensing of glucose [71]. The sensor had a low response time of 8 s and a low detection limit of 0.32 μM. The good catalytic activity of NiS towards effective electro-oxidation of glucose attributed to the excellent performance. In another study, a three-dimensional flower-like Ni_7S_6 electrochemical sensor was used for the detection of hydrogen peroxide and enzyme-free glucose [72]. The sensor had a low detection limit of 0.15 μM for both analytes with good selectivity in the presence other biomarkers.

A chemiresistive sensor based on pure NiS for H_2 detection at 300℃ showed poor recovery [73]. Once decorated with Au nanoparticles, the sensor was able to recover completely. The Au nanoparticles helped facilitate the adsorption and desorption of the H_2 gas. Recently, a fibres-shaped NiS ethanol sensor showed improved response, selectivity and stability once In_2O_3 fibres were incorporated into the NiS structure [74]. The authors attributed the enhanced performance to the large surface area and the p-n heterojunction.

1.6.2. Ni_3S_2

Heazlewoodite, Ni_3S_2, is known as the most stable of all the nickel sulfide phases [66, 75]. It is a good metallic conductor with a resistivity of 1.8×10^{-5} Ω at room temperature [43, 65-66, 70], good magnetic properties, and a high theoretical capacity that makes heazlewoodite a promising electrode candidate in photo catalysis [76], dye-sensitized solar cells [77], supercapacitors [78], Li-ion and Na-ion batteries [64, 68], and hydrogen evolution and oxygen evolution reactions (HER and OER) [65-66, 75]. Ni_3S_2 crystallizes in a rhombohedral structure

with each of the Ni atoms sitting at a pseudo tetrahedral site in an approximately body centred cubic sulfur lattice (**Fig. 1.3**) [65, 75]. The Ni-Ni bonding of Ni_3S_2 is more covalent than in other Ni-based structures. The four Ni-Ni bonds developed for each of the Ni atoms connect all of the Ni atoms along a highly branched path. These short Ni-Ni bonds are comparable to the bonds in Ni metal contributing to its unique structure.

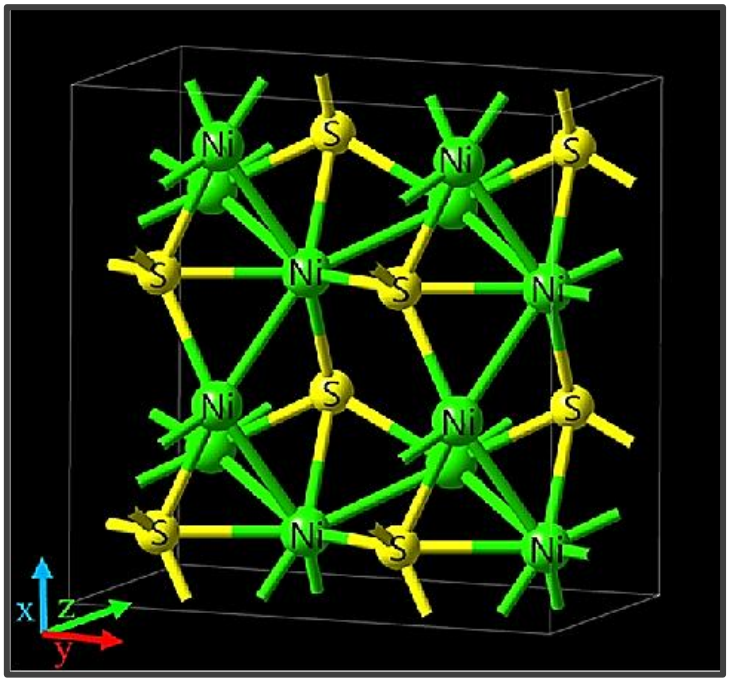

Figure 1. 3. Crystal structure of Ni_3S_2 illustrating its trigonal bypyramidal core [75].

To the best of our knowledge, there is little literature available on the use of the Ni_3S_2 catalyst in sensor applications. A cauliflower-like Ni_3S_2 on Ni foam electrochemical sensor with a large surface area and effective ion/electron transfer was able to detect glucose with high sensitivity, good selectivity, good repeatability and short response time [70]. Linganiso and co-workers fabricated a room temperature chemiresistive humidity sensor with layer-based Ni_3S_2 [79]. Their sensor showed a sensitivity of 4.5 for 70% relative humidity. This decreased to 2.5 and 1.4 once doped with selenium and tellurium, respectively. Nanocomposites comprising of Ni_3S_2 and carbon nanotube has also been reported for the electrochemical detection glucose [80] and 4-methoxyphenol [81].

1.7. Graphene-based sensors

Graphene has undoubtedly been at the forefront of many innovative nanotechnology advancements. Graphene is a monolayer of sp^2 hybridized carbon atoms arranged in a 2D

honeycomb lattice [82-83]. This extensively investigated carbon material is the basic structure of all other carbon-based materials (**Fig. 1.4**) [84-85]. It rolls up in a tubular way to form carbon nanotubes, forms fullerenes by wrapping and graphite by stacking. The fascination of graphene in the development of gas sensors is attributed to its low electrical noise, excellent carrier mobility of about 200 000 $cm^2V^{-1}s^{-1}$ at an electron density of ~2×10^{11} cm^{-2}, great electrical conductivity of 1.0×10^8 S/m, high thermal conductivity of 2 000- 4 000 $Wm^{-1}K^{-1}$, and a large theoretical surface area of 2 600 m^2g^{-1}[82, 86].

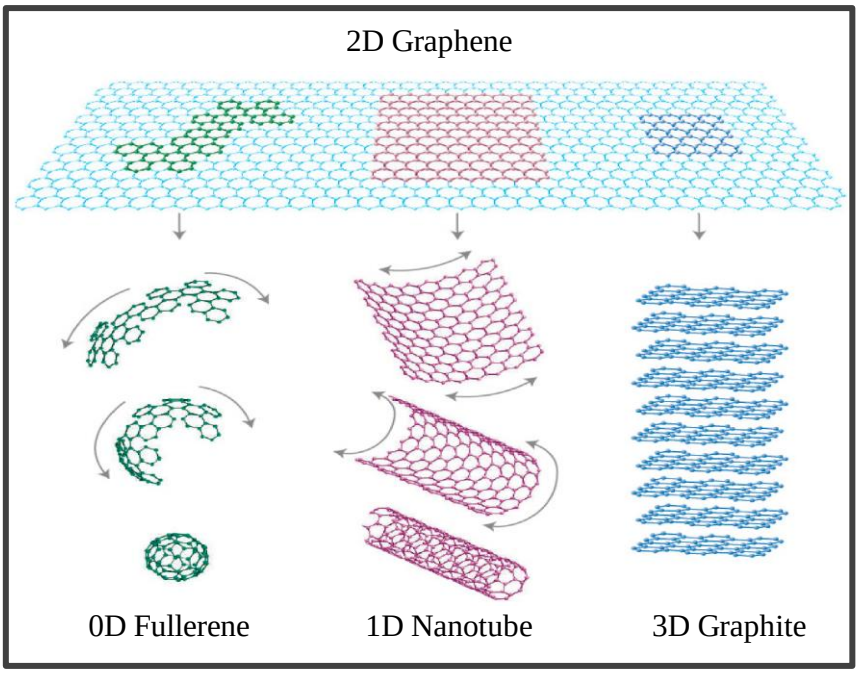

Figure 1. 4. Schematic illustration of carbon allotropes [84].

A publication on the detection of adsorbed gas molecules on the surface of graphene sheets by Schedin and colleagues sparked the great interest of graphene sensors [83]. Carbon dioxide detection using a graphene-based conductometric sensor was developed by mechanical cleavage and micromachining [87]. The sensor portrayed a rapid and reproducible response because of the weak interaction between the CO_2 and graphene. Despite the good sensing performance of graphene, using pure graphene in gas sensing for real time applications is impractical because (i) pristine graphene has no functional groups on its surface required for gas and vapour adsorption, (ii) it is not producible in large scale and (iii) it has no band gap [83-85]. Researchers have explored graphene derivatives in the hope of achieving better sensing performance [86, 88-89]. One such derivative is reduced graphene oxide (rGO), which was first applied by Robinson for sensing and has since been widely studied for sensing applications [89].

1.7.1. Reduced graphene oxide sensors

Reduced graphene oxide (rGO) is defined as graphene sheets with oxygen functionalities attached on the sheet surface. It is obtained by reduction of highly oxygenated graphene oxide (GO). rGO is usually preferred in graphene-based sensors because of the abundant defects and chemical groups that facilitate gas adsorption; the easily tuneable chemical and electrical properties; and its efficient charge transport [86]. Robinson et al. [89] pioneered the application of rGO in sensing when he reported a detection of 10 s exposure of ppb levels of chemical-warfare agents and explosives. They were able to tailor the response and recovery characteristics of the sensor by adjusting the reduction process. Perforated reduced graphene oxide nanosheets have been employed for the room temperature detection of NO_2 in the parts-per-billion range [90]. The authors ascribed the high sensing performance to the sufficient functional groups and the diffusion channels available in the nanoporous rGO. A sensitive sensor fabricated using rGO was also reported of having good sensitivity, moderate stability and high selectivity for NH_3 in the presence of various VOCs [91].

However, rGO also has its limitations. It suffers from poor selectivity to various gases and it tends to agglomerate irreversibly in aqueous solutions due to strong $\pi - \pi$ stacking and van der Waals interactions between the sheets. The latter weakens the response sensitivity and recovery [86]. To improve sensor performance features of rGO, physical and chemical modification of rGO have been explored. Functionalization of rGO with traditional gas sensing materials by either doping with noble metals or forming hybrids and heterostructures with metal oxides, polymers and organic ligands has been considered for enhanced sensing performance [86, 88]. The heterostructure are found to have accelerated charge transfer, improved performance and can to a certain extent avoid aggregation of the rGO sheets. For example, the synergistic interaction between SnO_2 and rGO was able to produce a highly selective NO_2 sensor [92]. Introducing rGO to In_2O_3 afforded a NO_2 sensor a response that was seven times higher than pristine In_2O_3 [93]. The excellent sensing performance was due to the high surface area and the local p-n junctions and the introduction of rGO was also able to decrease the operating temperature to as low as room temperature.

1.7.2. Reduced graphene oxide- metal sulfide sensors

Reports available on rGO-metal sulfide composites as sensing material have increased over the last few years with a majority of them focusing on NO_2 sensing [12, 51, 94-97]. Zhou et al. [51] made an rGO/MoS_2 film for NO_2 detection. The larger exposure area, more adsorption

sites and the p-n heterojunction were all responsible for the good response features. They studied the effect of the concentration of both the rGO and MoS_2 in the hybrid. The sensing response increased with a decrease in the amount of rGO from 1 to 0.1 mg/mL and then decreased when the concentration was 0.05 mg/mL and lower. They also noticed that the response of the sensor prepared by mixing GO and MoS_2 followed by reduction was better than the one prepared by mixing rGO and MoS_2. This is because fewer p-n junctions exist in the ex-situ prepared composite due to the weaker contact between the two materials caused by the less number of functional groups in rGO. Mixing of GO and MoS_2 before reduction also helped in reducing the aggregation of MoS_2. Cheng and colleagues [96] found that the heterojunction between the interface of rGO and SnS_2 resulted in an electronic sensitive effect that enhanced the response for NO_2 sensing. rGO was able to alleviate restacking and agglomeration of SnS_2, but as rGO became the more dominant effect in the composite, it agglomerated and decreased the response and recovery of the sensor. Other examples of rGO-metal sulfide sensors are summarized in **Table 1.1**.

Table 1. 1. Studies on rGO-metal sulfide materials for gas sensing.

Materials	**Analyte**	**Operating Temp (℃)**	**Lowest limit of detection**	**Response/Recovery time (s)**	**Ref**
rGO/MoS_2 film	NO_2	60	5.7 ppb	-	[51]
3D MoS_2/rGO composite	NO_2	80	27.9 ppb	-	[94]
rGO/MoS_2	Humidity	25	50 %	59/343	[95]
rGO hybridized with WS_2 nanoflakes	NH_3	33.5	10 ppm	60/300	[12]

Quasi- 2D rGO/SnS_2 hybrid	NO_2	150	500 ppb	50/48	[96]
rGO decorated with CdS/CdO	NO_2	125	2 ppm	76/82	[97]
rGO-MoS_2-CdS	NO_2	75	200 ppb	25/34	[98]

1.8. Ni_3S_2-rGO composites

The combination of Ni_3S_2 with rGO has offered favourable features, especially in energy storage devices [99-105]. A high performance supercapacitor fabricated using Ni_3S_2 nanocubes wrapped with rGO exhibited ultra-high specific capacity and current density because of the synergistic effect of graphene as a conductive support and Ni_3S_2 cubes as pseudo capacitive material [99]. rGO acted as a 2D support for the homogeneous growth of the Ni_3S_2 cubical structures and it also increased the double-layer capacity by providing a large surface area. Furthermore, the Ni_3S_2 structures assisted in the effective enhancement of the accessible surface area by preventing the restacking of the rGO sheets. Anode material for sodium ion batteries consisting of rGO coated on a clustered nanosheets array of Ni_3S_2 grown on Ni foam was proven to have high specific as well as excellent cycling stability [100]. The authors ascribed the improved performance of the Ni_3S_2/Ni to rGO, which promoted the displacement reaction of Ni_3S_2 with sodium. The performance of this electrode was also theoretically studied using density functional theory (DFT) studies. The calculations revealed that rGO was able to significantly improve the electron mobility and the hybrid interaction between the extraneous p orbits of C and the indigenous p and d of Ni, and the p orbits of S. The latter was concluded as the major reason for the enhanced electrical transport properties by rGO.

However, to the best of our knowledge there is no literature available on the use of Ni_3S_2-rGO composites for application in sensing. The united physicochemical properties of Ni_3S_2 and rGO

in the field of sensing could potentially, just as in electrochemical devices, provide desirable advantages.

1.9. Synthesis techniques for nanomaterials

1.9.1. Different synthesis techniques

As aforementioned, the functional properties of nanomaterials are related to their morphology hence much attention has been given to the synthesis of these materials. Nanomaterials are synthesized by employing different methods, such as physical, chemical, electrochemical and photochemical techniques [29]. There are a few factors to be considered when choosing a synthesis technique: (i) nucleation and growth processes; (ii) stability of the synthesized material; (iii) interfaces and distributions of the material; (iv) how to best control the size and composition of the as-synthesized materials; and (v) the scale-up and assembly strategies employable for low cost large-scale production.

Chemical methods play a major role in the synthesis of nanostructured materials. Wet chemical methods are, amongst others, hydrothermal or solvothermal techniques, sol-gel procedures, co-precipitation, etc. [23, 106]. These methods provide the advantage of obtaining pure nanomaterials however, their long reaction times are disadvantageous. In the slow heating process that occurs during hydrothermal synthesis, the solution reaches low super-saturation after a long time creating initial nuclei with a wide size distribution [23, 107]. The materials synthesized using these methods sometimes need post-synthesis high temperature annealing to obtain the desired structures [23]. These limitations have driven the development of novel synthesis techniques that are more efficient and effective in terms of energy, time and costs. Microwave synthesis is considered a clean and eco-friendly technique forming part of the branch of green chemistry [107-109].

1.9.2. Microwave synthesis

1.9.2.1. Microwave principles

Microwaves lie between radio and infrared waves in the electromagnetic spectrum. By definition, they are waves that lie between the wavelengths of 1 mm and 1 m that correspond to the 0.3 – 300 GHz frequency range. These waves were initially only used in telecommunications [23, 107-108]. In 1946, Percy Spencer at Raytheon Corp discovered microwave heating. This lead to the implementation of microwave heating in processes such as cooking food, thawing, curing wood, treatment of materials such as sewage sludge and

processing of medical waste [23, 110]. All microwaves (commercial and industrial) are only allowed to operate at a frequency of 2.45 GHz, by international agreement, so as to avoid interference with telecommunication, cell phone and other wireless networks [23].

In microwave heating, electromagnetic energy is transferred into thermal energy. Therefore, it is a conversion of energy rather than a heat transfer phenomenon. The energy is delivered via radiation and not convection or conduction [23, 107, 109]. The electric component of the electromagnetic field causes heating by means of two different mechanisms, i.e. dipolar polarization mechanism and conduction mechanism [23, 109, 111]. In dipolar polarization, permanent and induced dipoles rotate in attempt to align with the alternating field. The rotating molecules generate friction among themselves and the energy is dissipated in the form of heat. This occurs when water and other polar solvents partake in the reaction. In the conduction mechanism, charged particles (electrons, ions, etc.) present in the reaction obtain their kinetic energy from the microwave's electric field and collide with atoms in neighbouring molecules to generate heat. The latter is much stronger with regards to heat generating capacity [111].

Materials can be classified in different categories based on their absorption ability of microwaves [110-112]. Materials that are not efficiently heated by microwaves, in which the microwaves are reflected or have negligible energy absorption, are called microwave reflectors or opaque materials. All bulk metals fall under this category. Low-loss insulator materials such as Teflon or quartz are transparent to microwaves. Microwaves are able to penetrate these materials without being absorbed, heat being lost or generated. These materials are called microwave transmitters or transparent materials. Microwave absorbers or high-loss insulators absorb microwave energy and are heated up rapidly. These dielectric materials are an important class for microwave synthesis. There is also another important group, namely mixed absorbers [110]. These are the more advanced materials present as composites or multiphase where at least one of the phases consist of high loss insulators and some as low loss insulators. Examples are metal matrix composites, ceramic matrix composites and polymer matrix composites.

1.9.2.2. Advantages of microwave synthesis routes over conventional synthesis techniques

Heating in a conventional oil bath (or heating mantle) takes place with an external heating source. Firstly, it heats the reaction vessels. Thereafter, that heat is transferred from the vessel to the reaction mixture (**Fig. 1.5**a). This depends on convection currents and thermal conductivity of the materials that must be penetrated [23, 107]. The temperature of the reaction vessel is usually higher than that of the reaction mixture inside. In addition, heating of the

reaction mixture is often not uniform. This temperature gradient can lead to synthesized products with non-uniform properties. This process is also sluggish and inefficient.

In microwave heating, microwave radiation is delivered directly to the molecules present in the reaction mixture and the temperature of the bulk is raised simultaneously (**Fig. 1.5**b) [23]. Selective heating takes place where the energy is delivered directly to the target material without any interaction with the surrounding environment. Volumetric heating is another advantage where heat is generated throughout the entire volume of the material and the temperatures reached in the microwave vessel can be increased well above the boiling point of a solvent thus increasing the rate of the reaction by a factor of 10-1000. Moreover, reactions reach completion faster meaning higher yields are obtained with very few by-products. The products also have smaller particle sizes and a narrower size distribution due to the short reaction time. This technique also has the possibility of producing materials that cannot be obtained using conventional methods. Microwave synthesis not only offers efficiency with regards to time, but it is also saves energy, is safe, can be automated and is cost effective.

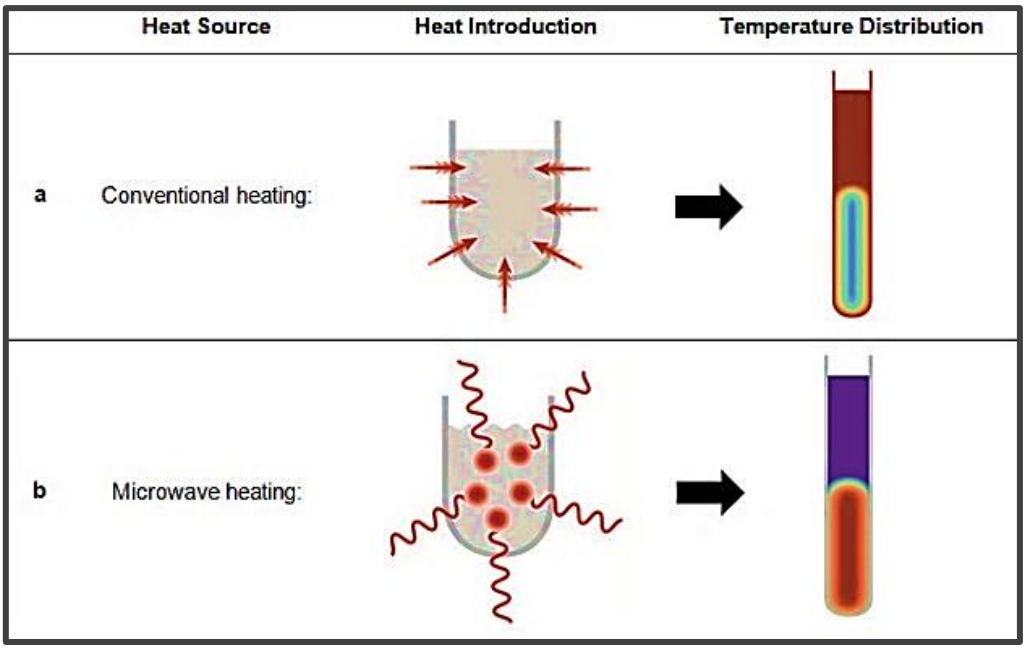

Figure 1. 5. Conventional heating (a) and microwave heating (b) [113].

1.9.2.3. Materials synthesized via microwave methods for sensing applications

Various sensor material synthesized by microwave technology are found in literature [73, 111, 114-120]. Microwave synthesized metal oxides, metal sulfides and composites have all been investigated and have shown good performance. Cho and co-workers [114] reported an improvement in the gas sensing performance of SnO_2 when synthesized with a microwave-

assisted method instead of a conventional method. They attributed the shortening of the response time to the formation of mesopores in the SnO_2 due to rapid gas evolution that occurred during synthesis. The influence of microwave parameters on sensing have been evaluated using ZnO structures [117]. The power and reaction time had no influence on the morphology of the structure but the power had an influence on the sensor response. Structures synthesized at low power had a higher response than those synthesized using a higher heating power. This can be due to the different amount of active sites created by tuning the heating power. Heterostructured materials for sensing have also been synthesized by microwave techniques [111, 118-120]. Microwave hydrothermally produced MoO_3 nanorods on rGO sheets showed high gas-sensing performance to H_2S [120]. The improved gas sensing response of the hybrid material was attributed to the large surface area that facilitated rapid carrier transport and the electron migration at the interface of the MoO_3 and the rGO.

1.10. Aim and objectives

The main aim of this study was to synthesize Ni_3S_2-reduced graphene oxide composites for the application in room temperature chemoresistive gas sensing devices.

In order to achieve the main aim, the following objectives were implemented:

1. To synthesize Ni_3S_2 nanostructures employing a microwave hydrothermal method and to study the effect of different solvents on the chemical and physical properties of the nanostructures.
2. To synthesize graphene oxide using the Improved Hummers' method.
3. To reduce graphene oxide using different reduction techniques.
4. To make Ni_3S_2-reduced graphene oxide composites of different Ni_3S_2 to reduced graphene oxide ratios.
5. To characterise the as-synthesized materials using various techniques, such as: X-ray diffraction (XRD), Raman spectroscopy, Fourier transform infrared (FTIR) spectroscopy, X-ray photoelectron spectroscopy (XPS), transmission electron microscopy (TEM) and Branauer- Emmett- Teller (BET) surface area analysis.
6. To fabricate sensing devices using the as-synthesized materials and to evaluate their room temperature gas sensing properties.

1.11. Dissertation outline

Chapter 1: Introduction to study and literature review

Herein, the background and motivation for the study are briefly discussed. This chapter also gives insight into materials used in gas sensing technologies, graphene and its related materials as gas sensors and metals sulfides as possible gas sensing materials. Additionally, it highlights the use of heterostructured materials as possible solutions to the problems faced with the current gas sensing materials. Finally, the main aim and objectives of the study are also stated.

Chapter 2: Microwave synthesis of Ni_3S_2 nanostructures

This chapter looks into the microwave synthesis and characterization of Ni_3S_2 nanostructures. Water, ethanol and ethylene glycol were applied as solvents during synthesis. The effect of hydrogen gas annealing on the synthesized structures was also studied.

Chapter 3: Synthesis of reduced graphene oxide from graphite powder

In this chapter reduced graphene oxide was synthesized from graphite powder and characterized. Graphene oxide was firstly produced from graphite and characterized. Microwave and a conventional thermal reduction strategies were employed to synthesize reduced graphene oxide.

Chapter 4: Synthesis of Ni_3S_2-reduced graphene oxide composites

This chapter shows the in situ and ex-situ synthesis and characterization of the composites.

Chapter 5: Application of nickel sulfide-reduced graphene oxide composites in sensing devices

The fabrication of the sensing devices, testing of the devices as well as the results obtained are discussed in this chapter.

Chapter 6: Conclusions and recommendations

The general concluding remarks on the work covered in the study and future recommendations are made in this chapter.

References

[1] Perera, F., International Journal of Environmental Research and Public Health **15** (2018) 16.

[2] Chatterjee S.G., Chatterjee, S., Ray. A.K., Chakraborty, A.K., Sensors and Actuators B **221** (2015) 1170- 1181.

[3] Mirzaei, A., Neri, G., Sensors and Actuators B **237** (2016) 749- 775.

[4] Greenpeace

https://www.greenpeace.org/africa/en/press/4202/new-satellite-data-reveals-the-worlds-largest-air-pollution-hotspot-is-mpumalanga-south-africa/ Accessed 06 June 2019.

[5] Greenpeace

https://www.greenpeace.org/africa/en/press/7678/mpumalanga-so2-pollution-as-bas-as-no2-new-study-finds Accessed 20 August 2019.

[6] Altieri, K.E., Keen, S.L., Science of the Total Environment **684** (2019) 610-620.

[7] World Health Organization

https://www.who.int/news-room/detail/02-05-2018-9-out-of-10-people-worldwide-breathe-polluted-air-but-more-countries-are-taking-action Accessed 20 August 2019.

[8] The African Centre for the Constructive Resolution of Disputes

https://www.accord.org.za/ajcr-issues/conflict-implications-of-coal-mining-and-environmental-pollution-in-south-africa/ Accessed 06 June 2019

[9] Organization for Economic Cooperation and Development (OECD), 2016. The Economic Consequences of Outdoor Air Pollution. OECD Publishing, Paris. https://doi.org/10.1787/9789264257474-en.

[10] Paladiya, C., Kiana, A., Sensors and Actuators B **268** (2018) 494‑511.

[11] Zappa, D., Galstyan, V., Kaur, N., Munasinghe Arachchige, H.M.M,A., Sisman, O., Comini, E., Analytica Chimica Acta **1039** (2018) 1- 23.

[12] Wang, X., Gu, D., Li, X., Lin., S., Zhao, S., Rumyansteva, M.N., Gaskov, A.M, Sensors and Actuators B **282** (2019) 290‑299.

[13] Dey, A., Materials Science & Engineering B **229** (2018) 206- 217.

[14] Jeevanadam, J., Barthoum, A., Chan, Y.S., Dufresne, A., Danquah, Beilstein Journal of Nanotechnology **9** (2018) 1050-1074.

[15] Tiwari, J.N., Tiwari, R.N., Kim, K.S., Progress in Materials Science **57** (2012) 724-803.

[16] Pokropivny, V.V., Skorokhod, V.V., Materials Science & Engineering C **27** (2007) 990-993.

[17] Otieno, F., Shumbula, N.P., Airo, M., Mbuso, M., Moloto, N., Erasmus, R.M., Quandt, A., A., Wamwangi, D, AIP Advances **7** (2017) 085302.

[18] Wu, J., Chen, S., Seeds, A., Liu, H., Journal of Physics D: Applied Physics **48** (2015) 363001.

[19] Li, Z., Wang, L., Li, Y., Feng, Y., Feng, W., Composites Science and Technology **179** (2019) 10- 40.

[20] Jin, T., Han, Q., Wang, Y., Jiao, L., Small **14** (2018) 1703086.

[21] Yang, F., Song, P., Ruan, M., Xu, W., FlatChem **18** (2019) 100133.

[22] Rolison, D.R., Long, J.W., Lytle, J.C., Fischer, A.E., Rhodes, C.P., McEvoy, T.M., Bourg, M.E., Lubers, A.M., Chemical Society Reviews **31** (2009) 226-252.

[23] Mirzaei, A., Kim, J-H., Kim, H.W., Sim, S.S., Sensors and Actuators B **258** (2018) 270-294.

[24] Sharma, S., Madou, M., Philosophical Transactions of the Royal Society A: Mathematical **370** (2012) 2448-2473.

[25] Nasiri, N., Clarke, C., Sensors **19** (2019) 462.

[26] Lv, M., Liu, Y. Geng, J., Kou, X., Xin, Z., Yang, D., Biosensors and Bioelectronics **106** (2018) 122 -128.

[27] Kaushik, A., Kumar, Arya, S.K., Nair, M., Malhotra, B.D., Bhansali, S., Chemical Reviews **115** (2015) 4571-4606.

[28] Caron, A., Redon, N, Thevenet, F., Hanoune, B., Coddeville, P., Building and Environment **107** (2016) 19-28.

[29] Maduraiveeran, G., Jin, W., Trends in Environmental Analytical Chemistry **13** (2017) 10-23.

[30] Choudhury, I.A., Hossain, A., Bhuiyan, S.H., Comprehensive Materials Processing, Elsevier Limited **13** (2014) 121- 148.

[31] Liu, X., Cheng, S., Liu, H., Hu, S., Zhang, D., Ning, H., Sensors **12** (2012) 9635-9665.

[32] Comini, E., Analytica Chimica Acta 568 (2006) 28-40.

[33] Korotcenkov, G., Materials Science and Engineering B **139** (2007) 1-23.

[34] Wang, T., Huang, D., Yang, Z., Xu, S., He, G., Li, X., Hu, N., Yin, G., He, D., Zhang, L., Nano-Micro Letters **8** (2016) 95-119.

[35] Akande, A.A., PhD Thesis, University of Pretoria, 2016.

[36] Walker, J.M., Akhbar, S.A., Morris, P.A., Sensors and Actuators B **286** (2019) 624- 640.

[37] Sun, Y-F., Liu, S-B., Meng, F-L., Liu, J-Y., Jin, Z., Kong, L-T., Liu, J-H., Sensors **12** (2012) 2610- 2631.

[38] Wen, Z., Tian-mo, L. Physica B **405** (2010) 1345-1348.

[39] Aluri, G.S., Motayed, A., Davydov, A.V., Oleshko, V.P., Bertness, K.A., Sanford, N.A., Rao, M.V., Nanotechnology **22** (2011) 295503.

[40] Tagushi, N., Japanese Patent Application (162) 45-38200.

[41] Theerthagiri, J., Karuppasamy, K., Durai, G., Rana, A.U.H.S., Arunachalam, P., Sangeetha, K., Kuppusami, P., Kim, H-S., Nanomaterials **8** (2018) 256.

[42] Rana, C., Bera, S.R. Saha, S., Journal of Materials Science: Materials in Electronics **30** (2019) 2016-2029.

[43] Wang, Y.K., Wu, G.L., Li, Z.T., Wu, M.B., Advanced Materials Research **1118** (2015) 9-13.

[44] Qin, Z., Xu, K., Yue, H., Wang, H., Zhang, J., Ouyang, C., Xie, C., Zeng, D., Sensors and Actuators B **262** (2018) 771- 779.

[45] Rao, S.S., Gopi, C.V.V.M, Kim, S.K., Son, M.K., Jeong, M.S., Savariraj, D., Prabakar, K., Kim, H.J., Electrochimica Acta **133** (2014) 174-179.

[46] Luo, M., Liu, Y., Hu, J., Li, J., Liu, J., Richards, R.M., Applied Catalysis B: Environmental **125** (2012) 180-188.

[47] Ren, H., Huang, Z.H., Yang, Z., Tang, S., Kang, F., Lv, R., Journal of Energy Chemistry **26** (2017) 1217-1222.

[48] Guidi, V., Fabbri, B., Gaiarda, A., Gherardi, S., Giberti, A., Malagù, Zonta, G., Belluti, P., Procedia Engineering **120** (2015) 138-141.

[49] Leonardi, S.G., Wlodarski, W., Li, Y., Donato, N., Bonavita, A., Neri, G., Journal of Alloys and Compounds **781** (2019) 440- 449.

[50] Giberti, A., Gaiardo, A., Fabbri, B., Gherardi, S., Guidi, V., Malagu, C., Bellutti, P., Zonta, G., Casotti, D., Cruciani, G., Sensors and Actuators B **223** (2016) 827- 833.

[51] Zhou, Y., Liu, G., Zhu, X., Guo, Y., Sensors and Actuators B **251** (2017) 280-290.

[52] Hussain, S., Liu, T., Javed, M.S., Aslam, N., Zeng, W., Sensors and Actuators B **239** (2017) 1243- 1250.

[53] Navale, S.T., Bangar, D.K., Chougule, M.A., Patile, V.B., RSC Advances **5** (2015) 6518-6527.

[54] Järvinen, T., Lorite, G.S., Peräntie, J., Toth, G., Saarakkala, S., Virtanen, V.K., Kordas, K., Nanotechnology **29** (2019) 405501.

[55] Chakraborty, S., Pal, M., Sensors and Actuators B **242** (2017) 1155-1164.

[56] Sonker, R.K., Yadav, B.C., Gupta, V., Tomar, M., Material Chemistry and Physics **239** (2020) 121975.

[57] Afsar, M.F., Rafiq, M.A., Tok, A.I.Y., RSC Advances **7** (2017) 21556-21566.

[58] Bharatula, L.D., Erande, M.B., Mulla, I.S., Rout, C.S., Late, D.J., RSC Advances **6** (2016) 105421- 105427.

[59] Xiong, Y., Xu, W., Ding, D., Lu, W., Zhu, L., Zhu, Z., Wang, Y., Xue, Q., Journal of Hazardous Materials **341** (2018) 159-167.

[60] Suh, J.M., Shim, YS., Kwon, K.C., Jeon, J-M., Lee, T.H., Shokouhimehr, M., Jang, H.W., Electronic Materials Letters **15** (2019) 368-376.

[61] Liu, D., Tang, Z., Zhang,, Z., Sensors and Actuators B **273** (2018) 473- 479.

[62] Shi, W., Huo, L., Wang, H., Zhang, H., Yang, J., Wei, P., Nanotechnology, **17** (2006) 2918.

[63] Han, Y., Liu, Y., Su, C., Wang, S., Li, H., Zeng, M., Hu, N., Su, Y., Zhou, Z., Wei, H., Yang, Z., Sensors and Actuators B **296** (2019) 126666.

[64] Ryu, H.S., Kim, J.S., Park, J., Park, J.Y., Cho, G.B., Liu, X., Ahn, I.S., Kim, K.W., Ahn, J.H., Ahn, J.P., Martin, S.W., Wang, G., Ahn, H.J., Journal of Power Sources **244** (2013) 764-770.

[65] Jiang, N., Tang, Q., Sheng, M., You, B., Jiang, D., Sun, Y., Catalysis Science & Technology **6** (2016) 1077-1084.

[66] Dong, J., Zhang, F.Q., Yang, Y., Zhang, Y.B., He, H., Huang, X., Fan, X., Zhang, X.M., Applied Catalysis B: Environmental **243** (2019) 693-702.

[67] Zheng, X., Han, X., Zhang, Y., Wang, J., Zhong, C., Deng, D., Hu, W., Nanoscale **11** (2019) 5646-5654.

[68] Duan, W., Yan, W., Yan, X., Munakata, H., Jin, Y., Kanamura, K., Journal of Power Sources **293** (2015) 706-711.

[69] Wei, W., Mi, L., Gao, Y., Zheng, Z., Chen, W., Guan, X., Chemistry of Materials **26** (2014) 3418-3426.

[70] Kim, S. Lee, S.H., Lee, Y., Biosensors and Bioelectronics **85** (2016) 587- 595.

[71] Kannan, P.K., Rout, C.S., Chemistry A European Journal Communication **21** (2015) 9355-9399.

[72] Wu, W., Li, Y., Jin, J., Wu, H., Wang, S., Xia, Q., Sensors and Actuators B **232** (2016) 633- 641.

[73] Linganiso, E.C., Mwakikunga, B.W., Mhlanga, S.D., Coville, N.J., Sone, B.T., Maaza, M., 2012 IEEE Sensors Proceedings, Tapei Taiwan (2012) 1-4.

[74] Huang, X-Y., Chi, Z-T., Liu, J., Li, D-H., Sun, X-J., Yan, C., Wang, Y-C., Li, H., Wang, X-D., Xie, W-F., Sensors and Actuators B **304** (2020) 127305.

[75] Ho, T.A., Bae, C., Nam, H., Kim, E., Lee, S.Y., Park, J.H., Shin, H., ACS Applied Materials & Interfaces **10** (2018) 12807-12815.

[76] Hu, P., Liu, X., Liu, B., Li, L., Qin, W., Yu, H., Zhong, S., Li, Y., Ren, Z., Wang, M., Journal of Colloid and Interface Science **496** (2017) 254-260.

[77] Maiaugree, W., Tangtrakarn, A., Lowpa, S., Ratchapolthavisin, N., Amornkitbamrung, V., Electrochimica Acta **174** (2015) 955-962.

[78] Li, J., Wang, S., Xiao, T., Tan, X., Xiang, P., Jiang, L., Deng, C., Li, W., Li, M., Applied Surface Science **420** (2017) 919-926.

[79] Linganiso, E.C., Linganiso, Z.L., Motaung, T.E., Singh, T., Fischer, T., Mathur, S., Mhlanga, S.D., Mwakikunga, B.W., Coville, N.J., 2019 IEEE SENSORS, Montreal, QC, Canada (2019) 1-4.

[80] Lin, T-S., Liu, C-J., Dai, C-S., Applied Catalysis B **154-155** (2014) 213- 220.

[81] Rahman, M.M., Ahmed, J., Asiri, A.M., Siddiquey, I.A., Hasnat, M.A., Journal of the Taiwan Institute of Chemical Engineers **64** (2016) 157-165.

[82] Geim, A.K, Science **324** (2009) 1530-1534.

[83] Schedin, F., Geim, A.K., Morozov, S.V., Hill, E.W., Blake, P., Katsnelson, M.I, Novoselov, K.S., Nature Materials **6** (2007) 652- 655.

[84] Basu, S., Bhattacharyya, P., Sensors and Actuators B **173** (2012) 1- 21.

[85] Nag, A., Mitra, A., Mukhopadhyay, S.B., Sensors and Actuators A **270** (2018) 117- 194.

[86] Meng, F-L., Guo, Z., Huang, X-J., Trends in Analytical Chemistry **68** (2015) 37- 47.

[87] Yoon, H.J., Jun, D.H., Yang, J.H., Zhou, Z., Yang, S.S., Cheng, M.M-C., Sensors and Actuators B **157** (2011) 310-313.

[88] Justino, C.I.L., Gomes, A.R., Freitas, A.C., Duarte, A.C., Rocha-Santos, T.A.P., Trends in Analytical Chemistry **91** (2017) 53- 66.

[89] Robinson, J.T., Perkins, F.K., Snow, E.S., Wei, Z., Sheehan, P.E., Nanoletters **8** (2008) 3137- 3140.

[90] Wang, D.H., Hu, Y., Zhao, J.J., Zeng, L.L., Tao, X.M., Chen, W., Journal of Materials Chemistry A **2** (2014) 17415-17420.

[91] Ghosh, R., Midya, A., Santra, S., Ray, S.K., Guha, P.K., ACS Applied Materials & Interfaces **5** (2013) 7599-7603.

[92] Gui, Y-H., Wang, H-Y., Tian, K., Yang, L-I., Guo, H-S., Zhang, H-Z., Fang, S-M., Wang, Y., Ceramics International **44** (2018) 4900-4907.

[93] Liu, J., Li, S., Zhang, B., Wang, Y., Gao, Y., Liang, X., Wang, Y., Lu, G., Journal of Colloid and Interface Science **504** (2017) 206-213.

[94] Chen, T., Yan, W., Xu, J., Li, J., Zhang, G., Ho, D., Journal of Alloys and Compounds **793** (2019) 541-551.

[95] Park, S.Y., Lee, J.E., Kim, Y.H., Kim, J.J., Shim, Y.-S., Kim, S.Y., Lee, M.H., Jang, H.W., Sensors and Actuators B **258** (2018) 775- 782.

[96] Cheng, M., Wu, Z., Liu, G., Zhao, L., Gao, Y., Zhang, B., Liu, F., Yan, X., Liang, X., Sun, P., Lu, G., Sensors and Actuators B **291** (2019) 216-225.

[97] Sun, J., Sun, L., Han, N., Chu, H., Bai., S., Shu., X., Luo, R., Chen, A., Sensors and Actuators B **299** (2019) 126832.

[98] Shao, S., Che, L., Chen, Y., Lai., Huang, S., Journal of Alloys and Compounds **774** (2019) 1-10.

[99] Namdarian, A., Tabrizi, A.G., Maseloeno, A., Mohammadi, A., Moosavifard, S.E., International Journal of Hydrogen Energy **43** (2018) 17780-17787.

[100] Song, X., Li, X., Bai, Z., Yan, B., Xiong, D., Lin, L., Zhao, H., Li, D., Shao, Y., Carbon **133** (2018) 14-22.

[101] Zhang, Z., Zhao, C., Min, S., Qian, X., Electrochimica Acta **144** (2014) 100-110.

[102] Ou, X., Gan, L., Luo, Z., Journal of Materials Chemistry A **2** (2014) 19214-19220.

[103] Jinlong, L., Tongxiang, L., Meng, Y., Suzuki, K., Miura, H., Journal of Electroanalytical Chemistry **78** (2017) 8-13.

[104] Lin, H., Liu, F., Wang, X., Ai, Y., Yao, Z., Chu, L., Han, S., Zhuang, X., Electrochimica Acta **191** (2016) 705-715.

[105] Zhao, C., Zhang, Z., Wang, Q., Min, S., Qian, X., RSC Advances **5** (2015) 63258-63536.

[106] Tan, C., Zhang, H., Nature Communications **6** (2015) 7873.

[107] Zhu, Y.J., Chen, F., Chemical Reviews **114** (2014) 6462-6555.

[108] Loupy, A., Varma, R.S., Chemistry Today **24** (2006) 39-39.

[109] Motshekga, S.C, Pillai, S.K., Ray, S.S., Jalama, K., Krause, R.W.M., Journal of Nanomaterials **2012** (2012) ID 691503.

[110] Mishra, R.R., Sharma, A.K., Composites: Part A **81** (2016) 78- 97.

[111] Kim, H.W., Na, H.G., Kwon, Y.J., Kang, S.Y., Choi, M.S., Bang, J.H., Wu, P., Kim, S.S., ACS Applied Material & Interfaces **9** (2017) 31667- 31682.

[112] Menéndez, J.A., Arenillas, A., Fidalgo, B., Fernández, Y., Zubizarreta, L., Calvo, E.G., Bermúdez, J.M., Fuel Processing Technology **91** (2010) 1- 8.

[113] Anton Paar

https://wiki.anton-paar.com/en/microwave-assisted-synthesis/ (Accessed 17 September 2019)

[114] Cho, P.S., Kim, K.W., Lee, J.H., Sensors and Actuators B **123** (2007), 1034- 1039.

[115] Shingange, K., Swart, H.C., Mhlongo, G.H., Physica B **535** (2018) 216- 220.

[116] Tshabalala, Z.P., Motaung, D.E., Mhlongo, G.H., Ntwaeaborwa, O.M., Sensors and Actuators B **224** (2016) 841- 856.

[117] Chu. X., Chen, T., Zhang, W., Zheng, B., Shui, H., Sensors and Actuators B **142** (2009) 49-54.

[118] Wan, P., Yang, W., Wang, X., Hu, J, Zhang, H., Sensors and Actuators B **214** (2015) 36-42.

[119] Meng, H., Yang, W., Ding, K., Feng, L., Guan, Y., Journal of Materials Chemistry A **3** (2015) 1174-1181.

[120] Bai, S., Chen, C., Luo, R., Chen, A., Lia, D., Sensors and Actuators **216** (2015) 133-120.

Chapter 2: Microwave synthesis of Ni_3S_2 nanostructures

2.1. Introduction

Transition metal sulfides are an important class of metal chalcogenides because of their respective advantages in various applications including supercapacitors, dye-sensitized solar cells, batteries, water splitting and catalysis [1-9]. From the metal sulfide family, nickel sulfides have received considerable amount of attention because of their unique properties. Nickel sulfide exists in different valence states, such as NiS, NiS_2, Ni_3S_2, Ni_3S_4, Ni_7S_6, etc. [5-7]. This can make it difficult to obtain nickel sulfide nanomaterials with a pure phase, a uniform morphology and size [6, 10]. Among these phases, Ni_3S_2 has become a subject of interest because of its superior properties. It is known to be the most stable and to have better electrical conductivity and electrochemical performance when compared with other nickel sulfides [5, 11]. Jiang et al. [5] synthesized NiS, NiS_2 and Ni_3S_2 under the same conditions for the application in hydrogen evolution reaction (HER). Ni_3S_2 proved to be a better electrocatalysts with higher HER activity due to its larger electrochemical surface area, higher conductivity and unique surface chemistry, which was beneficial for water dissociation.

The composition, structure, size, porosity and morphology of nanomaterials influence their magnetic, optical, chemical and electrical properties [12]. Hence, a great deal of attention has been spent on investigating parameters that allow for the control of the above-mentioned features. Ni_3S_2 with various morphologies has been synthesized employing different synthesis techniques, such as chemical vapour deposition [13], atomic layer deposition [10], electrodeposition [14], mechanical alloying [15], and hydrothermal and solvothermal methods [8, 16-19]. The hydrothermal or solvothermal method using a Teflon-lined autoclave is one of the most reported methods for Ni_3S_2 synthesis thus the effect of different synthesis parameters (for this method) on the morphology have been studied. For example, Duan et al. synthesized different morphologies of Ni_3S_2 for electrode material by changing the sulfur source [8]. Thioacetamide produced nanoflakes, thiourea nanosheets and sodium thiosulfate nanoparticles. In another study, temperature was found to have an influence on the morphology where lower temperatures produced silk-worm structures and higher temperatures nanosheets [16]. The size of the pores of Ni_3S_2 on Ni foam could also be controlled by tuning the reaction time [17]. Mi and co-workers studied the effect of solution polarity on the shape, size and morphology of their Ni_3S_2 structures [18]. They noticed that when they changed the solution polarity of the

solvent by increasing the amount of water added to ethanol, the small cubic nano-or microstructures on the mesh template changed into bamboo shoot-like crystals with a microstructure. They explained that the solubility of thiourea increased as the water content increased which resulted in a more complete reaction. A similar study by Kim [19] showed that using water, ethanol or a mixture of both can produce different morphologies with thioacetamide employed as the sulfur source. In water, dendritic structures were produced, ethanol produced nanoflakes and a 1:1 (v/v) ethanol/water solvent ratio produced cauliflower-like structures. They attributed this to the fact that water is a smaller molecule compared to ethanol thus it is liable to form fractal patterns that can bring flower-like or dendrites forth through a diffusion-limited process.

Even though hydrothermal and solvothermal synthesis methods are the most frequently used routes for nickel sulfide synthesis, the high temperatures and long reaction times are unattractive. Microwave synthesis has been found to be an efficient method that provide reaction times that are more appealing, lower energy consumption and higher product yields [20]. Microwave technology has been used in synthesizing various metal sulfides including PbS nanotubes [21], ZnS nanoparticles [22], NiS_2 nanocubes [23], SnS_2 nanoflowers [24] and globular-like Ni_3S_2 nanoparticles [5]. The use of different power levels, reaction temperatures and times, and precursors and precursor concentrations have been investigated in an attempt to alter the morphology and performance of as-synthesized materials [25-29]. Solvent properties also have significant effects on the structures formed under microwave heating [25, 27, 29]. Depending on the polarity, dielectric properties and other properties, different solvents will interact differently with the microwaves [25, 27, 29-30]. Khoza et al. [27] studied the influence of varying solvents on microwave synthesized ZnO nanoparticles. They explained that the nucleation and growth of the nanoparticles was affected by the polarity of the solvent. Binary solvent systems can also influence the shape and size of the products synthesized using the microwave technique [31].

Annealing is often performed as a post-synthesis procedure to increase the crystallinity of the as-synthesized materials or to confirm the stability of the crystal at a particular temperature [32]. Annealing can also change the structural, morphological, optical and electrical properties of as-obtained materials [32-35]. Microwave assisted hydrothermal synthesized ZnO nanoflowers were annealed in air at 200, 400 and 600℃ [33]. The well-defined flower-like structure made up of multi-nanorods were transformed into randomly orientated worm-like

structures after annealing. Furthermore, an increase in the annealing temperature caused a decrease in the PL intensity as well as a decrease in the electron spin resonance signal. Nickel sulfide annealing is known to produce phase changes as sulfur is released from the crystal structures [36-38]. Baleyava et al. [36] studied the effect of thermal annealing on properties of nickel sulfide nanostructures synthesized using a successive ionic layer adsorption and reaction (SILAR) method. The authors reported a structural phase transition upon annealing. The as-synthesized Ni_3S_4 structures were annealed for 8 hrs at three different temperatures (100, 150 and 180℃) in air and in vacuum. Annealing in vacuum produced a mixture of Ni_3S_4 and Ni_9S_8. When annealing occurred in air, two additional nickel structures emerged ($NiSO_4.7H_2O$ and $NiO\text{-}SO_4\text{-}H_2O$). Annealing of NiS in both air and vacuum produced NiS and Ni_7S_6.

In this present work, the synthesis of Ni_3S_2 nanostructures using a simple microwave-assisted method is reported. The effect of employing water, ethanol, ethylene glycol or a binary solvent system consisting of water and ethylene glycol or water and ethanol on the nanostructures was studied. The influence of annealing on the composition and morphology of the nanostructures synthesized using only water as a solvent was also explored.

2.2. Experimental procedure

Nickel (II) chloride hexahydrate ($NiCl_2.6H_2O$, 98%), thiourea (CH_4N_2S, 99%), anhydrous ethylene glycol ($C_2H_6O_2$, 99.8%) and ethanol (CH_3CH_2OH, 99%) were all used without any further purification, as received from Sigma Aldrich, South Africa.. A 15% H_2O_2 solution was prepared by diluting a purchased H_2O_2 (30%, Sigma Aldrich, South Africa) solution with distilled water. Hydrogen (H_2, 99.98%) was obtained from Afrox and used for annealing.

2.2.1. Synthesis of Ni_3S_2

The method employed to synthesize several Ni_3S_2 nanostructures was similar to the one reported in [38] with a few modifications. In a typical reaction, 1.189 g $NiCl_2.6H_2O$ and 0.485 g of thiourea were dissolved in 22.5 mL of solvent. 2.5 mL of a 15 wt. % H_2O_2 solution was added to the mixture and stirred for 5 minutes in order to obtain a homogeneous solution. The mixture was then transferred into the Teflon-lined microwave reaction vessels and placed in a microwave reactor (Anton Paar Multiwave 3000) which was operated at 600 W for 6 minutes followed by fan cooling to room temperature. The formed black precipitate was washed several times with distilled water and ethanol and finally dried in an oven at 60℃ for 12 hours. The solvent was comprised of ethanol and/or water and ethylene glycol and/or water. The volume

ratio between ethanol and water as well as between ethylene glycol and water was set to 1:0, 2:1, 1:1, 1:2 or 0:1. The samples were labelled as NS-W for nickel sulfide synthesized in water, NS-Et/W (ratio) and NS-EG/W (ratio) for the samples prepared in the different ethanol/water and ethylene glycol/water solvent compositions.

2.2.2. Thermal annealing under hydrogen

About 120 mg of the as-synthesized product using water as solvent (NS-W) was weighed and annealed under a hydrogen atmosphere in a horizontal quartz tube furnace. The annealing was carried out at 300, 400 and 500℃ for 30 minutes under a hydrogen flow (50 sccm) and a ramping rate of 5 ℃/min. The effect of annealing for a longer period at the same flow rate (60 min) and at a higher flow rate (100 sccm) at 300℃ were also examined.

2.3. Characterization

Powdered X-ray diffraction (PXRD) patterns of the obtained black powders were collected on a Bruker D2 phaser diffractometer with a Cu-Kα (λ= 0.154 nm) radiation source. The scan range was $5° \leq 2\theta \leq 90°$ in a 0.02° measurement step.

Transmission electron microscopy (TEM) established the morphologies of the obtained material using a Tecnai Spirit T12 instrument at 120 keV. A small amount (~2 mg) of the powder was dispersed in about 5 mL of ethanol by ultra-sonicating the solution for 10-15 minutes to ensure homogeneity. A few drops of the solution were placed on a carbon coated copper grid and then dried in ambient air before inserting it in the microscope.

High magnification TEM micrographs were obtained using a JEOL JEM-2100F transmission electron microscope equipped with a LaB6 source with the instrument operated at an acceleration voltage of 200 kV, fitted with a Gatan CCD camera. The specimens were prepared in the same way as the TEM samples.

Brunauer-Emmet-Teller (BET) method was employed for specific surface area analysis. The N_2 adsorption and desorption isotherms of the nickel sulphide structures were taken using a Micrometrics Tristar 3000 instrument at 77 K. All the samples were degassed before analysis at 423-473 K in N_2. By analysing the desorption branches of the N_2 isotherms, the pore size distribution was determined and calculated using the Barett-Joyner-Halenda (BHJ) method.

Fourier transform infrared (FTIR) spectroscopy was carried out using a Bruker Vector 22 FT-IR spectrometer to ascertain the surface functional groups on the nickel sulphide. The spectra were collected from 500 to 3500 cm^{-1}.

Laser Raman spectroscopic analysis was performed to determine the vibrational modes of the synthesized nickel sulfide. The measurement was done using a Horiba LabRAM Raman spectrometer equipped with an Olympus BX41 microscope attachment.

The chemical composition of the nickel sulfide synthesized with water as a solvent was determined by X-ray photoelectron spectroscopy (XPS). Measurements were recorded on a Physical Electronics Quantum 2000 using a monochromatic Al Kα source operated at 1486.7 eV.

2.4. Results and discussion

2.4.1. Effect of solvent composition on nanostructures

2.4.1.1. Phase analysis

Powder X-ray diffraction (PXRD) was performed to investigate the crystal phase and structure of the nickel sulfide structures synthesized using different solvent compositions. The diffraction peaks positioned at 2θ = 21.8°, 31.1°, 37.9°, 38.3°, 44.4°, 49.9°, 50.3°, 54.8°, 55.4°, 69.3°, 73.0°, 77.9°, 85.7° and 89.0° could be indexed to the (101), (110), (003), (021), (202), (113), (211), (104), (122), (303), (214), (401), (321) and (116) crystal planes of the rhombohedral Ni_3S_2 (PDF 00-030-0863) phase, respectively with lattice constants a = 5.74650 Å and c = 7.13490 Å (**Fig. 2.1**a). The impurity peaks situated at 2θ = 11.2°, 18.2° and 35.6° could be assigned to a possible (001) plane of carbon [39], and (110) and (021) planes of hexagonal millerite (NiS PDF 01-074-7239). Nickel sulfide formation could possibly be explained by reactions that occur between $NiCl_2$, thiourea and hydrogen peroxide below (**Eq. 2.1**-**2.6**) [40-43]. Firstly, the thiourea reacted with hydrogen peroxide to form thiourea dioxide (**Eq. 2.1**) which decomposed into urea and sulfoxylate (**Eq. 2.2**). The sulfoxylate underwent a few other reactions to produce sulfide ions (**Eq. 2.3**). The nickel salt was reduced to Ni (**Eq. 2.4**).The released S^{2-} ions **(Eq. 2.3**) reacted with Ni to produce Ni_3S_2 (**Eq. 2.5**) or NiS (**Eq. 2.6**). According to thermodynamics, Ni_3S_2 has a lower melting point than NiS as well as a lower free energy of formation [44]. Consequently, under the same reaction conditions, Ni_3S_2 formation will be more likely to occur than NiS formation.

$$(NH_2)_2CS \xrightarrow{H2O2} (NH_2)_2CSO_2 + H_2O \qquad (\mathbf{2.1})$$

$$NH(NH_2)CSO_2^- + H_2O \rightarrow (NH_2)_2CO + HSO_2^- \quad (\mathbf{2.2})$$

$$HSO_2^- \rightleftarrows SO_3^{2-} + H_2O + S^{2-} \quad (\mathbf{2.3})$$

$$Ni^{2+} + 2e^- \rightarrow Ni \quad (\mathbf{2.4})$$

$$2S^{2-} + O_2 + H_2O + 3Ni \rightarrow Ni_3S_2 + 4OH^- \quad (\mathbf{2.5})$$

$$S^{2-} + O_2 + H_2O + Ni \rightarrow NiS + 4OH^- \quad (\mathbf{2.6})$$

The carbon side product that formed during the hydrolysis reaction of thiourea in the formation of metal sulfides has previously been proposed as either NH=C=NH or H_2N-C≡N [45]. Furthermore, some of the thiourea or urea might also still be present in our final product [41].

The solvolysis reaction in ethanol did not seem to have reached completion due to the insolubility of thiourea in ethanol (**Fig. 2.1**b). As the polarity of the solvent increased (addition of water to ethanol), so did the number of peaks designated to Ni_3S_2 as well as the crystallinity of the as-synthesized material. This was due to the increased available amount of S^{2-} ions. However, the impurity peaks persisted in all the samples prepared in the Et/W solvent system. Some of these impurity peaks could be indexed to hexagonal NiS and Ni_7S_6 (PDF 00-014-0364) suggesting that a mixture of nickel sulfide phases was obtained in the Et/W solvent system with Et/W 1:2 producing most prominent peaks belonging to Ni_3S_2. When EG was used as a solvent, all the characteristic Ni_3S_2 were obtained with impurity peaks belonging to hexagonal NiS and rhombohedral NiS (PDF 00-001-1286) (**Fig. 2.1**c). When a binary solvent system consisting of water and ethylene glycol was employed a highly pure phase of Ni_3S_2 was obtained. We noticed that the crystallinity of NS increased with an increase in solution polarity (**Fig. 2.1**d). Also, the diffraction peaks shifted 2θ values with an introduction of EG to the solvent system.

In all the samples, the most intense peak was the (110) plane indicating the preferential growth of the crystals in this direction. Therefore, the average crystallite sizes of NS-W and NS-EG/W samples were calculated based on the width of this plane using the Scherrer equation:

$$D = \frac{k\lambda}{\beta cos\theta} \quad (\mathbf{2.6})$$

Where, D is the average crystal size, k is a constant usually applied as 0.9, λ is the wavelength of the X-ray used which is 0.154 nm for the CuKα, β is the full width at half maximum (FWHM) and θ is Bragg's angle of reflection. The estimated crystallite sizes (**Table 2.1**)

calculated using equation (**2.6**) suggest that the crystallite sizes of the synthesized material decreased with a decreasing polarity of the nature of the solvent, which corresponded to the increase in the FWHM of the XRD peaks. This may be explained by the high viscosity of EG that could influence the mobility of the primary particles and in turn also influence the effective collision rates [46]. The dominance of EG in the solvent system could imply that it was highly adsorbed on the inorganic surfaces and was able to induce steric hindrance which may have limited the growth process and caused crystal size reduction.

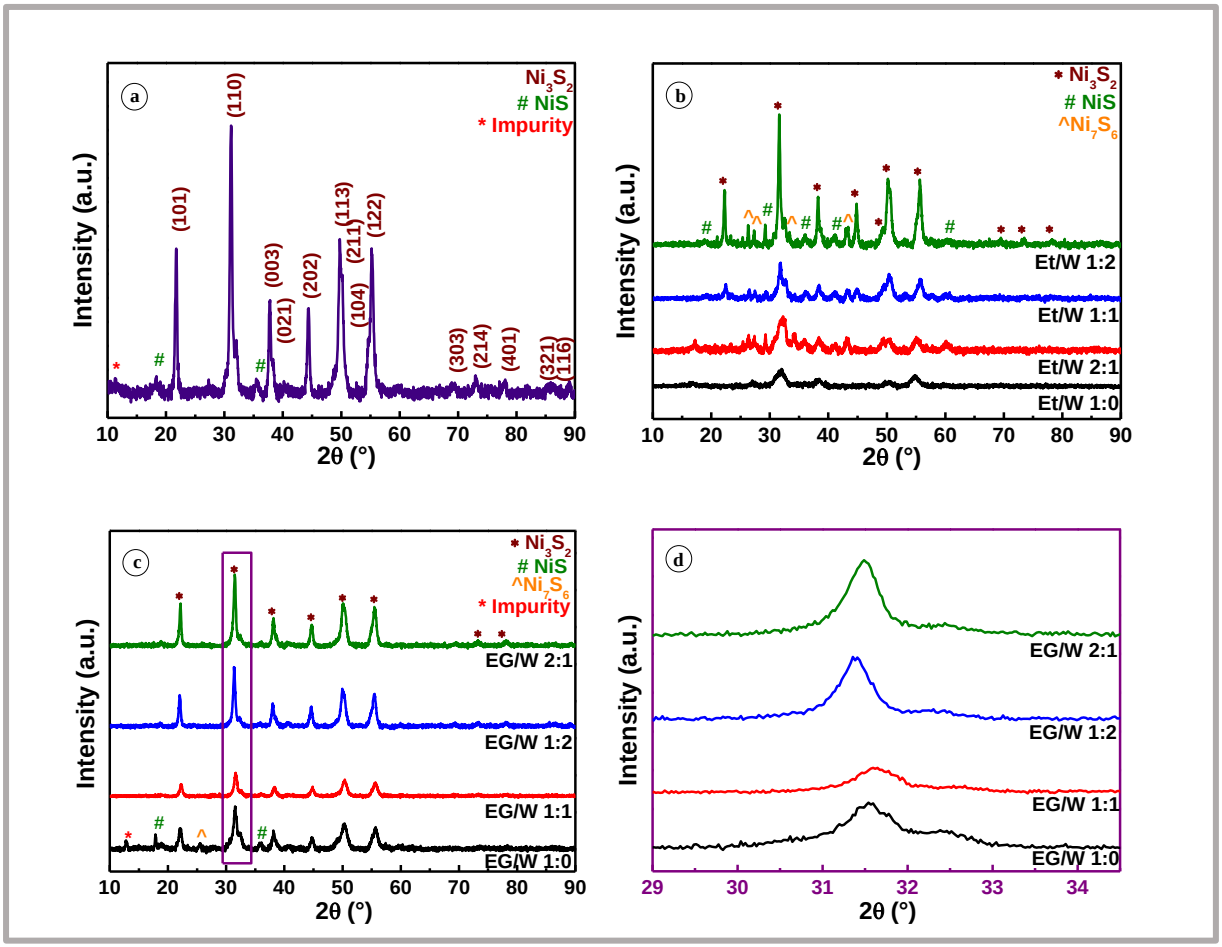

Figure 2. 1. XRD patterns of the as-prepared nickel sulfides: (a) prepared in only water as solvent, (b) prepared in EG/water solvent compositions, (c) prepared in EtOH/water solvent compositions, and a zoomed in spectra of the (110) peak orientation of samples prepared using water and/or EG as solvent showing a shift in peak position as a result of different solvent compositions.

Table 2. 1. Crystallite sizes of NS samples prepared in water and/or ethylene glycol.

Sample	**(110) Plane (2 θ (°))**	**FWHM (°)**	**Crystallite size (nm)**
NS-W	31.14	0.5187	15.90

NS-EG/W 1:2	31.47	0.5481	15.06
NS-EG/W 1:1	31.38	0.5425	15.21
NS-EG/W 2:1	31.64	0.7389	11.18
NS-EG/W 1:0	31.61	1.2348	6.69

2.4.1.2. IR absorption properties

FTIR spectroscopy was performed on the NS-W and NS-EG/W samples as illustrated in **Fig. 2.2**. The peak at around 633 cm^{-1} was ascribed to the Ni-S stretching vibration [47-49]. The C=S asymmetric stretching frequency at 741 cm^{-1} confirmed the metal-sulfur coordination bond [48, 49]. The out of plane NH_2 wagging of the amine group was located at 900 cm^{-1} [41]. The latter was less pronounced in the samples prepared in the EG/W solvent system. The peak at ~ 1079 cm^{-1} was assigned to the S=O stretching mode of the air oxidized sulfur [38, 47, 49], but it could also be due to the C-N stretching vibrations from the thiourea [48]. Another C-N stretching vibration was noted at 1249 cm^{-1} [50]. This band was more visible in the nickel sulfide structures produced in using the EG/W solvent system. A NH_2 bending mode was observed at 1622 cm^{-1} [48]. This peak could also be possibly due to bending vibrations of the OH group from H_2O [38, 46]. Lastly, a C-H stretching vibration from thiourea was observed at ~ 2893 cm^{-1} [48, 50]. The peaks at ~ 2300 cm^{-1} could possibly be due to moisture and CO_2 during analysis.

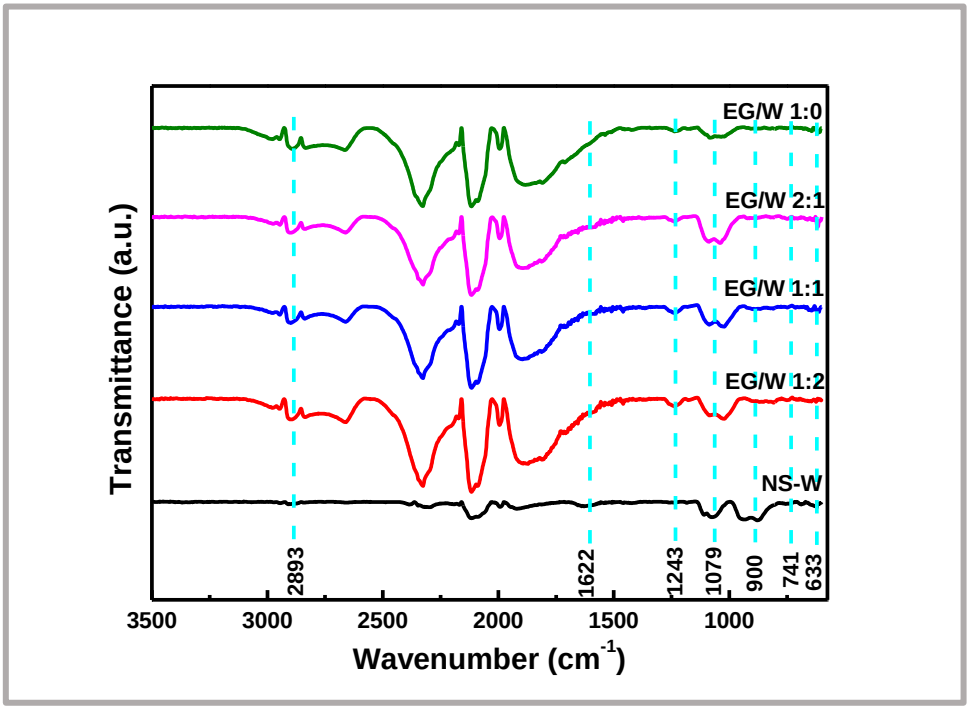

Figure 2. 2. FTIR spectra of NS-W and NS-EG/W samples.

2.4.1.3. Morphology analysis

The effect of using different solvents on the morphology of the nickel sulfide nanostructures was examined using TEM micrographs as shown in **Fig. 2.3**. The reaction occurring in water produced interconnected quasi-spherical flower-like nanostructures made up of fibrous nanosheets (**Fig. 2.3**a&b). An introduction of EG to water produced densely packed layered based flower-like structures with no distinct shape (**Fig. 2.3**c-h). When an equal volume of EG and water was employed, the nanostructures had a wrinkled few layer based morphology, that appeared to be less dense. When only EG was used as solvent, smaller nanosheets seemed to overlap before forming agglomerates.

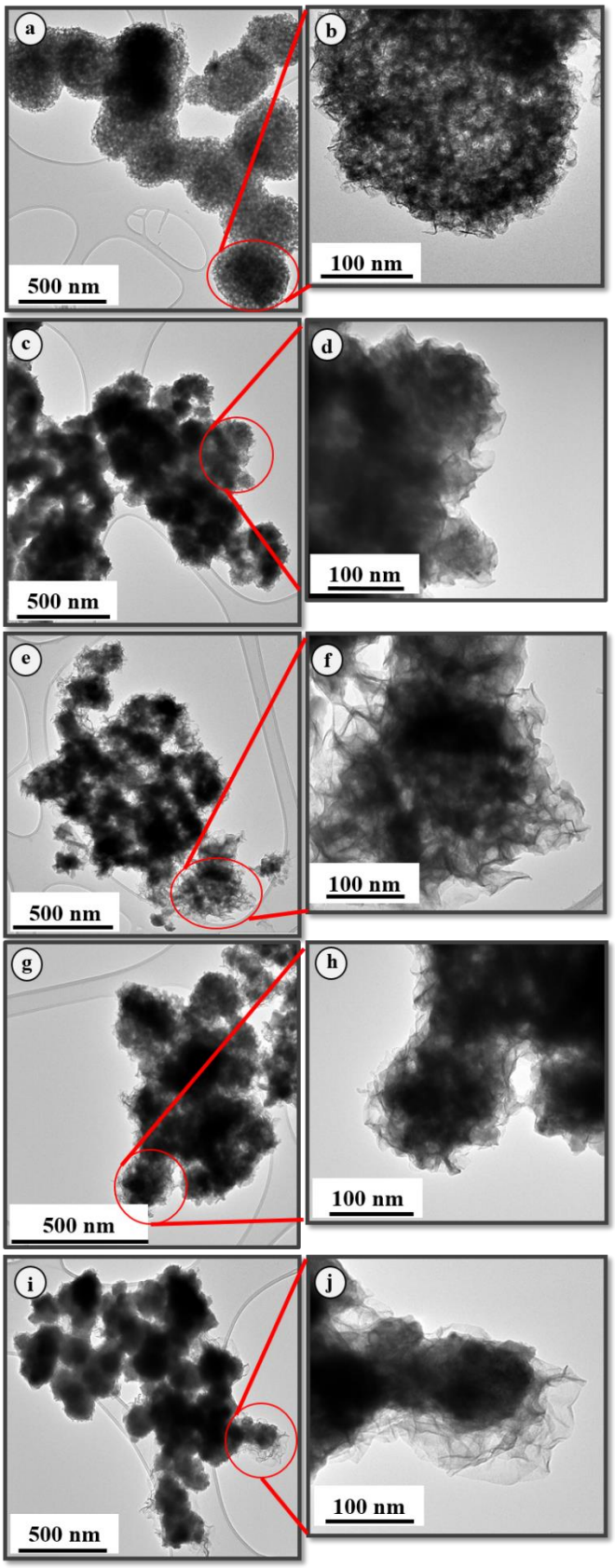

Figure 2. 3. TEM micrographs of: (a, b) NS-W, (c, d) NS-EG/W 1:2, (e, f) NS-EG/W 1:1, (g, h) NS-EG/W 2:1, and (i, j) NS-EG/W 1:0.

Scheme 2.1 is a proposed growth mechanism of the nickel sulfide nanoflowers. Nanocrystalline nuclei formed during the hydrolysis or solvolysis process, which gradually produced nanoparticles or crystals [51]. These crystals grew into nanosheets. These individual nanosheets have a surface energy that was quite high with two main exposed planes. Hence, they showed a tendency to aggregate perpendicularly to the surface planes so as to decrease the surface energy by reducing the number of exposed areas. The nanosheets gradually self-orientated and assembled into flower-like hierarchical structures under dipolar fields associated with hydrogen bonds and van der Waals forces [51, 52]. The nanoparticles that formed during nucleation in the hydrothermal reaction have higher collision rates than those formed in the solvothermal reaction because water has a lower viscosity thus forming small nanosheets [46]. Secondly, EG has a lower saturated vapour pressure and a higher boiling point thus amalgamation of the nuclei was less compared to that which took place with water since water has a higher saturated vapour pressure and lower boiling point [25]. Moreover, ethylene glycol has a bulkier structure than water [53]. Therefore, the flower-like structures that formed when water was used as solvent were marigold-like whereas the ones formed during the solvolysis reactions were rose-like (**Scheme 2.1**).

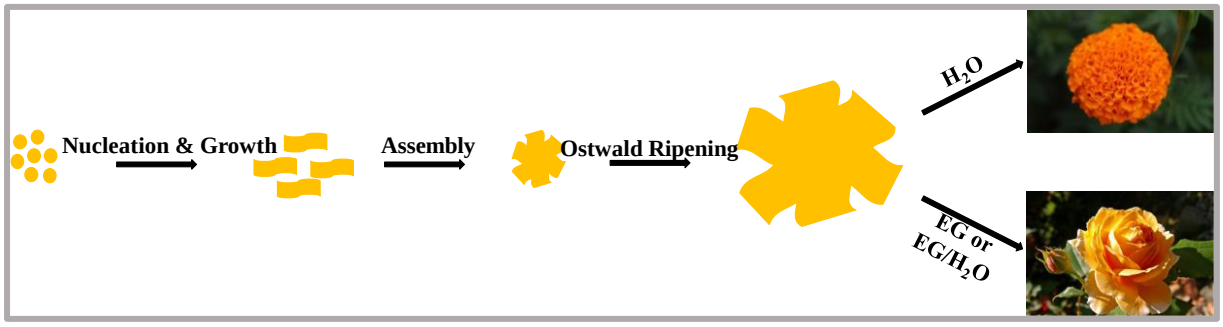

Scheme 2. 1. Proposed growth mechanism of Ni_3S_2 nanoflowers [55].

Since the synthesis was performed under microwave radiation, the dielectric properties of the solvents should also be taken into consideration when attempting to explain the mechanism of formation. Microwave heating occurs by converting microwave radiation into thermal energy [30]. The value of the dielectric loss tangent (tan δ) could be used to describe the heating efficiency of the solvent via microwave radiation. The higher the tan δ value the faster the conversion of microwave irradiation into thermal energy. EG has a high dielectric loss tangent (tan δ) compared to water (**Table 2.2**) meaning it has an enhanced interaction with the microwave radiation [25, 30] and the reaction would be expected to occur faster in EG compared to in water. However, due to the higher viscosity and higher boiling point of EG the

reaction would still be slower thus producing larger nanosheets. In a similar study, Krishnapriya [25] also obtained marigold flower-like ZnO in water during microwave assisted synthesis, but ZnO with a rotor-like morphology when EG was employed as solvent.

Table 2. 2. Boiling point, dielectric constant (ε) and the dielectric loss tangent (tan $\boldsymbol{\delta}$) of the solvent used in present work [30].

Solvent	**Boiling point (℃)**	ε	**tan $\boldsymbol{\delta}$**
Water	100	80.0	0.123
Ethylene glycol	198	38.0	1.350

2.4.1.4. BET surface area analysis

The N_2 adsorption-desorption isotherms of the obtained nickel sulfides are shown in **Fig. 2.6**a&b. It can be seen from **Fig. 2.6**a that the isotherm of NS-W has a type III isotherm with a H3 hysteresis loop at relative pressure (P/P_0) of 0.4-1.0, characteristic of mesoporous materials [24, 55-56]. Its corresponding pore size diameter distribution curve (inset) showed a narrow pore size distribution between 4 and 16 nm, which was in the mesoporous region. The N_2 isotherms for the NS-EG/W samples also exhibited type III isotherms, but a bimodal pore size distribution (**Fig. 2.6**b). The curves have a broad tailing peak located at $>$ 4 nm and a sharp peak centred at approximately 89, 68, 58 and 57 nm for NS-EG/W 1:0, 2:1, 1:2 and 1:1, respectively. This could suggest the presence of pores in the mesopores region (2-50 nm) and the macropore region ($>$50 nm). The nanopetals could possibly be responsible for the small pores and the internanopetal spaces for the larger pores [24]. The width of the tailing peak increased as the EG content in the solvent increased. The largest pores were also observed in the sample synthesized with a solvent with the highest EG content. This could suggest that the size distribution of the pores in the nanopetals became larger as EG became the more dominating solvent as well as the voids between the nanopetals.

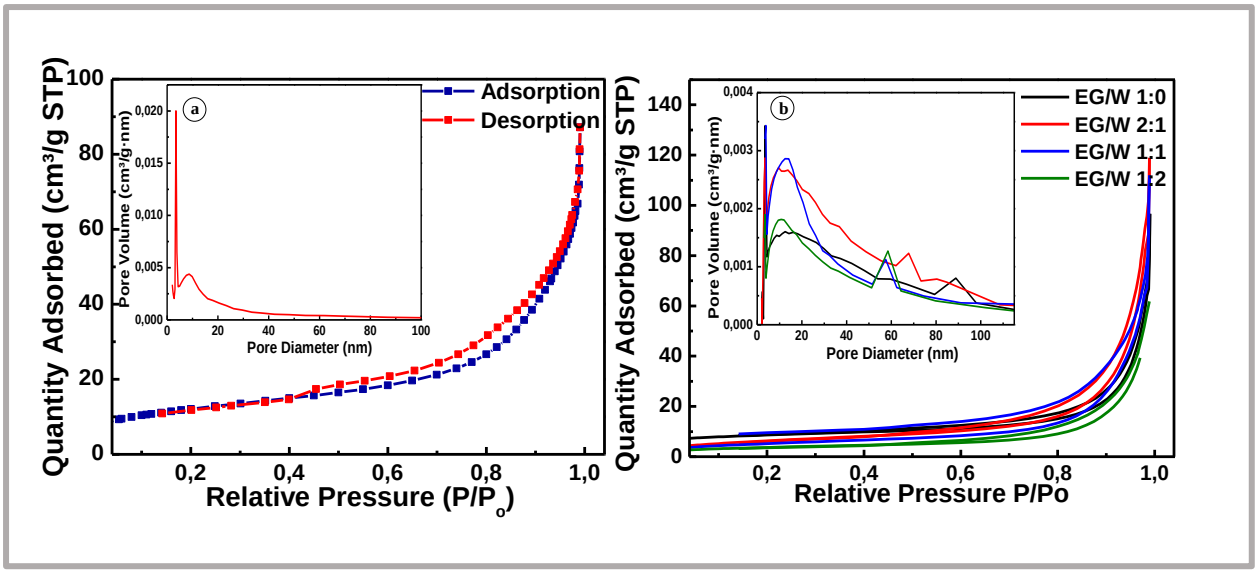

Figure 2. 4. N_2 adsorption-desorption isotherms and pore size distribution curves (inset) of (a) NS-W and (b) NS-EG/W nanostructures.

The specific surface area for the samples was calculated using the BET method. The specific BET surface area of NS-W was ~ 42.3 m^2/g (**Fig. 2.5**). When ethylene glycol was introduced to the water, the surface area decreased to almost a third of the NS-W surface area. Thereafter, it gradually increased with an increase in the amount of ethylene glycol in the solvent. Similar results were obtained when Wojnarowicz *et al.* [31] studied the effect of water content in ethylene glycol on ZnO nanoparticles synthesized via a microwave solvothermal method.

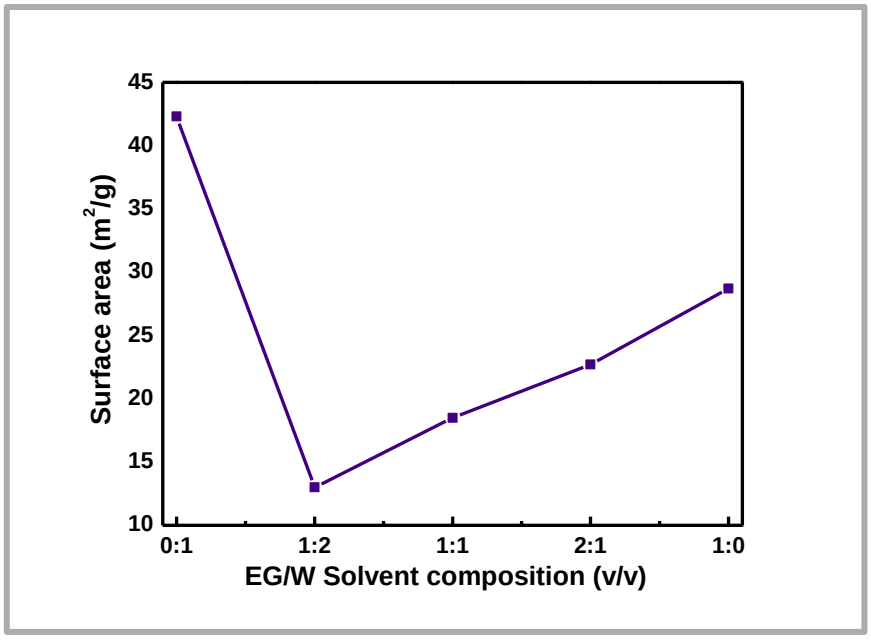

Figure 2. 5. Values of the specific surface area of the structures synthesized at different EG/W solvent compositions.

According to the experimental results, the solvent composition does have an influence on the final phase purity, structure and morphology of the nickel sulfide.

2.4.1.5. Laser Raman spectroscopic analysis

The Raman spectrum in **Fig. 2.6** of NS-W also served as additional confirmation for the formation of Ni_3S_2 in water. Ni_3S_2 has a rhombohedral structure with the space group *R*32 (155) [57-59]. Theoretically, the phonon modes at the Γ point for Ni_3S_2 are:

$$\Gamma\ (Ni_3S_2) = 2A_1^R + 2A_2^{IR} + 4E^{R,IR} \qquad (\mathbf{2.7})$$

Where, six of the bands are Raman-active bands (two A_1 and four E) and six Infrared-active (two A_2 and four E). The Raman spectrum exhibited peaks at approximately 196, 217, 301, 322, and 342 cm^{-1} which could be assigned to the E(4), E(3), E(2), A_1(1) and E(1) modes, respectively [55-56].

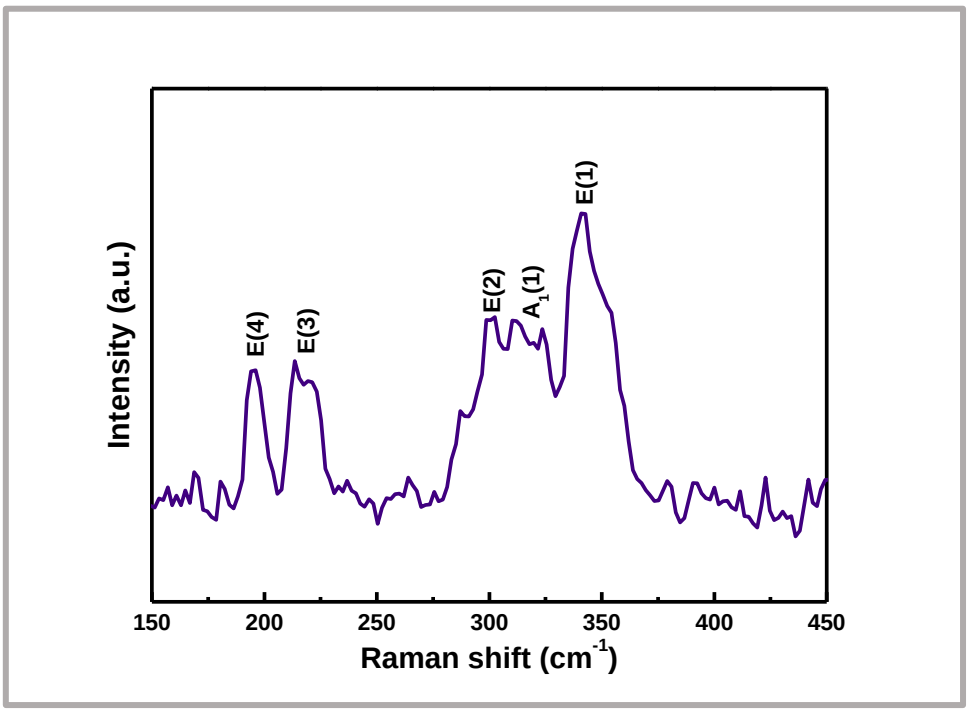

Figure 2. 6. Raman spectrum of Ni_3S_2 nanostructures prepared in water as solvent.

2.4.1.6. Elemental analysis

X-ray photoelectron spectroscopy was performed to ascertain the surface electronic state and chemical composition of NS-W. All observed peaks in the survey spectra as displayed in **Fig. 2.7**a could be assigned to the anticipated elements including Ni, S, O and C. C is usually denoted as adventitious [6], but in this case it could also be due to the side product that formed during synthesis as explained earlier and the O signal could be due to the partial oxidation of

the nickel sulfide during sample preparation for XPS measurement. **Fig. 2.7**b shows the high-resolution spectrum of Ni 2p exhibiting two major peaks at 857.2 eV and 875.1 eV, with a spin energy of 17.9 eV, assigned to Ni $2p_{3/2}$ and Ni $2p_{1/2}$, respectively [16]. The other peaks located at 862.3 eV and 879.9 eV were accompanying satellite peaks of Ni $2p_{3/2}$ and Ni $2p_{1/2}$ [16, 60]. The S 2p region in the binding area range of 160 -174 eV was demonstrated in **Fig. 2.7**c. The peaks located at 163.9 eV and 165.6 eV were ascribed to the S $2p_{3/2}$ and S $2p_{1/2}$ for the S-Ni bonds [16, 60].

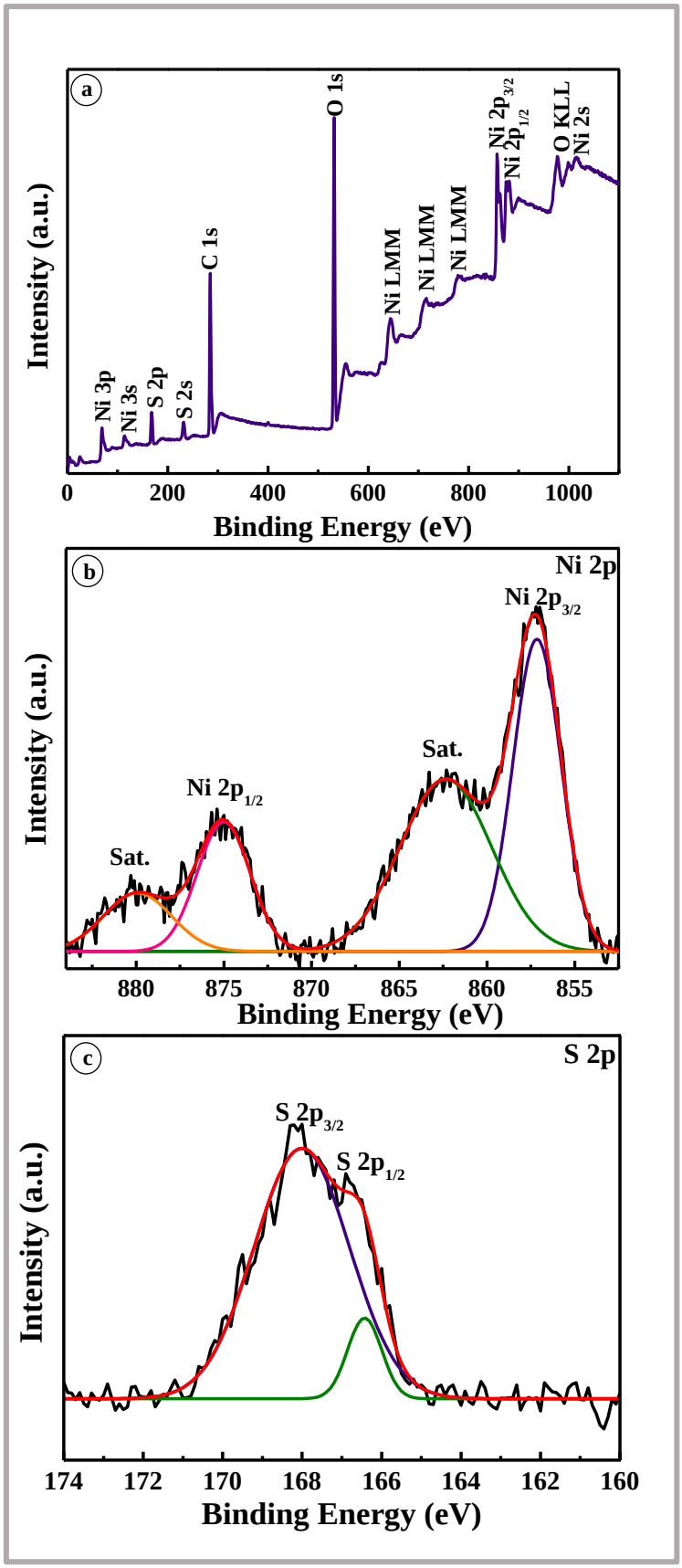

Figure 2. 7. XPS profiles of the as-prepared Ni_3S_2 produced with only water as the solvent: survey spectra of all elements present (a); Ni 2p spectrum (b); and S 2p spectrum (c).

2.4.2. Effect of annealing: phase, IR absorption and morphology studies

When Linganiso *et al*. [61] used NiS for hydrogen sensing at 300℃ they noticed that the structure changed to Ni_3S_2 after sensing. Therefore, in attempt to obtain pure Ni_3S_2, we annealed NS-W under pure H_2 gas. X-ray analysis of the material was performed to study the crystal structure of NS-W after annealing (**Fig. 2.8)**. When samples were annealed at 300℃, an enhancement in the intensity of the diffraction peaks occurred. Additionally, only rhombohedral Ni_3S_2 (PDF 00-030-0863) was obtained at this temperature. The impurity peak was removed and the NiS (PDF- 01-074-7239) peaks at 2θ = 11.2°, 18.2° and 35.6° were all absent after annealing. An increase in annealing temperature to 400℃ produced diffraction planes ascribed to Ni_3S_2, NiS and Ni_7S_6 (PDF 00-014-0364). The same mixture of nickel sulfide polymorphs were obtained at 500℃.

The graph in **Fig. 2.9** demonstrates the effect of annealing temperature on the (110) plane position and the crystallite size. It was evident that the (110) plane position shifted to higher 2θ values and the estimated crystallite size decreased with an increase in annealing temperature. Nanostructures annealed at 300℃ demonstrated the most improvement in the crystal structure and grain growth occurred at this temperature. However, once the annealing temperature was higher, the crystallinity of Ni_3S_2 decreased due to a break in the crystal structure as sulfur was released and other nickel sulfide phases emerged. The shift to higher 2θ values may have been related to a decrease in the lattice parameters from the strain produced by crystallization during the annealing process [62].

An extended annealing time and an increase in the gas flowrate greatly decreased the crystallinity of the structures (**Fig. 2.8**b). This decrease in crystallinity was observed with the increase in the FWHM of the diffraction planes (**Table 2.3**). The nickel sulfide XRD reflection planes also shifted to higher 2θ values upon an increase of annealing time as well as when the flowrate was increased (**Table 2.3**). No new peaks were observed with a prolonged annealing time, but new peaks assigned to NiS and Ni_7S_6 appeared when the gas flowrate was doubled.

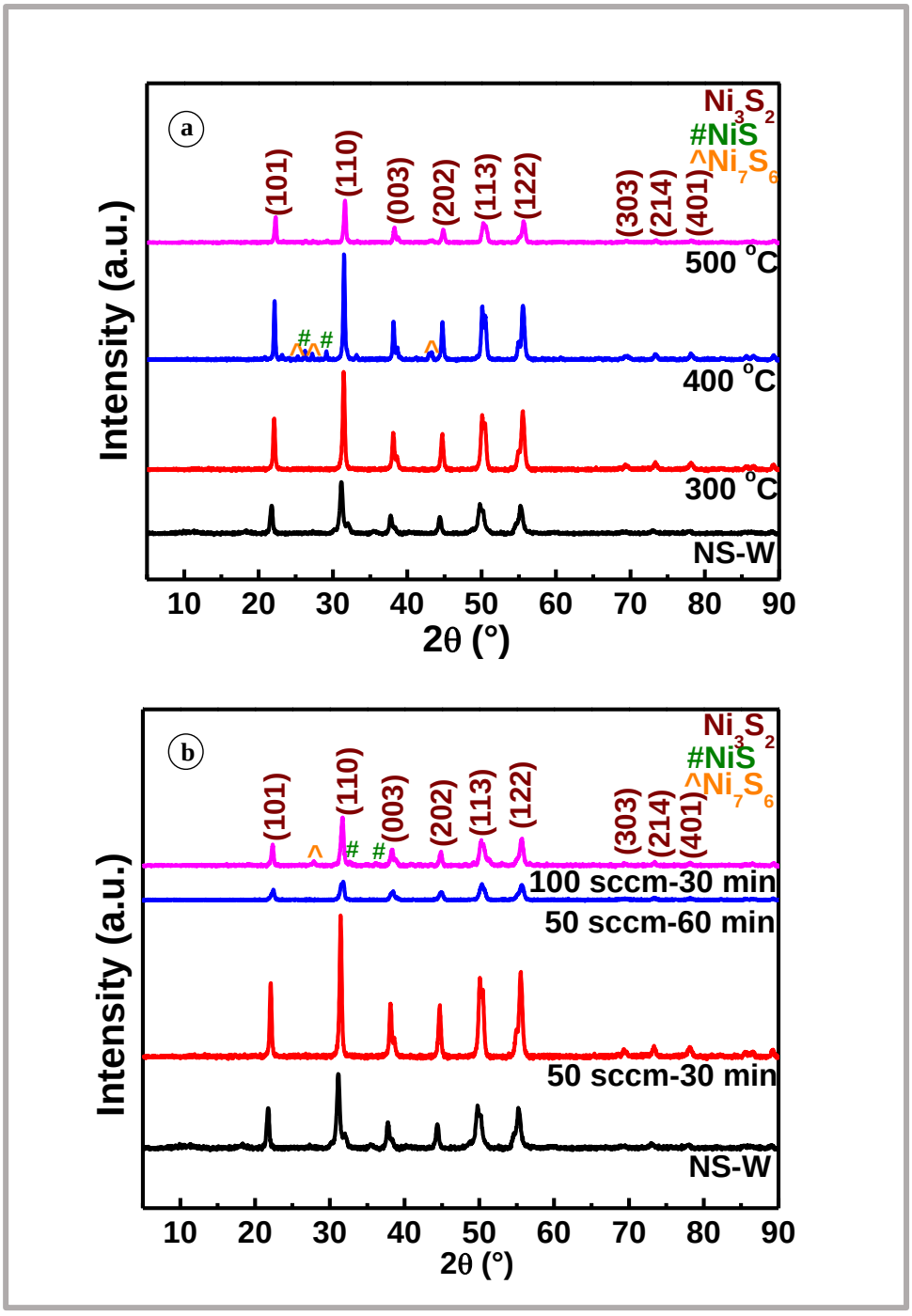

Figure 2. 8. XRD patterns of NS nanostructures annealed under H_2 gas with (a) a flow rate of 50 sccm at different temperatures and (b) for different times at a flow rate of 50 sccm, and at 100 sccm for 30 min.

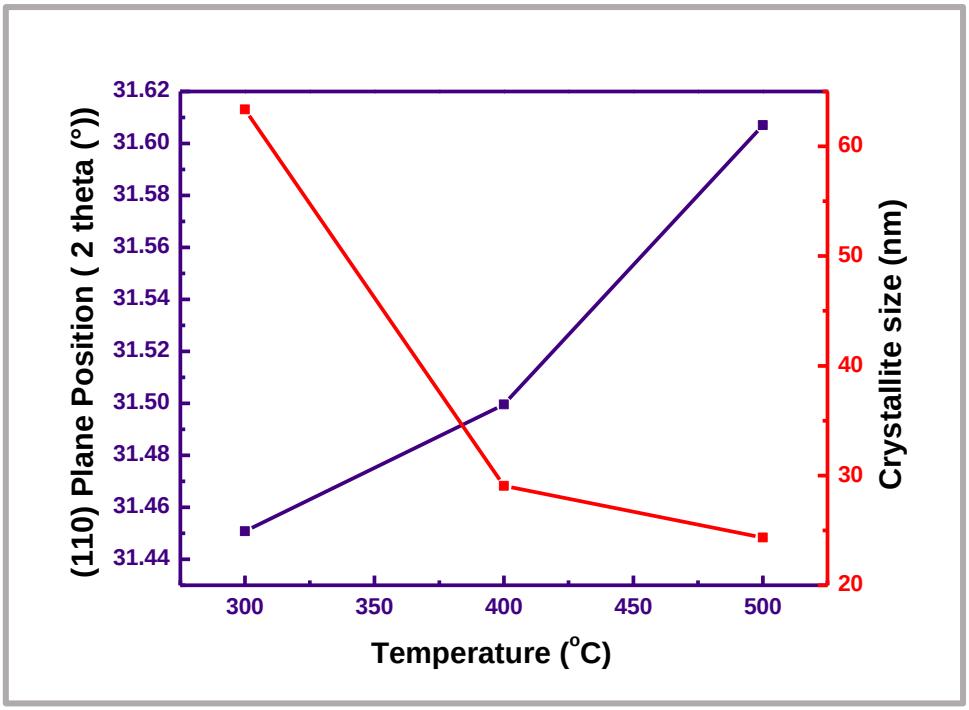

Figure 2. 9. Peak shift vs estimated crystallite size as a function of temperature for the (110) plane of NS.

Table 2. 3. Crystallite sizes of the NS samples annealed at 300℃.

Sample	(110) Plane (2 θ (°))	FWHM (°)	Crystallite size (nm)
NS-W	31.14	0.5187	15.90
300 ℃- 50 sccm (30 min)	31.45	0.3027	63.35
300 ℃- 50 sccm (1 hr.)	31.67	0.6136	13.46
300 ℃- 100 sccm (30 min)	31.67	0.4576	18.04

Other researches have also performed annealing studies of nickel sulfides [34, 37, 40, and 63]. Zhang and co-workers [40] improved the crystallinity of Ni_3S_2 nanorods synthesized on nickel foam by annealing the structures for 4 hours at 300℃ under argon gas. No additional nickel sulfide phases were observed after annealing. Another group was able to prepare Ni_3S_2 by exposing $NiSO_4 \cdot 3NH_4$ and $NiSO_4 \cdot 7H_2O$ to an Ar/H_2 environment at 400℃ for 2 hours [63]. They were able to successfully convert SO_4^{2-} to S_2^{4-}. However, when $NiSO_4 \cdot 3NH_4$ and $NiSO_4 \cdot 7H_2O$ was exposed to only argon gas only $NiSO_4$ structures were obtained suggesting that H_2 was also important for the conversion. Mahmood [37] was able to produce Ni_3S_4 nanoparticles on N-doped graphene with another phase ($NiS_{1.03}$) depending on the temperature

of annealing under N_2 gas. Additionally, the sensing tests performed by Linganiso were under a nitrogen environment [61]. At this background, one could assumedly say that performing annealing under an ultra-pure hydrogen environment could be the reason for a mixture of nickel sulfide phases at temperatures of 400℃ and 500℃.

FTIR spectroscopic analysis revealed a loss (**Fig. 2.10**) in the NH_2 bending mode, which was situated at 1622 cm^{-1} in NS-W after annealing. The peaks located at 653 cm^{-1}, 1053 cm^{-1} and 1164 cm^{-1} indicated the presence of vibrational modes due to sulfide ions in the crystal [38, 47-49]. The intensity of the peak related to S=O (1053 cm^{-1}) increased with an increase in annealing temperature, time and flowrate. The Ni-S peak (653 cm^{-1}) shifted to a higher wavenumber with an increase in annealing temperature, time and flowrate [47-49]. The out-of-plane NH_2 wagging of an amine group was situated at ~ 874 cm^{-1} [41]. The C-N stretching vibration located at ~ 1233 cm^{-1} [50] was present in all annealed samples. The C-H stretching vibrations was also present around 2888 cm^{-1} [48, 50]. The shift in some of the peaks as well as a change in the intensity may possibly be related to a change in the lattice parameters of the nickel sulfide [64]. The peaks around 2300 cm^{-1} could be related to the moisture during analysis.

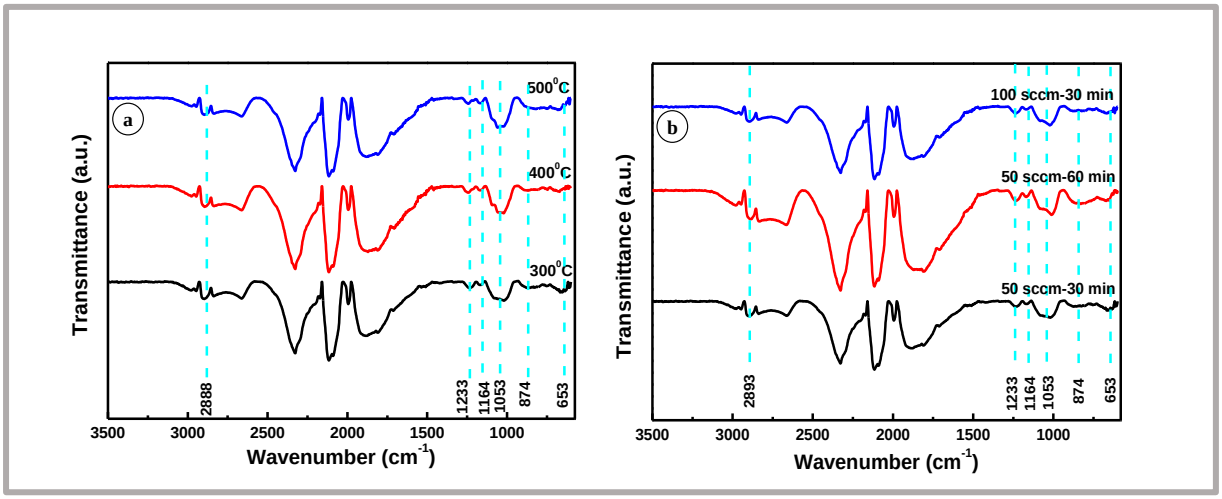

Figure 2. 10. FTIR spectra of NS nanostructures annealed under H_2 gas with (a) a flow rate of 50 sccm at different temperatures and (b) for different times at a flow rate of 50 sccm, and at 100 sccm.

The TEM micrographs of the annealed NS samples were observed to vary with an increase in temperature as illustrated in **Fig. 2.11**. When the NS was annealed at 300℃, nanorods with

dense centres seemed to emerge from the nanosheets of the previously quasi-spherical flowerlike structures forming rod-based flowerlike nanostructures (**Fig. 2.11**a&b). These emerging rods on the surface of the quasi-spherical flowers also lead to the disconnection of the fused structures. When the temperature was increased to 400℃, the morphology of the NS changed to what seemed like clusters of various morphologies and sizes (**Fig. 2.11**c&d). A further increase in the annealing temperature produced smaller structures with a mixture of spherical and hexagonal morphologies (**Fig. 2.11**e&f).

An extension of time with another 30 minutes under 50 sccm H_2 gas produced agglomerated non-uniform particles (**Fig. 2.12**a&b) whereas an increase in the flowrate to 100 sccm at 300℃ lead to the formation of longer nanorods and some nanoparticles (**Fig. 2.12**c&d)

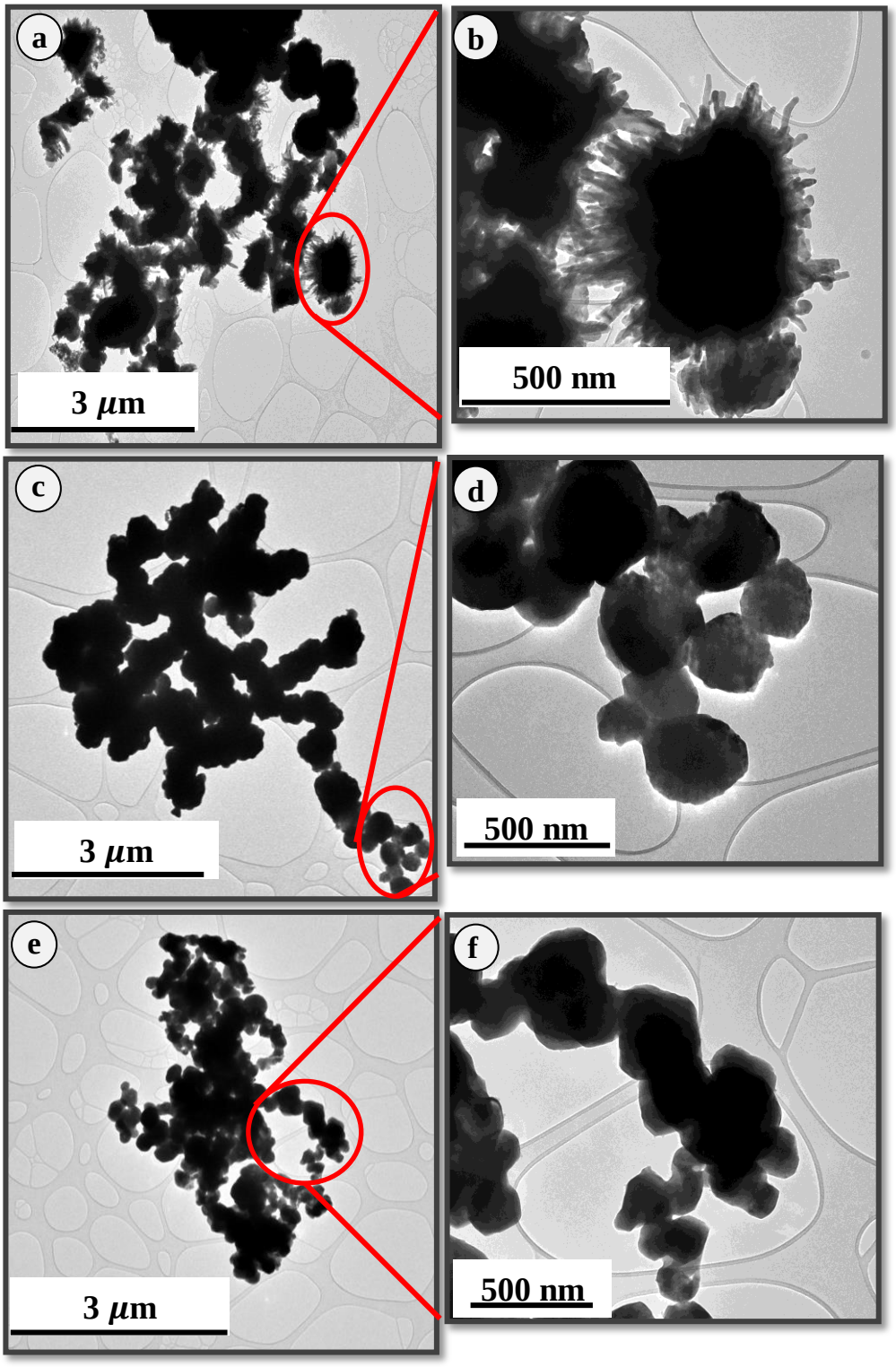

Figure 2. 11. TEM images of NS structures annealed under H_2 gas with a flow rate of 50 sccm for 30 min at (a, b) 300℃, (c, d) 400 ℃ and (e, f) 500 ℃.

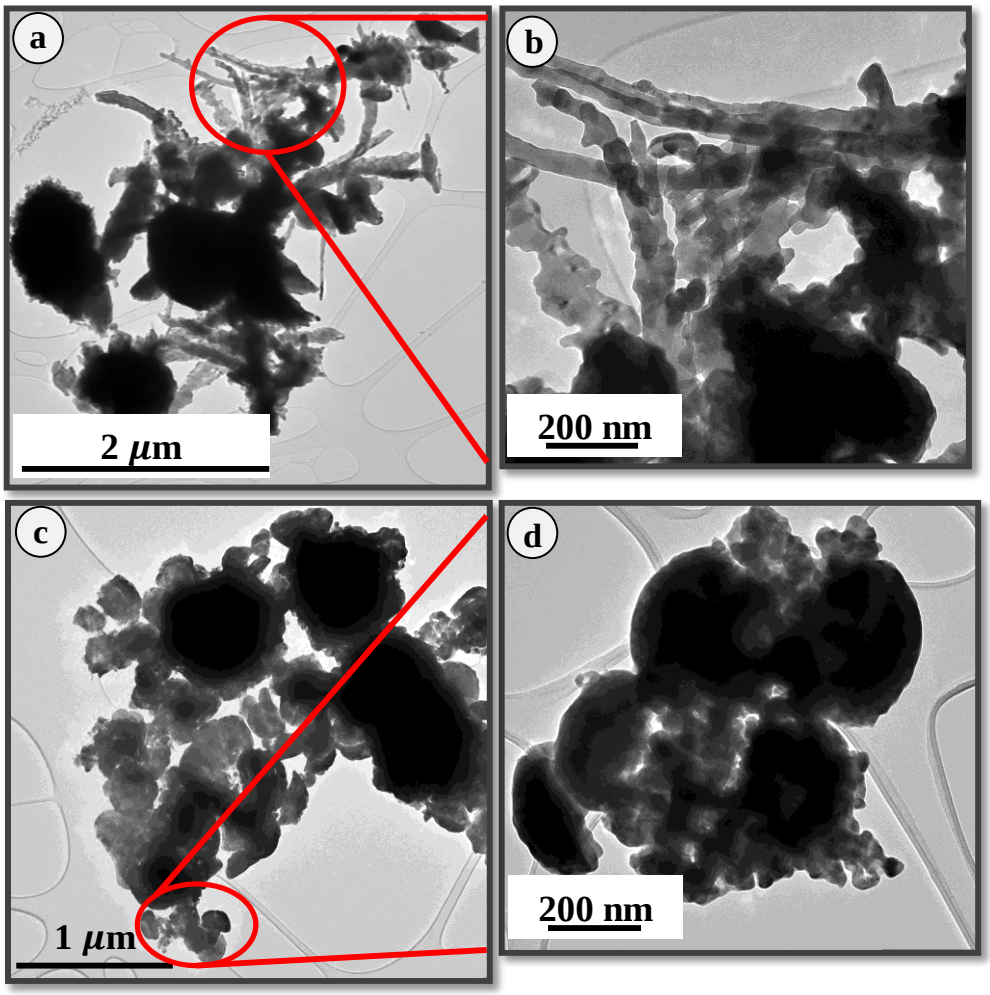

Figure 2. 12. TEM micrographs of NS structures annealed under H_2 gas at 300 ℃: (a, b) with a flow rate of 50 sccm for 1 hour and (c, d) with a flow rate of 100 sccm for 30 min.

2.5. Conclusions

Nickel sulfide nanostructures have been synthesized by a microwave assisted hydrothermal method using water, ethanol, ethylene glycol or a mixture of water/ethanol or water/ethylene glycol as solvents. Water and ethylene glycol and a mixture of these two solvents produced Ni_3S_2 nanostructures with a high phase purity, whereas ethanol or a mixture of water and ethanol produced structures consisting of three different nickel sulfide phases. Varying the volume ratios between water and ethylene glycol, with no change in the other conditions, prepared different types of flower-like nanostructures. Water produced quasi-spherical flower-like structures while ethylene glycol or a mixture of water and ethylene glycol produced layer-based rose-like structures. Nanostructures produced in water had the largest surface area. However, the surface area decreased as ethylene glycol was introduced to the water and started increasing once ethylene glycol was the domineering solvent. The effect of annealing under

hydrogen on the structural and morphological flower-like structures synthesized in water was also studied. Annealing at 300℃ produced Ni_3S_2 where an increase in the temperature produced peaks belonging to other nickel sulphide phases (NiS and Ni_7S_6). An extension of the annealing time decreased the crystallinity of the material. Lastly, when the flowrate was increased peaks also belonging to NiS and Ni_7S_6 appeared.

References

[1] Rao, S.S., Gopi, C.V.V.M, Kim, S.K., Son, M.K., Jeong, M.S., Savariraj, D., Prabakar, K., Kim, H.J., Electrochimica Acta **133** (2014) 174-179.

[2] Luo, M., Liu, Y., Hu, J., Li, J., Liu, J., Richards, R.M., Applied Catalysis B: Environmental **125** (2012) 180-188.

[3] Ren, H., Huang, Z.H., Yang, Z., Tang, S., Kang, F., Lv, R., Journal of Energy Chemistry **26** (2017) 1217-1222.

[4] Wang, Y.K., Wu, G.L., Li, Z.T., Wu, M.B., Advanced Materials Research **1118** (2015) 9-13.

[5] Jiang, N., Tang, Q., Sheng, M., You, B., Jiang, D., Sun, Y., Catalysis Science & Technology **6** (2016) 1077-1084.

[6] Dong, J., Zhang, F.Q., Yang, Y., Zhang, Y.B., He, H., Huang, X., Fan, X., Zhang, X.M., Applied Catalysis B: Environmental **243** (2019) 693-702.

[7] Zheng, X., Han, X., Zhang, Y., Wang, J., Zhong, C., Deng, D., Hu, W., Nanoscale **11** (2019) 5646-5654.

[8] Duan, W., Yan, W., Yan, X., Munakata, H., Jin, Y., Kanamura, K., Journal of Power Sources **293** (2015) 706-711.

[9] Wei, W., Mi, L., Gao, Y., Zheng, Z., Chen, W., Guan, X., Chemistry of Materials **26** (2014) 3418-3426.

[10] Ho, T.A., Bae, C., Nam, H., Kim, E., Lee, S.Y., Park, J.H., Shin, H., ACS Applied Materials & Interfaces **10** (2018) 12807-12815.

[11] Yin, X., Yu, S., Hu, J., Li, H., Lv, Z., Zhou, X., Journal of Alloys and Compounds **791** (2019) 864-873.

[12] Tiwari, J.N., Tiwari, R.N., Kim, K.S., Progress in Materials Science **57** (2012) 724-803.

[13] Li, J., Shen, P.K., Tian Z., International Journal of Hydrogen Energy **42** (2017) 7136-7142.

[14] Li, Y., Shi, M., Wang, L., Wang, M., Li, J., Cui, H., Advanced Powder Technology **29** (2018) 1092-1098.

[15] Li, J-J. Hu, Y-X., Liu, M-C., Kong, L., Journal of Alloys and Compounds **656** (2016) 575-583.

[16] Wang, Y.L., Wei, X.Q., li, M.B., Hou, P.Y., Xu, X.J., Applied Surface Science **436** (2018) 42-49.

[17] Li, J., Wang, S., Xiao, T., Tan X., Xiang, P., Jiang, L., Deng, C., Li, W., Li, M., Applied Surface Science **420** (2017) 919-926.

[18] Mi, L., Ding, Q., Chen, W., Zheng, Z., Hou, H., Liu, C., Shen, C., RSC Advances **2** (2012) 6817-6823.

[19] Kim, S., Lee, S.H., Lee, Y., Biosensors and Bioelectronics **85** (2015) 587-595.

[20] Mirzaei, A., Kim, J-H., Kim, H.W., Sim, S.S., Sensors and Actuators B **258** (2018) 270-294.

[21] Hu, H., Deng, C., Zhang, K., Yin, P, Micro & Nano Letters **7** (2012) 464-466.

[22] Mehta, S.K., Khushboo, Umar, A., Talanta **85** (2011) 2411-2416.

[23] Pang, H., Wei, C., Li, X., Li, G., Ma, Y., Li, S., Chen, J., Zhang, J., Scientific Reports **4** (2014) 3577.

[24] Liu, H., Su, Y., Chen, P., Wang, Y., Journal of Molecular Catalysis A: Chemical **378** (2013) 285-292.

[25] Krishnapriya, R., Praneetha, S., Murugan, A.V., CrystEngComm **17** (2015) 8353-8367.

[26] Tang, S., Zheng, Z., Vongehr, S., Meng, X., Journal of Nanoparticles Resolution **13** (2011) 7085-7094.

[27] Khoza, P.B., Moloto, M.J., Sikhwivhilu, L.M., Journal of Nanotechnology (2012) 195106.

[28] Salavati-Niasari, M., Banaiean-Monfared, G., Emadi, H., Enhessari, M., Competes Rendus Chimie **16** (2013) 929-936.

[29] Zhao, Y., Liao, X.H., Hong, J.M., Zhu, J.J., Materials Chemistry and Physics **87** (2004) 149-153.

[30] Zhu, Y-J., Chen, F., Chemical Reviews **114** (2014) 6462-6555.

[31] Wojnarowicz, J., Opalinska, A., Chudoba, T., Gierlotka, S., Mukhovskyi, R., Pietrzyowska, E., Sobczak, K., Lojkowski, W., Journal of Nanomaterials, (2016) 2789871.

[32] Shanmugam, N., Cholan, S., Kannadasan, N., Sathishkumar, K., Viruthagiri, G., Journal of Nanomaterials **2013** (2013) 351798.

[33] Mhlongo, G.M., Motaung, D.E., Nkosi, S.S., Swart, H.C., Malgas, G.F., Hillie, K.T., Mwakikunga, B.W., Applied Surface Science **293** (2014) 62-70.

[34] Ungula, J., Dejene, B.F., Swart, H.C., Results in Physics **7** (2017) 2022-2027.

[35] Tshabalala, Z.P., Shingange, K., Dhonge, B.P., Ntwaeaborwa, O.M., Mhlongo, G.H., Motaung, D.E., Sensors and Actuators **238** (2017) 402-419.

[36] Baleyeva, O.O., Azizov, A.A., Muradov, M.B., Maharramov, A.M., Eyvazova, G.M., Gasimov, R.J., Dadashov, Z.X., Materials Science in Semiconducting Processing **64** (2017) 130-136.

[37] Mahmood, N., Zhang, C., Hou, Y., Small **9** (2013) 1321-1328.

[38] Linganiso. E.C., PhD Thesis, University of the Witwatersrand, Johannesburg (2014).

[39] Marcano, D.C., Kosynkin, D.V., Berlin, J.M., Sinitskii, A., Sun, Z., Slesarev, A., Alemany, L.B., Lu, W., Tour, J.M., ACS Nano **4** (2010) 4806-4814.

[40] Zhang, C., Wang, S., Tang, S., Wang, S., Li, Y., Du, Y., Applied Surface Science **458** (2018) 656-664.

[41] Chou, S.W., Li, J.Y., Journal of the Electrochemical Society **160** (2013) D178-D182.

[42] Davies, D.A., Silver, J., Vecht, A., Marsh, P.J., Rose, J.A., Journal of The Electrochemical Society **148** (2001) H143-H148.

[43] Makarov, S.V., Horváth, A.K., Silaghi-Dumitrescu, R., Gao, Q., Chemistry A European Journal **20** (2014) 14164-14176.

[44] He, H., Chen, A., Lv, H., Dong, H., Chang, M., Li, C., Journal of Alloys and Compounds **574** (2013) 217-220.

[45] García-Valenzuela, J.A., Comments on Inorganic Chemistry **37** (2017) 99-115.

[46] Pimental, A., Rodrigues, J., Duarte, P., Nunes, D., Costa, F.M., Monteiro, T., Martins, R., Fortunato, E., Journal of Materials Science **50** (2015) 5777-5787.

[47] Wang, X., Hu, J., Su, Y., Hao, J., Liu, F., Han, S., An, J., Lian, J., Chemistry A European Journal **23** (2017) 4128-4136.

[48] Muthu, N.S., Gopalan, M., Applied Surface Science **480** (2019) 186-198.

[49] Kristl, M., Dojer, B., Gyergyek, S., Kristl, J., Heliyon **3** (2017) e00273.

[50] Yin, P.F., Zhou, C., Han, X.Y., Zhang, Z.R., Xia, C.H, Sun, L.L., Journal of Alloys and Compounds **620** (2015) 42-47.

[51] San, Y., Zhao, G., Wang, G., Shen, Y., Meng, D., Zhang, Y., Meng, F., RSC Advances **7** (2017) 3540-3549.

[52] Xu, L., Ding, Y.S., Chen, C.H., Zhao, L., Rimkus, C., Joesten, R., Suib, S.L., Chemistry of Materials **20** (2008) 308-316.

[53] Lim, J., Sim, K., Lee, J.K., CrystEngComm **18** (2016) 2155-2162.

[54] https://www.flowerglossary.com/orange-flowers/ (Accessed 15 Dec 2019).

[55] Bavykin, D.V., Parmon, V.N., Lapkin, A.A., Walsh, F.C., Journal of Materials Chemistry **14** (2004) 3370-337.

[56] Zhang, Y., Li, C., Liu, L., Wang, K., Zhu, Y., Ben, J., Wu, J., Journal of Superconductivity and Novel Magnetism **32** (2019) 757-762.

[57] Feng, N., Hu, D., Wang, P., Sun, X., Li, X., He, D., Physical Chemistry Chemical Physics **15** (2013) 9924-9930.

[58] Wang, J-H., Cheng, Z., Brèdas, J-L., Liu, M., The Journal of Chemical Physics **127** (2007) 214705.

[59] Cheng, Z., Abernathy, H., Liu, M., The Journal of Chemical Physics C **111** (2017) 17997-18000.

[60] Zheng, J.H., Zhang, R.M., Wang, X.G., Materials Letters **228** (2018) 191-194.

[61] Linganiso, E.C., Mwakikunga, B.W., Mhlanga, S.D., Coville, N.J., Sone, B.T., Maaza, M., 2012 SENSORS IEEE, Taipei (2012) 1-4.

[62] Jenkins, R., Snyder, R., *Introduction to X-Ray Powder Diffractometry*; Chemical Analysis, John Wiley & Sons: New York **138** (1996) 91-95.

[63] Ou, X., Luo, Z., RSC Advances **6** (2016) 10280-10284.

[64] Zak, A.K., Abrishami, M.E., Majid, W.H.A., Yousefi, R., Hosseini, S.M., Ceramics International **37** (2011) 393-398.

Chapter 3: Synthesis of reduced graphene oxide from graphite powder

3.1. Introduction

A paper published by Nobel Laureates, Konstantin Novoselov and Andre Geim, on how they experimentally attained graphene from graphite has accelerated graphene research so much so that is now called a 'wonder material' and 'celebrity' in the field of material science [1-4]. The many unique advantages presented by this one atom thick 2D material allows it to be applied in a wide range of fields, from energy storage devices [5] to water purification [6] and catalysis [7]. Graphene is a planar sheet of sp^2 hybridized carbon atoms that are tightly packed to form a 2D honeycomb crystal structure [1-8].

Numerous methods for the synthesis of graphene from non-graphitic and graphitic sources have been investigated [8]. Chemical vapour deposition growth on copper [5, 8-9] and epitaxial growth on silicon carbide [10] use non-graphitic sources to produce graphene. These methods can produce high quality graphene with high electrical conductivity. However, they are not appropriate for large-scale synthesis needed in the industry. Micromechanical cleavage [1, 11] and chemical oxidation followed by reduction [4, 12] of graphite are also well-documented methods for obtaining good quality graphene. The most popular and probably the most cost effective method for attaining graphene on a large scale is reduction of graphene oxide sheets exfoliated from graphite oxide [4, 12-13].

Graphene oxide (GO) is a single or few layers of graphite with incorporated oxygen functional groups: epoxy and alcohol groups on the basal planes and carboxyl and ketone groups at the edges [14]. These oxygen functionalities can be removed or lessened by various reduction processes [4, 12, 15-16]. The degree of reduction on GO significantly influences the thermal, electrical and physical properties of the subsequent reduced graphene oxide (rGO) product. This can be easily tuned by altering the reaction conditions of the particular reduction strategy used [12, 16]. Techniques such as high temperature refluxing [17], hydrothermal [18], thermal heating [4, 19], photochemical [20] and microwave methods [13, 21-30] have all been studied for the reduction of GO.

A reducing agent is often used in wet chemical methods and it is well known that the electrical properties and the carbon to oxygen ratios of rGO are dependent on the nature of the reducing

agent. Hydrazine has proven to be the best reducing agent for graphene oxide producing reduced graphene oxide with the lowest oxygen content and better electrical conductivity compared to other reducing agents ($NaBH_4$, hydrioc acid etc.) [16, 31-33]. Hydrazine is however toxic to human beings and the environment [12]. Researchers have explored using reduced amounts of hydrazine by employing a combination of methods [4] and using environmentally friendlier reducing agents such as enzymes, bio-organisms, sugars and other organic compounds [12, 34]. The application of ascorbic acid (vitamin C) as a reducing agent of GO was firstly reported by Zhang and colleagues [34]. Their work initiated a huge interest in using ascorbic acid for GO reduction since the rGO produced with this reducing agent exhibited properties (electrical conductivity and C/O ratio) closest to the one synthesized using hydrazine.

Other methods such as laser [35], ultra-violet [36], solar [37] and microwave radiation [13, 21-30] have been considered in the quest of finding greener alternatives for the reduction of GO to rGO. Microwave synthesis reactions are known to occur at higher reaction rates due to selective heating [38]. The consideration of using microwave technology as a viable alternative reduction strategy for GO has recently gained momentum because of the above-mentioned advantages [39]. Additionally, the interaction of microwave irradiation with carbon materials is different because heating is mainly caused by the π-π electrons [40]. This peculiar heating mechanism is great for material processing and functioning.

The effects of microwave reaction time and power level on the structural and electrical properties of rGO have been investigated [24, 27]. Agusu et al. observed an increase in the interlayer spacing of the reduced graphene oxide sheets as the microwave power level was increased from 240 to 550 W when the reduction reaction was ran for 20 minutes in a domestic microwave oven using Zn as a reducing agent [27]. However, when the reaction time was increased to 40 minutes, the interlayer spacing showed a decrease when the power was higher than 400 W. Additionally, the stacking thickness decreased with an increase in power during the 20 minute reactions. The electrical conductivity reached a maximum at an operating power of 400 W. Microwave-assisted hydrazine reduction of GO to rGO has been reported by Elazab [30] and Li [24]. Both reporters applied a relatively low power (250 and 300 W) for the production of rGO in 10 minutes achieving an 8.1 and 5.28 C/O ratio, respectively.

This chapter reports on the synthesis of reduced graphene oxide from graphite powder. The graphite powder was oxidized using a well-known method to obtain graphene oxide, thereafter

the obtained graphene oxide reduced using a microwave-assisted method and a thermal heating technique. Reduction via microwave technology investigated the effect of using different reducing agents and thermal reduction was done in air environment only for comparison.

3.2. Experimental procedure

Graphite powder (<20 μm), potassium permanganate ($KMnO_4$, 99%), sulfuric acid (H_2SO_4, 98%), phosphoric acid (H_3PO_4, 85%), hydrogen peroxide (H_2O_2, 30%), hydrazine hydrate (NH_2H_4, 50-60%), L-ascorbic acid ($C_6H_8O_6$, 99%) and barium chloride dihydrate ($BaCl_2 \cdot 2H_2O$, 96%) were purchased from Sigma Aldrich, South Africa and used as received. A 10% hydrochloric acid solution was prepared by diluting a purchased HCl (36%, Sigma Aldrich, South Africa) solution with distilled water.

3.2.1. Preparation of graphene oxide

GO was prepared from graphite powder using the Improved Hummers' method [41]. In a typical synthesis, 3 g of graphite powder and 18 g of $KMnO_4$ was slowly added to a cold (0℃) 400 mL acid mixture containing 360 mL of H_2SO_4 and 40 ml of H_3PO_4 while ensuring that the temperature did not exceed 20℃. The mixture was then stirred at 50℃ for 12 hours and the oxidation terminated by adding 3 mL of H_2O_2 and 400 mL of ice-cold distilled water. The brown gel was centrifuge washed at 15 000 rpm with 10% HCl until all sulphate ions were removed (tested using $BaCl_2 \cdot 2H_2O$) followed with distilled water until a pH of ~7. The suspension was ultra-sonicated for an hour and vacuum freeze-dried at ~ -80℃ for a week.

3.2.2. Reduction of graphene oxide

A GO suspension was produced by dispersing 200 mg of GO in 200 mL of distilled water by ultra-sonication. A certain amount of reducing agent (hydrazine hydrate (3 mL) and ascorbic acid (1 g)) was added to the suspension which was then stirred for a few minutes to obtain homogeneity. The mixture was transferred into the Teflon-lined microwave reaction vessels and placed into a microwave reactor (Anton Paar Multiwave 3000) which was operated at 600 W for 10 minutes followed by fan cooling until room temperature was reached. The black precipitates were washed with water and ethanol and later dried overnight at 100℃. A control experiment was conducted where the GO suspension (without addition of any reducing agent) was exposed to microwave irradiation under the same conditions.

In an attempt to compare the degree of defects in microwave-reduced rGO with conventionally prepared rGO, GO powders were exposed to thermal reduction in air for 30 minutes. In brief, 200 mg of GO was weighed in a quartz boat and placed in a horizontal tube furnace. The furnace was heated to 300℃ at a ramping rate of 5 ℃/min, kept at 300℃ for 30 minutes and cooled to room temperature.

The products were labelled as mGH, mGA and mGC for the samples prepared by microwave reduction using hydrazine, ascorbic acid, and the control, respectively. The thermally reduced product was identified as tGA for reduction in air.

3.3. Characterization

The graphite and as-synthesized materials were characterized using the various techniques as described in **Chapter 2.3**.

3.4. Results and discussion

The formation of reduced graphene oxide from graphite powder is schematically shown in **Scheme 3.1**. The oxidation process leads to a population of different oxygen moieties on the graphite sheets. The concentration of these moieties is greatly reduced after the reduction of graphene oxide.

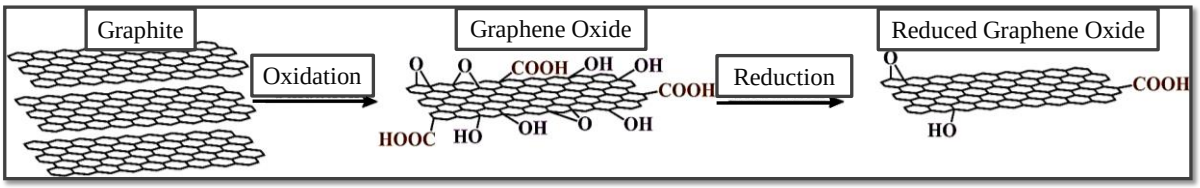

Scheme 3. 1. Formation mechanism of rGO from graphite powder [15].

3.4.1. Phase analysis

The transformations that occurred in the crystal structure of graphite during the oxidation-reduction process were firstly confirmed using X-ray diffraction (XRD). Crystallographic parameters for graphite, GO and all the rGO samples were determined using the XRD patterns (**Fig. 3.1**). The interlayer spacing (d_{002}), crystal stack height (L_c), in-plane crystal sizes (L_a) and the number of graphene layers in the crystal (N_c) were all estimated using the equations below [12]:

$$d_{002} = \frac{\lambda}{2 \sin \theta_1} \qquad \textbf{(3.1)}$$

$$L_c = \frac{k_1 \lambda}{FWHM \cos \theta_1} \quad (\mathbf{3.2})$$

$$L_a = \frac{k_2 \lambda}{FWHM \cos \theta_2} \quad (\mathbf{3.3})$$

$$N_c = \frac{L_c}{d_{002}} \quad (\mathbf{3.4})$$

Where, λ is the radiation wavelength, θ_1 the diffraction peak position for the (002) or (001) diffraction plane, θ_2 the peak position for the (100) plane, k_1 a form factor usually applied as 0.9, k_2 the Warren Form Factor constant applied as 1.84, and FWHM the width at half height for the corresponding plane.

The XRD pattern in **Fig. 3.1**a confirmed the formation of GO from graphite powder. Graphite (inset) exhibits peaks at 2θ = 26.4°, 42.4°, 44.4° and 54.4° corresponding to the (002), (100), (101) and (004) planes of carbon, respectively (PDF 00-008-0415). The intense crystalline (002) plane of graphite was consistent with an interlayer spacing of 0.34 nm (**Table 3.1**). In GO, the (002) peak disappeared and a new peak emerged at ~ 2θ = 10.9° assigned to the (001) plane of carbon that corresponded to an interlayer spacing of 0.81 nm. This increase in the interlayer spacing indicated an expansion of graphite sheets due to the incorporation of oxygen functional groups as well as water molecules in the interlayer galleries of hydrophilic GO [41]. This distinct and sharp peak suggest that ordered structure along the c-axis was preserved [42]. Reduction caused a disappearance of the latter and a re-emergence of the (002) plane assigned to graphitic carbon at 2θ = 24-25°in the rGO samples (**Fig. 3.1**b). Consequently, the interlayer spacing decreased to 0.35-0.37 nm due to the removal of the oxygen functional groups and water molecules, and a restacking coupled with overlapping of the rGO sheets. The wider (002) peak in the reduced samples could be indicative of their poor ordering along the stacking direction and that they were mostly comprised of freestanding graphene sheets [43]. Furthermore, the (100) plane in tGA was not as prominent as in the microwave reduced samples. The observed decrease in the crystal domains (L_a and L_c) after oxidation and reduction inferred an increased structural disorder in the GO and rGO samples [12]. The number of layers in the crystal structure (N_c) of graphite decreased tremendously after oxidation because of the separation caused by oxidation and exfoliation, and the amorphous nature of rGO.

When comparing the crystallographic parameters of the microwave reduce samples with each other, the interlayer spacing between the rGO sheets (d_{002}) were all the same suggesting that

the degree of oxygen functional group removal between the sheets was similar in all the samples. Consequently, the stacking height (L_c) of these samples was also the same. The number of crystal layers was the lowest in the control sample (mGC) and similar to the GO. Lastly, the in-plane crystal size was the highest in mGH and comparable to the thermally reduced sample (tGA).

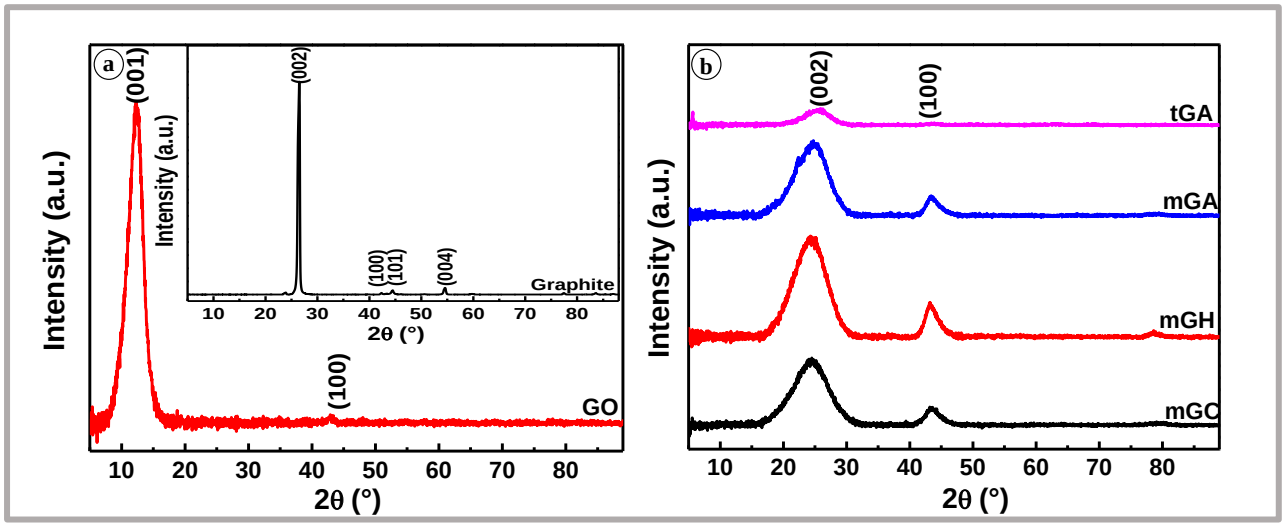

Figure 3. 1. XRD pattern for GO (inset: graphite) (a), and rGO (b).

Table 3. 1. Summary of XRD data for all the samples.

Sample	**(002) or (001) Plane (2 *θ* (°))**	**L_c (nm)**	**d_{002} (nm)**	**N_c**	**(100) Plane (2 *θ* (°))**	**L_a (nm)**
Graphite	26.4	18.6	0.34	55	42.4	30.8
GO	12.2	2.6	0.81	3	42.9	16.7
mGC	24.3	1.2	0.37	3	43.6	6.0
mGH	24.2	1.3	0.37	4	43.5	7.0
mGA	24.4	1.3	0.37	4	43.7	6.7

tGA	25.3	1.7	0.35	5	43.7	8.5

3.4.2. Morphology analysis

The morphological properties of the materials were evaluated using transmission electron microscopy (TEM). Graphite has a crystalline platelet-like morphology with well-defined sheets (**Fig. 3.2**a). The GO and rGO displayed sheets that were a few micrometres in size (**Fig. 3.2**b-f). The crumpled, wrinkled few layered sheets in GO indicated that exfoliation produced 2D sheets [37]. The wrinkles were attributed to the structural defects or functional groups that changed the electronic structure of the carbon atoms from sp^2 to sp^3 [44]. The rGO sheets appeared to be denser due to re-stacking caused by the weak van der Waals bonds between the sheets [37]. The wrinkling and folding was still prominent in the rGO samples due to the tension in the carbon-to-carbon bonds [15]. mGC (**Fig.3.2**c) seemed to have smaller sheets with denser, more compact regions at the edges. The high magnification TEM micrographs of mGH (**Fig. 3.2**g&h) further illustrated the crumpling and wrinkling present in the rGO sample.

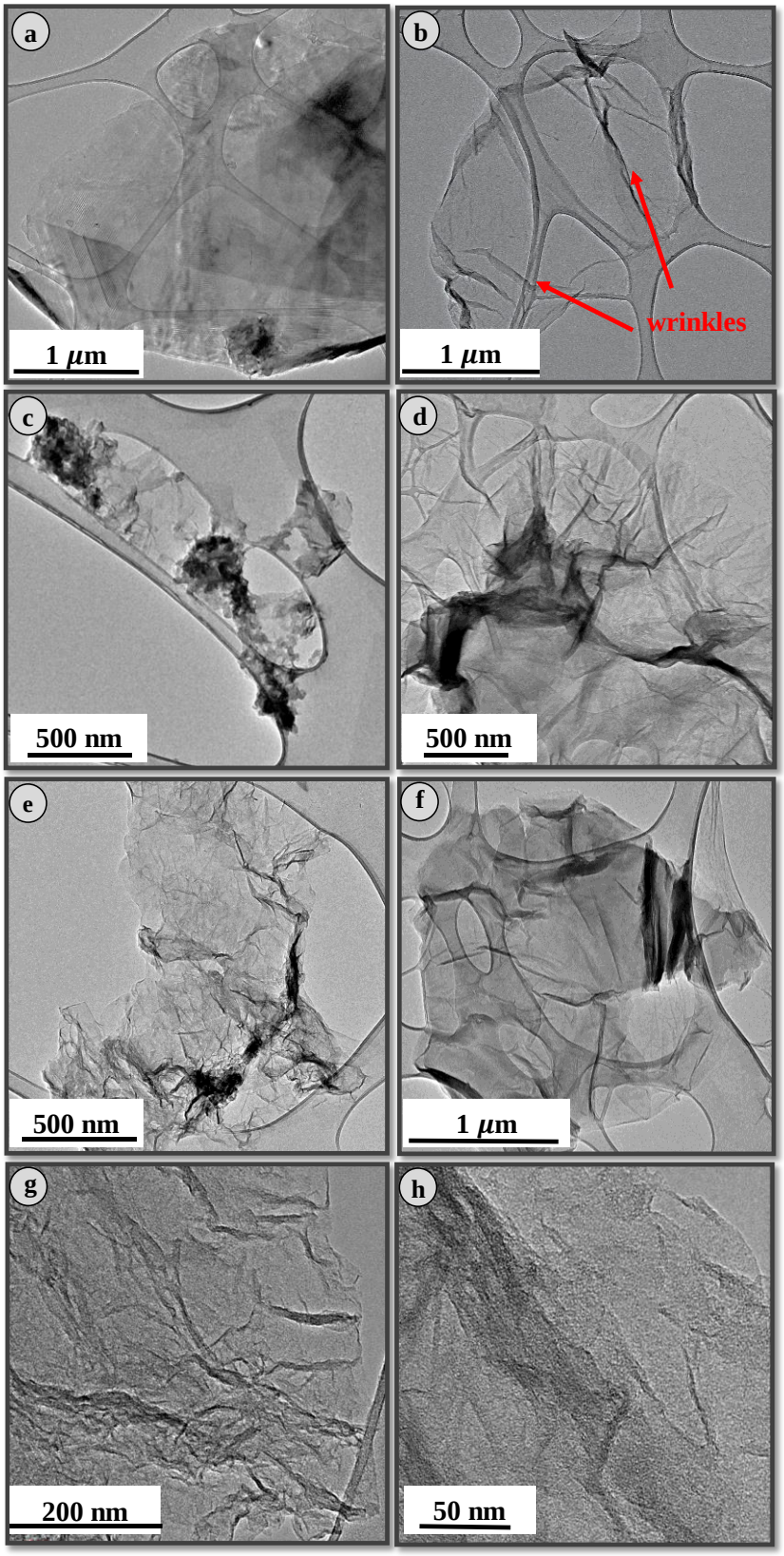

Figure 3. 2. TEM micrographs of graphite (a), GO (b), mGC (c), mGH (d), mGA (e), tGA (f), and high magnification TEM image of mGH (g and h).

3.4.3. Laser Raman spectroscopic analysis

The significant structural changes occurring during the oxidation-reduction process were further reflected in the Raman spectra of graphite, GO and the rGO samples. The Raman spectrum for graphite (**Fig. 3.3**a) consisted of the three characteristic carbon peaks, i.e. the D, G and 2D band [45, 46]. The D band around 1352.2 cm $^{-1}$ could be ascribed to the breathing modes of the sp^2 and sp^3 carbon atoms in the rings and represents the imperfections or disorders in the carbon structure. The extremely low area of this band suggest that graphite contains a very small concentration of defects in its carbon structure [15]. The G band at 1579.1 cm^{-1} was due to the bond stretching of the sp^2 carbon atoms in both the chains and rings. The 2D band situated at 2715.7 cm^{-1} was due to the second-order two-phonon process. No D^* band (usually situated at ~ 1620 cm^{-1}) was observed in graphite and the synthesized GO and rGO materials indicating the high quality of graphene films [46]. An increase in the area and intensity of the D band occurred after oxidation due to the transformation of some in plane sp^2 carbons into disordered sp^3 carbons when oxygen functionalities were introduced. The blue shift of the G band could possibly also be explained by the reduction in sp^2 domains. The 2D band was diminished in the GO because of the chemical defects induced by the functional groups between the graphitic layers [47]. The shift in position of the G band continued after the reduction process due to the strain associated with the removal of oxygen functional groups during reduction of GO.

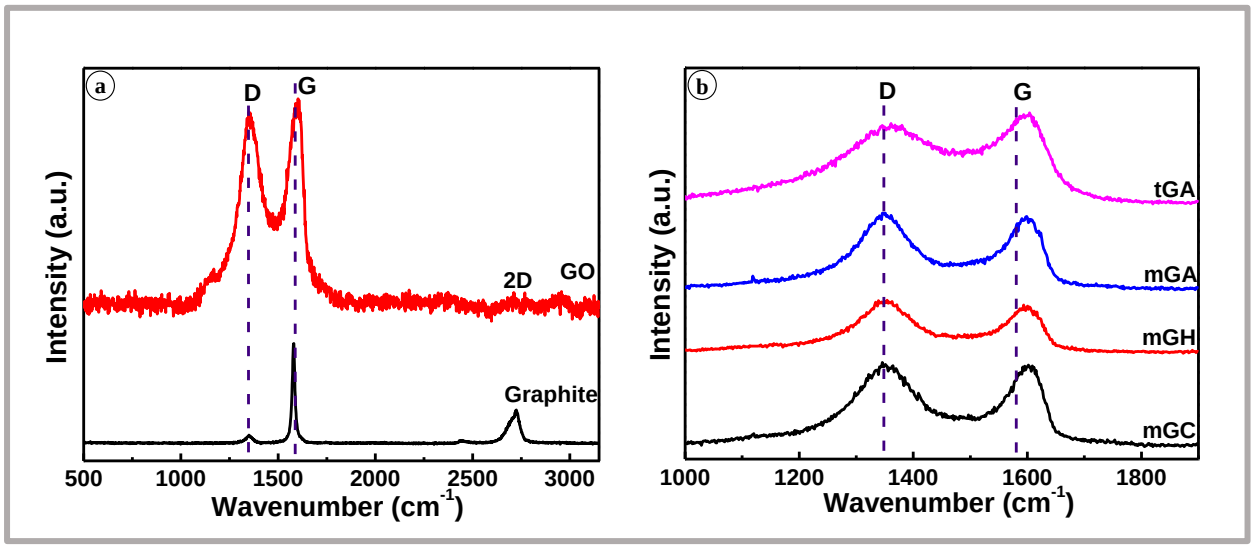

Figure 3. 3. Raman spectra of GO and graphite (a), and rGO samples (b).

The I_D/I_G ratio (the area under each peak was applied instead of intensity) gives an estimation of the number of structural defects and the size of the in-plane sp^2 domains present in the material (**Table 3.2**) [43]. An increase in the I_D/I_G ratio was observed after oxidation of graphite, which was consistent with literature [4, 15, 18, 43]. This value increased further during reduction where the edges of the sheets increased when the sp^2 domains were torn apart by the removal of the oxygen groups [4, 37]. Some carbon atoms were also removed resulting in pores and defects in the graphitic lattice [31, 37]. mGC has an I_D/I_G ratio of 2.13, which was 0.1 less than that of mGH proposing that reduction by microwave irradiation without a reducing agent was effective in inducing more defects in rGO. As anticipated, the concentration of defects were found to be lower in mGA because of the lower reducing ability of ascorbic acid which was even lower than mGC inferring that the ascorbic acid could hinder the defect inducing ability of microwave irradiation. The thermally reduced sample had a higher defect density. These defect densities of the microwave-reduced samples and tGA were comparable considering the fact that microwave reduction occurred in a short period of time and lower temperatures when compared to thermal reduction.

Table 3. 2. Summarized Raman data for graphite, GO and rGO samples.

	D Band		**G Band**		**2D Band Centre (cm^{-1})**	**I_D/I_G**
	Centre (cm^{-1})	**FWHM (cm^{-1})**	**Centre (cm^{-1})**	**FWHM (cm^{-1})**		
Graphite	1352.2	30.3	1579.1	16.4	2715.7	0.17
GO	1358.6	143.1	1590.1	82.3	-	1.63
mGC	1351.8	138.6	1596.4	65.5	-	2.13
mGH	1349.5	126.5	1596.6	62.1	-	2.23

mGA	1349.7	125.7	1593.3	69.3	-	1.87
tGA	1364.1	221.8	1590.8	84.4	-	2.48

3.4.4. Functional group analysis

FTIR spectroscopic measurements performed on the materials was used to elucidate the functional groups present in all the samples. The spectra for graphite and rGO samples were similar (**Fig. 3.4**). GO showed a peak between 3450 and 3666 cm^{-1} corresponding to an overlap of the –OH stretching mode of the incorporated alcoholic hydroxyl and –COOH groups across the GO sheet [18]. The strong hydrogen bonds between adsorbed water molecules and the carboxylic acid groups could also be represented by this peak [48]. The –OH bending mode of adsorbed water was also present at 1400 cm^{-1} [12, 18]. These peaks were weakened after reduction with tGA showing the weakest intensity. The C=O stretching vibration of the carboxyl and carbonyl conjugated groups (ester, aldehyde) was found at 1623-1734 cm^{-1} [12, 18, 49]. After reduction, these peaks were still present, however at a very low intensity for mGA and almost completely diminished in mGH. The epoxy or peroxide groups, alkoxy and epoxy groups were responsible for the C-O-C and C-O stretching at 980 cm^{-1}, 1054 cm^{-1} and 1226 cm^{-1}, respectively [18, 50]. The skeletal alkene group (C=C) stretching modes were present in the rGO samples at ~1000 cm^{-1} (in plane bending of C=C) and ~1540 cm^{-1} (aromatic C=C stretching). The fore mentioned indicate a loss of a majority of oxygen functional groups and the recreation of the sp^2 domains after reduction [49]. The symmetric and asymmetric stretching vibrations of CH_2 were present at 2892 cm^{-1} and 2960 cm^{-1} [51]. mGH and mGA exhibited a decrease in the intensity of most oxygen groups when compared to mGC and tGA especially the C=O specie. CO_2 and moisture-related peaks were also observed around 2300 cm^{-1}.

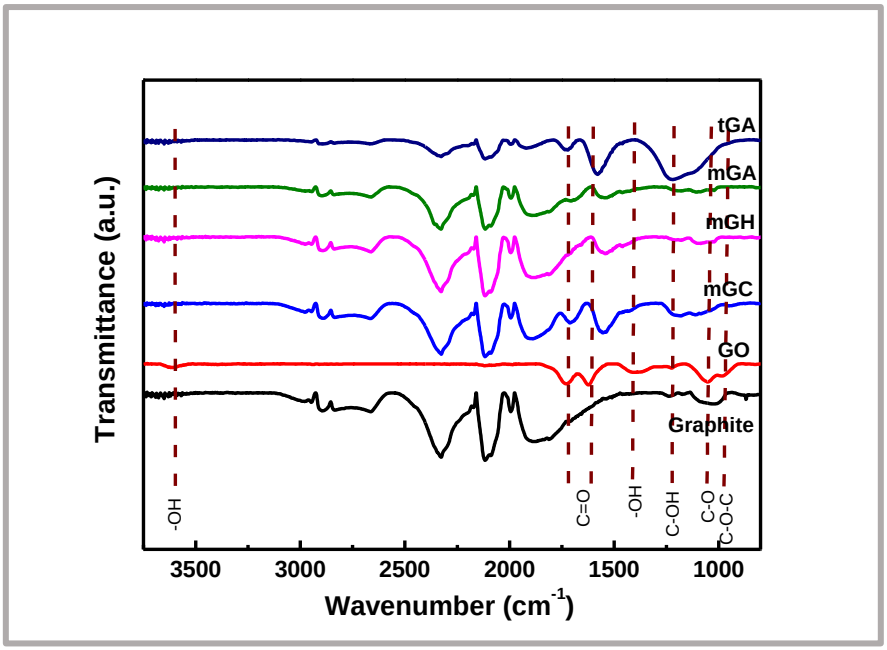

Figure 3. 4. FTIR spectroscopic results for graphite, GO and all rGO samples.

3.4.5. BET surface area analysis

The specific surface area of graphite, GO and mGH have been measured using BET adsorption of N_2 gas. The surface area of graphite increased from 6.9 m^2/g to 80.4 m^2/g upon oxidation (**Table 3.3**). There was a further increase after reduction to 815.2 m^2/g, which was lower than the theoretical surface area of graphene (2600 m^2/g) due to the agglomeration of the sheets that resulted in overlapping and coalescing with many exposed surfaces [1, 31]. This obtained value was however higher than rGO obtained using other methods [49] and comparable to rGO obtained using microwave methods [52]. Initially, during the production of GO, chemical oxidation followed by exfoliation via sonication caused an increase in surface area. mGH has an almost 10 times higher surface area than GO. The latter could be ascribed to the ability that microwaves have of producing large heat in the layers of the graphene oxide resulting in exfoliation of the sheets [39]. The pore volume of mGH was much larger than that of both graphite and GO because of the joint influence of sonication during the dispersion of GO and microwave effects [39]. The pore volume of GO was lower than that of graphite possibly due to the pressure applied during the freeze-drying process. The N_2 adsorption-desorption isotherms for all three material are illustrated in **Fig 3.5**. Graphite exhibit a type III isotherm with a H3 hysteresis loop whereas GO and rGO have a type IV isotherm according to IUPAC classifications. Both have a H3 hysteris loop between relative pressures of 0.4-1.0 indicating the presence of mesopores in which irreversible capillary condensation occurs. The pore

diameter distribution for the three samples are illustrated as insets in their respective isotherms (**Fig. 3.5**). A broad pore diameter distribution with a sharp peak centred at 137.5 nm was observed for graphite, and narrow peaks at 3.4 nm and 3.5 nm for GO and rGO, respectively. From the curves, we could conclude that graphite has micropores within the structure and that the pore distribution between 90 and 160 nm is due to the spacing in between the bulk graphite.

Table 3. 3. Surface area of graphite, GO and mGH.

Sample	**BET surface area (m^2/g)**	**Pore volume (cm^3/g)**
Graphite	6.9	0.15
GO	80.4	0.02
mGH	815.6	0.61

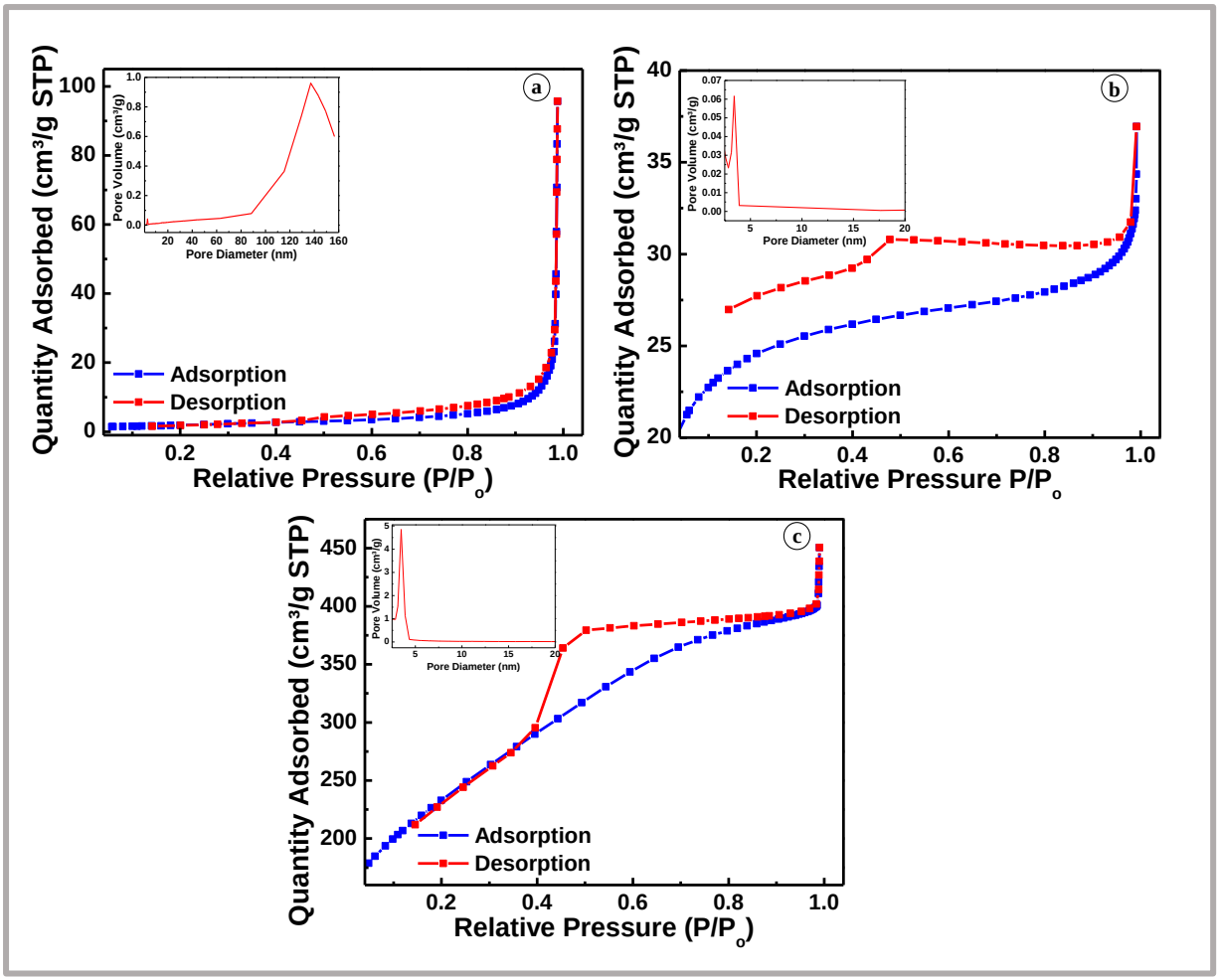

Figure 3. 5. N_2 adsorption-desorption isotherms and their respective pore diameter distribution curves (inset) for graphite (a), GO (b) and mGH (c).

3.4.6. Elemental analysis

X-ray photoelectron spectroscopy (XPS) was used to evaluate the surface composition and the carbon hybridization of GO and rGO. The XPS survey spectra of both GO and mGH is illustrated in **Fig. 3.6** and the elemental composition of both summarized in **Table 3.4**. The carbon to oxygen content in GO is reported as 1.99 and 7.8 in mGH. The latter was similar to a C/O to ratio obtained by microwave-assisted hydrazine reduction by Elazab [30]. Approximately 6.8% of nitrogen was present in rGO arising from the nitrogen in hydrazine [31]. Very low percentages of impurities were present in both GO (S 2p and Cl 2p) and rGO (F 1s and Mg 1s).

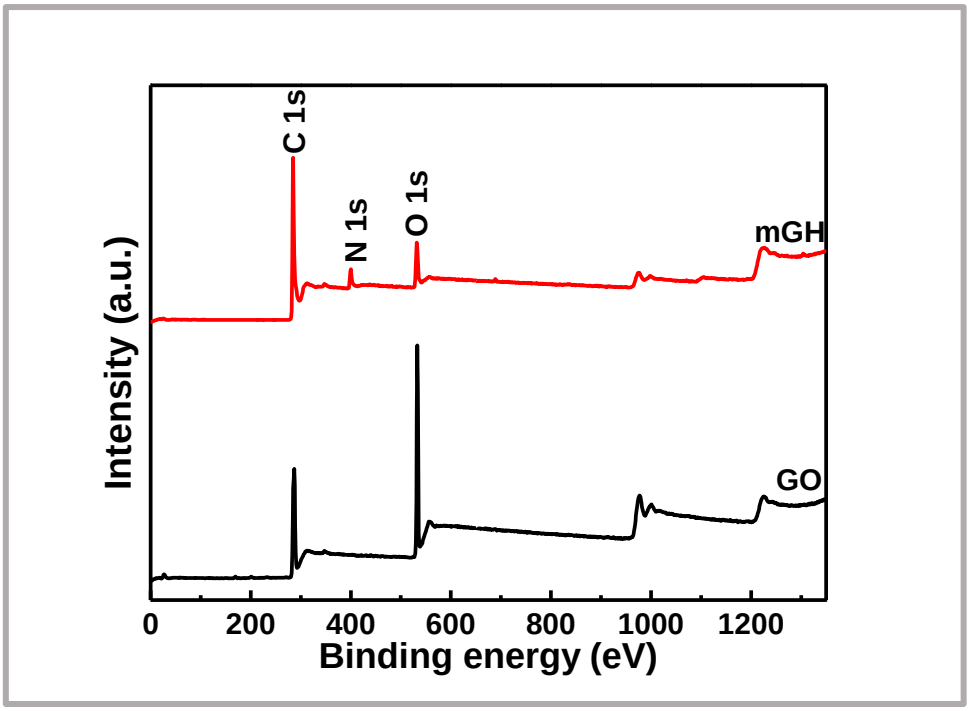

Figure 3. 6. XPS survey spectra of GO and mGH.

Table 3. 4. Atomic compositions of GO and mGH

	C (at %)	O (at %)	N (at %)	S (at %)	Cl (at %)	F (at %)	Mg (at %)
GO	66.1	33.2	-	0.4	0.2	-	-
mGH	82.2	10.6	6.8	-	-	0.3	0.2

The high-resolution XPS C 1s and O 1s core level spectra of the GO and mGH were de-convoluted to study the oxygen speciation in both samples. The bonding states of the C 1s core-level spectra for GO (**Fig. 3.7**a) and rGO (**Fig. 3.7**c) were both de-convoluted into four peaks. The first major peak (~284 eV) in both spectra could be assigned to the sp^2 C=C and sp^3 C-C bonds [53]. This peak became narrower and sharper after reduction indicating that the mGH structure was more regular than the GO structure. The C-O bond of the epoxy and hydroxyl groups was located at 287.2 eV in GO and at 286.1 eV in mGH. This peak shifted and decreased after reduction because of the elimination of hydroxyl groups at the basal planes by hydrazine reduction. The carbonyl group was represented by the C=O at a binding energy of 287.4 eV

for GO. In mGH, the C-N group at 285.2 eV substituted the latter [53]. Finally, the last peak corresponded to the O-C=O (289.2 eV for GO and 287.7 eV for mGH) bond of the carboxylic groups. This was almost completely weakened after reduction. The shift noted in the peak positions after reduction could be ascribed to the introduction of nitrogen in the structure [53, 54].

The O 1s spectra of GO (**Fig. 3.7**b) consisted of two oxygen species. The oxygen from the functional groups i.e. C=O and C-O bonds were centred at approximately 531 and 533 eV [55]. The intensity of the O 1s peak (**Fig. 3.7**d) significantly decreased after reduction as would be expected since most of the oxygen single-bonded to carbon groups were removed when forming rGO.

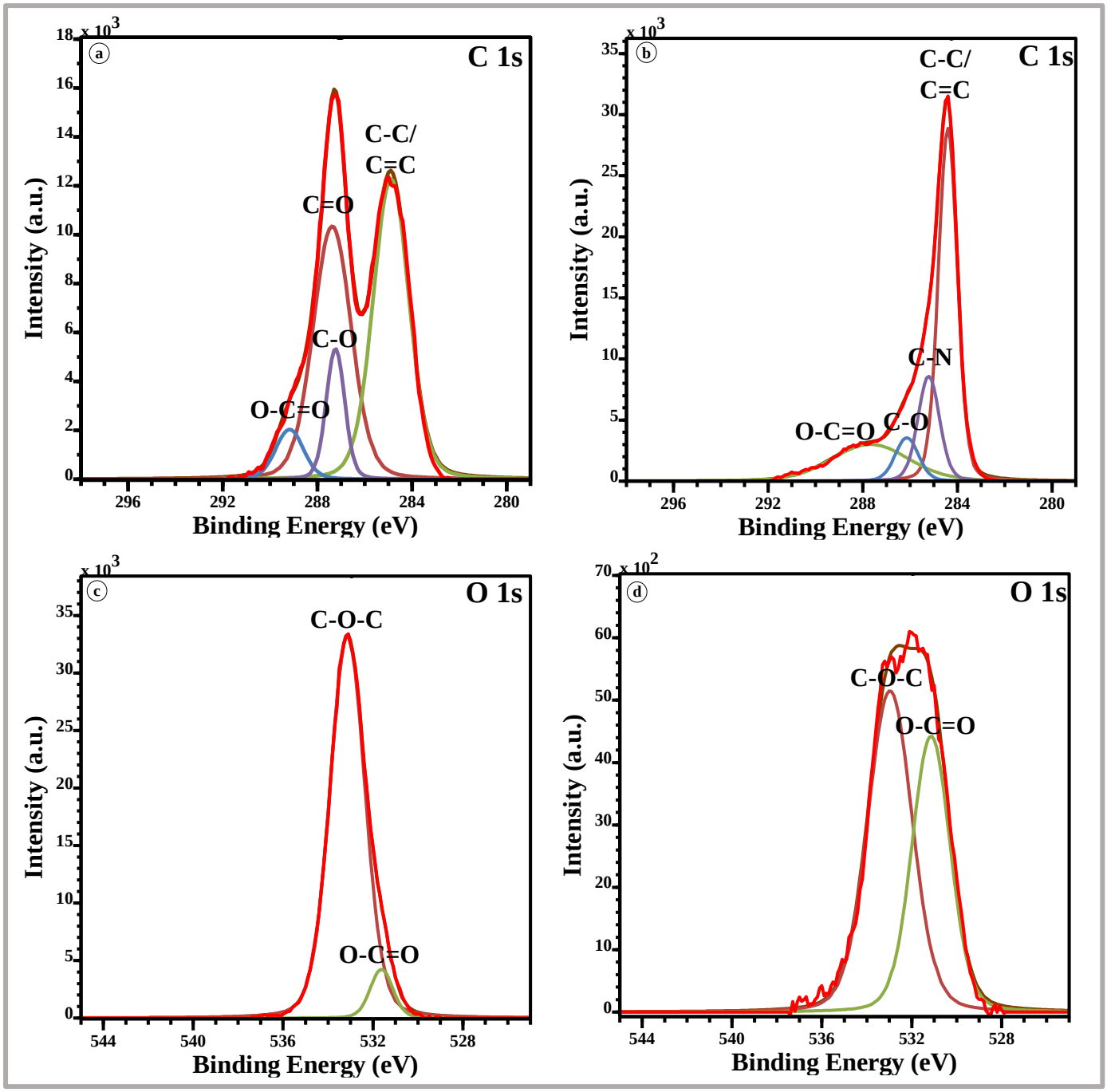

Figure 3. 7. XPS spectra of deconvoluted C 1s and O 1s peaks of GO (a & c) and mGH (b & d).

The incorporation of a heteroatom, N, is common during hydrazine reduction of graphene oxide [14, 31]. The N 1s core-level spectra in **Fig. 3.8** demonstrate the presence of three types of nitrogen species, pyridinic N (399.2 eV), pyrrolic N (400.6 eV) and graphitic N (401.5 eV) [31]. The pyridinic N and pyrrolic N species are bonded to two C atoms with one and two p-electrons in the π-conjucated system, respectively. The graphitic N species replaced some C atoms in the six-chained ring [53, 54]. The mechanism for obtaining the nitrogen has been

explained by Stankovich [31] and further explained using theoretical modelling by Gao [55]. However, the exact formation of the exact nitrogen species during the reduction reaction is not yet fully understood [14].

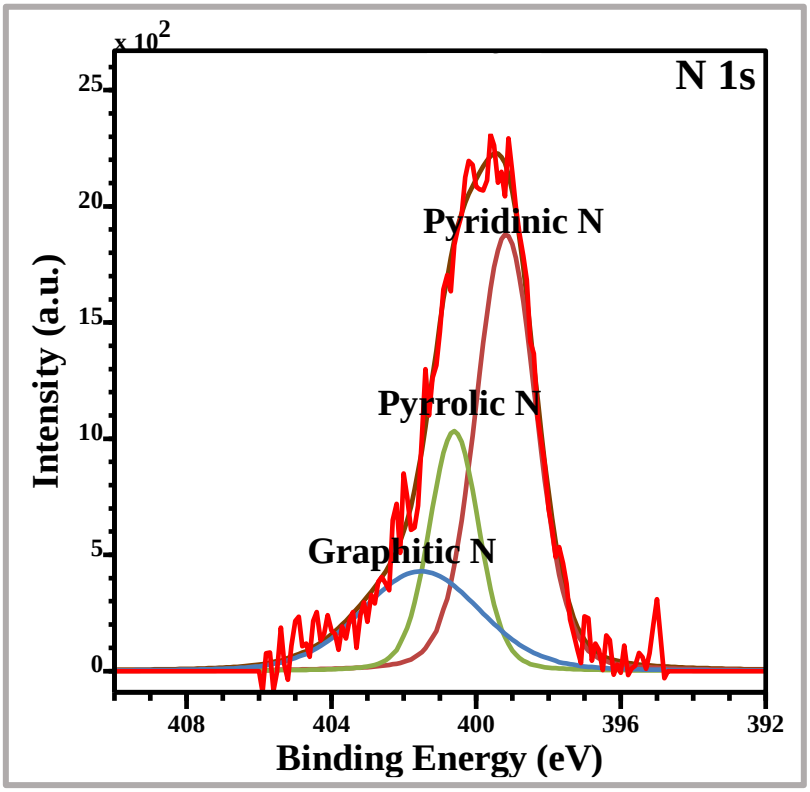

Figure 3. 8. High-resolution XPS spectra for N 1s of mGH.

3.5. Conclusions

Microwave hydrothermal reduction of graphene oxide has been presented as an environmentally friendly reduction strategy. XRD, Raman, FTIR and XPS confirmed the effectiveness of this technique. XRD patterns established the increase and decrease in stacking thickness of the graphite sheets after the oxidation and reduction processes. Raman spectroscopic analysis demonstrated that microwave reduction without any reducing agent could potentially be a competitor with hydrazine in inducing defects to the graphitic lattice. FTIR results showed that the removal of oxygen functionalities in the microwave-reduced samples could be comparable to the thermally reduced sample. Elemental composition results showed that the C/O ratio of the GO sheets increased from 1.99 to 7.8 after the microwave reduction with hydrazine reducing agent.

References

[1] Novoselov, K.S., Geim, A.K., Morozov, S.V., Jiang, D., Zhang, Y., Dubonos, S.V., Grogorieva, I.V., Firsov, A.A., Science **306** (2004) 666-669.

[2] Geim. A.K., Novoselov, K.S., Nature Materials **6** (2007) 183-191.

[3] Geim, A.K., Science **324** (2009) 1530-1534.

[4] De Silva, K.K.H., Huang, H-H., Joshi, R.K., Yoshimura, M, Carbon **119** (2017) 190-199.

[5] Hu, C., Song, L., Zhang, Z., Chen, N., Feng, Z., Qu, L, Energy & Environmental Science **8** (2015) 31-54.

[6] Hegab, H.M., Zou, L., Journal of Membrane Science **484** (2015) 95-106.

[7] Machado, B.F., Serp, P., Catalysis Science & Technology **2** (2012) 54-75.

[8] Lim, J.Y., Mubarak, N.M., Abdullah, E.C., Nizamuddin, S., Khalid, M., Inamuddin, Journal of Industrial Engineering Chemistry **66** (2018) 29-44.

[9] Guermoune. A., Chari, T., Popescu, F., Sabri, S.S., Guillemette, J., Skulason, H.S., Szkopek, T., Siaj, M., Carbon **49** (2011) 4204-4210.

[10] Son, I., Hwan Park, J., Kwon, S., Park, S., Rümmeli, M.H., Bachmatiuk, A., Song, H.J., Ku, J., Choi, J.W., Choi, J., Doo, S-G., Chang, H., Nature Communications **6** (2015) 7393.

[11] Jayasena, B., Subbiah, S., Nanoscale Research Letters **6** (2011) 95.

[12] Lavin-Lopez, M.P., Paton-Carrero, A., Sanchez-Silva, L., Valverde, J.L., Romero, A., Advanced Powder Technology **28** (2017) 3195-3203.

[13] Xie, X., Zhou, Y., Huang, K., Frontiers in Chemistry **7** (2019) 355.

[14] Dreyer, D.R., Park, S., Bielawski, C.W., Ruoff, R.S., Chemical Society Reviews **39** (2010) 228–240.

[15] Oliveira, A.E.F., Braga, G.B., Tarley, C.R.T., Periera A.C., Journal of Materials Science **53** (2018) 12005-12015.

[16] Park, S., An, J., Potts, J.R., Velamakanni, A., Murali, S., Ruoff, R.S., Carbon **49** (2011) 3019-3023.

[17] Kim, S., Choi, K., Park, S, Solid State Sciences **61** (2016) 40-43.

[18] Zheng, X., Peng, Y., Yang, Y., Chen, J., Tian, H., Cui, X., Zheng, W., Journal of Raman Spectroscopy **48** (2017) 97-103.

[19] Jung, I., Dikin, D.A., Piner, R.D., Ruoff, R.S., Nano Letters **8** (2008) 4283-4287.

[20] Matsumoto, Y., Morita, M., Kim, S.Y., Watanabe, Y., Koinuma, M., Ida, S., Chemistry Letters **39** (2010) 750-752.

[21] Chen, W., Yan, L., Bangal, P.R., Carbon **48** (2010) 1146-1152.

[22] Li, Z., Yao, Y., Lin, Z., Moon, K-S., Lin, W., Wong, C., Journal of Materials Chemistry **20** (2010) 4781-4783.

[23] Zhu, Y., Murali, S., Stoller, M.D., Veamakanni, A., Piner, R.D., Ruoff, R.S., Carbon **48** (2010) 2106-2122.

[24] Li, J., Yang, Z., Qiu, H., Dai, Y., Zheng, Q., Zheng, G-P., Yang, J., Journal of Material Chemistry A **1** (2013) 11451-11456.

[25] El-Khodary, S.A., El-Enany, G.M., El-Okr, M., Ibrahim, M., Electrochimica Acta **150** (2014) 269-278.

[26] Kimiagar, S., Rashidi, Nasim, N., Ghadim, E.E., Bulletin of Material Science **38** (2015) 1699-1704.

[27] Agusu, L., Ahmad, L.O., Anggara, D., Alimin, Mitsudo, S., Fujii, Y., Kikuchi, H., Journal of Physics: Conference Series **1011** (2018) 012012.

[28] Voiry, D., Yang, J., Kupferberg, J., Fullon, R., Lee, C., Jeong, H.Y., Shin, H.S., Chhowalla, M., Science **353** (2016) 1413-1416.

[29] Jiang, W.S., Yang, C., Chen, G-X., Yan, X-Q., Chen, S.N., Su, B-W., Liu, Z-B., Tian, J-G., Journal of Materials Chemistry C **6** (2018) 1829-1835.

[30] Elazab, H.A., Siamaki, A.R., Moussa, S., Gupton, B.F., El-Shall, M.S., Applied Catalysis A: General **491** (2015) 58-69.

[31] Stankovich, S., Dikin, D.A., Piner, R.D., Kohlhaas, K.A., Keinhammes, A., Jia, Y., Wu, Y., Nguyen, S.T., Ruoff, R.S., Carbon **45** (2007) 1558-1565.

[32] Chua, C.K., Pumera, M., Journal of Materials Chemistry A **1** (2013) 1892-1898.

[33] Moon, I.K., Lee, J., Ruoff, R.S., Lee, H., Nature Communications **1** (2010) 73.

[34] Zhang, J., Yang, H., Shen, G., Zhang, J., Guo, S., Chemistry Communications **46** (2010) 1112-1114.

[35] Kondrashov, V.A., Struchkov, N.S., Rozanov, R.Y., Nevolin, V.K., Kopylova, D.S., Nasibulinn, A.G., Nanotechnology **29** (2018) 035301-035308.

[36] Ji, T., Hua, Y., Sun, M., Ma, N., Carbon **54** (2013) 412-418.

[37] Mohandoss, M., Gupta, S.S., Nelleri, A., Pradeep, T., Maliyekkal, S.M., RSC Advances **7** (2017) 957-963.

[38] Mirzaei, A., Neri, G., Sensors and Actuators B **237** (2016) 749- 775.

[39] Khan, A., Jawaid, M., Neppolian, B., Asiri, A.M., *Graphene Functionalization Strategies: From Synthesis to Applications*, Singapore: Springer Nature (2019) 293-210.

[40] Menèndez, J.A., Arenillas, A., Fidalgo, B., Fernández, Y., Zubizarreta, L., Calvo, E.G., Bermúdez, J.M., Fuel Processing Technology **91** (2010) 1-8.

[41] Marcano, D.C., Kosynkin, D.V., Berlin, J.M., Sinitskii, A., Sun, Z., Slesarev, A., Alemany, L.B., Lu, W., Tour, J.M., ACS Nano **4** (2010) 4806-4814.

[42] Huang, H-H., De Silva, K.K.H., Kumara, G.R.A., Yoshimura, M., Scientific Reports **8** (2018) 6849.

[43] Díez, N., Śliwak, A., Gryglewicz, S., Gryzb, B., Gryglewicz, G., RSC Advances **5** (2015) 81831-81837.

[44] Shen, X., Lin, X., Yousefi, N., Jia, J., Kim, J-K., Carbon **66** (2014) 84-92.

[45] Ferrari, A.C., Robertson, J., Physical Review B **61** (2000) 14095-14107.

[46] Ferrari, A.C., Meyer, J.C., Scaraci, V., Casiraghi, C., Lazzeri, M., Mauri, F., Piscanec, S., Jiang, D., Novoselov, K.S., Roth, S., Geim, A.K., Physical Review Letters **97** (2006) 187401.

[47] Kaniyoor, A., Ramaprabhu, S., AIP Advances **2** (2012) 032183.

[48] Max, J., Chapados, C., The Journal of Physical Chemistry A **108** (2004) 3324-3337.

[49] He, D., Peng, Z., Gong, W., Luo, Y., Zhao, P., Kong, L., RSC Advances **5** (2015) 11966-11972.

[50] Alazmi, A., El Tall, O., Rasul, S., Hedhili, M.N., Patole, S.P., Costa, P.M.F.J., Nanoscale **8** (2016) 17782-17787.

[51] Fu, S., Ma, L., Gan, M., Wang, S., Zhang, X., Zhang, J., Zhou, T., Wang, H., Journal of Materials Science: Materials in Electronics **28** (2017) 3621-3629.

[52] Kumar, R. da Silva, E.T.S.G., Singh, R.K., Savu, R., Alaferdov, A.V., Fonseca, L.C., Carossi, L.C., Singh, A., Khandka, S., Kar, K.K., Alves, O.L., Kubota, L.T., Moshkalev, S.A., Journal of Colloid and Interface Science **515** (2018) 160-171.

[53] Li, Q., Liu, J., Bai, A., Li, P., Li, J., Zhang, X., Yu, M., Wang, J., Sun, H., Journal of Chemistry **1** (2019) 1-10.

[54] Phattharasupakun, N., Wutthiprom, J., Ma, N., Suktha, P., Sawangphruk, M., Journal of the Electrochemical Society **165** (2018) A1430-A1439.

[55] Gao, X., Jang, J., Nagase, S., Journal of Physical Chemistry C., **114** (2010) 832-842.

Chapter 4: Synthesis of Ni_3S_2-reduced graphene oxide composites

4.1. Introduction

The pursuit of attaining a material with impressive and desirable chemical, thermal and electrical properties has encouraged the engineering of composites or heterostructured material. Composites, which are made by combining metal oxides, transition metal chalcogenides, polymers, and/or carbon materials, have been prepared and proposed for the potential application in a variety of fields [1-3]. Composites can be defined as systems in which the materials of different compositions meets at the interfaces [4]. Walker and colleagues described the compositions or units as a backbone material and heterostructured material [5]. The backbone material contains the major conducting channels whereas the heterostructured material is the secondary material decorated on the backbone. Novel or improved physical and chemical properties usually emerge from the interfaces between the units [4-6].

Synthesis of nanocomposites usually follows three routes [7]: (a) sequential growth of the different material, (b) direct growth of the different building units and (c) concurrent growth of the different parts by regulating the building units. Various synthetic techniques have been employed namely; wet chemical approaches, solid-solid reactions, chemical vapour deposition, template-assisted synthesis and electrospinning [6, 7]. Graphene-nickel sulfide composites have received enormous attention due to their exceptional electrochemical properties [8]. Until now, researchers have employed many different methods to prepare these nanostructures [8-17]. The most common route is the hydrothermal route because it is environmentally benign, relatively inexpensive, is scalable and produces nanocomposites with high purity [8-10].

Xing and colleagues [9] prepared a nickel sulfide-graphene composite by hydrothermally reacting graphene oxide, $NiCl_2 \cdot 6H_2O$ and L-cysteine in a Teflon-lined autoclave at 160℃ for 6 hrs. Characterization by X-ray diffraction showed that two phases of nickel sulfide, NiS and NiS_2, were formed on the rGO sheets. Morphological studies revealed that the nickel sulfides had a spherical structure in tens of nanometres in size. Another group was able to synthesize only NiS blocked structures on graphene oxide using the same precursors, but at a longer reaction time and a lower temperature [10]. A colloidal synthesis method has been employed to prepare graphene wrapped-Ni_3S_4 nanoprisms [12]. The nanoprisms were uniformly dispersed on the graphene sheets prior to calcination, but agglomeration and wrapping of nanoprisms with graphene sheets occurred once calcined under argon. A mixture of spherical

nickel sulfides on rGO sheets were obtained by varying the ratio of precursors using spray pyrolysis with the hot well reactor operated at 800℃ for 8 s [13]. These composites were synthesized in one pot and did not require any further heat treatment. A 3D porous graphene network with Ni_3S_2 nanoparticles were obtained by employing a quasi-chemical vapour deposition method [14]. The authors used nickel foam as a catalytic skeleton and thiourea resin as carbon and sulfur precursors with the reaction temperature adjusted between 600℃ and 900℃ for 30 minutes.

The high reaction temperatures and long reaction times of the above-mentioned methods are often disadvantageous. Microwave synthesis technology has been reported as a possible solution to these challenges, however few reports are available in literature on the microwave synthesis of nickel sulfide-graphene composites, especially Ni_3S_2-rGO. Qin [15] synthesized layered Ni_3S_2-rGO composites using a microwave hydrothermal technique. These composites were obtained by mixing GO, $NiCl_2 \cdot 6H_2O$ and thiourea during a one-step procedure performed for 10 minutes at 100 W without the addition of any surfactant or reducing agent followed by annealing. Hu and co-workers [16] also obtained a layered composite by employing the same method as Qin but they were able to completely reduce graphene oxide to graphene without the additional annealing step. Recently, graphene-NiS/ Ni_3S_2 composites were acquired using a two-step microwave procedure where Ni particles were firstly decorated on the graphene sheets followed by the sulfurization of those particles using thiourea as a sulfur source [17]. The $NiCl_2 \cdot 6H_2O$ and graphene oxide were simultaneously reduced to Ni and graphene using hydrazine hydrate as a reducing agent under the microwave irradiation of 600 W for 4 minutes. The sulfurization step proceeded at the same power in only 3 minute thus the combined reaction time of the two steps for obtaining graphene decorated with quasi-spherical nickel sulfide nanoparticles was less than 10 minutes.

In this study, Ni_3S_2-reduced graphene oxide composites were synthesized using an in-situ microwave method and by physically mixing previously prepared Ni_3S_2 and rGO.

4.2. Experimental procedure

Sodium hydroxide (NaOH, 99%) was purchased from Sigma Aldrich, South Africa and used as is. The other materials used in the synthesis were used without any further purification (unless stated otherwise) as mentioned in **Chapter 2.2** and **Chapter 3.2**.

4.2.1. Preparation of composites using an in-situ sulfurization microwave technique

Nickel sulfide-reduced graphene oxide composites were synthesized using a sulfurization method reported in [17] with a few modifications.

4.2.1.1. Synthesis of rGO-Ni composites

rGO-Ni composites were prepared by dispersing 200 mg of GO in ethylene glycol (1 mg/mL) by ultra-sonication. 0.792 g of $NiCl_2 \cdot 6H_2O$ was added to the GO solution and sonicated to produce a homogeneous solution. Furthermore, 6.8 mL of hydrazine hydrate and 1.4 g of NaOH were added and stirred to ensure homogeneity of the reaction mixture. The latter was transferred into Teflon-lined microwave vessels and placed in a microwave reactor (Anton Paar Multiwave 3000) operated at 600 W for 4 minutes followed by fan cooling to room temperature. The obtained powder was centrifuge washed with distilled water and ethanol a few times and dried at 60℃ overnight.

4.2.2.2. Synthesis of rGO-nickel sulfide composites

1.2 g of the rGO-Ni composite was dissolved in 80 mL of distilled water by ultra-sonication. Thereafter, 0.2 g of thiourea was added to the composite solution and the reaction mixture was stirred for homogeneity. This solution was placed in Teflon-lined microwave vessels and placed in the microwave reactor that was operated at 600 W for 3 minutes and fan cooled to room temperature. The as-obtained black product was centrifuge washed with water and ethanol and dried overnight at 60℃.

A composite with a lower nickel sulfide loading was synthesized by using 0.396 g of $NiCl_2 \cdot 6H_2O$ and 0.1 g of thiourea. The rGO-Ni composites were labelled as AGNi and BGNi and the corresponding rGO-nickel sulfide composites as AGNS and BGNS.

4.2.2. Preparation of composites via an ex-situ technique

Composites made up of 5 and 10% Ni_3S_2 were synthesized by mixing 5 mg and 10 mg of Ni_3S_2-W (prepared in **Chapter 2**) with 95 mg and 90 mg of rGO (mGH as prepared in **Chapter 3**), respectively. The rGO and Ni_3S_2 were both dispersed in ethanol (1 mg/mL) by ultra-sonication for 1 hour. The two solutions were mixed together and further sonicated for 2 hours, the solvent evaporated and the black powder dried at 100℃ for 2 hours.

4.2.3. Characterization

X-ray diffraction (XRD), Transmission electron microscopy (TEM), High magnification transmission electron microscopy (HM-TEM), Laser Raman spectroscopy, Fourier transform infrared (FTIR) spectroscopy, Brunauer-Emmett-Teller (BET) surface area analysis and X-ray spectroscopy (XPS) techniques were used to analyse the structural, morphological and chemical properties of the as-synthesized materials.

4.3. Results and discussion

4.3.1. Phase analysis

X-ray diffraction analysis was performed on the materials to determine their phase structures. The XRD patterns for the composites prepared via the in-situ method are represented in **Fig. 4.1**a and b. As seen in **Fig. 4.1**a, the rGO with Ni exhibited major peaks at 2θ values of 44.7°, 52.1° and 76.8° attributed to the (111), (200) and (220) planes of Ni (PDF 01-071-4655). The broad peak in the 12°-26° region could be attributed to the overlap of the (001) and (002) planes of carbon suggesting that removal of the oxygen functional groups between the sheets of GO during reduction was not complete [18]. After sulfurization, AGNS contained peaks that corresponded to carbon (PDF 00-008-0415), NiS (PDF 00-003-0760) and Ni_3S_2 (PDF 00-030-0863) whereas BGNS comprised of planes due to the presence of carbon, $Ni(OH)_2$ (PDF 00-057-0907) and Ni_3S_2.

As previously mentioned, thermodynamically the melting point of Ni_3S_2 is lower than that of NiS and the free energy formation of Ni_3S_2 is much smaller than that of NiS [19]. Therefore, the formation of Ni_3S_2 was expected to be much easier than the formation of NiS under the same conditions. This could possibly explain why more intense Ni_3S_2 planes were observed in AGNS compared to NiS.

The formation mechanism of the nickel sulfide and nickel hydroxide products in BGNS is suggested by **Eq. 4.1-4.4**. During the reaction of thiourea with water, H_2S was released as a decomposition product of thiourea with increasing temperature (**4.1**) and it was responsible for the S^{2-} ions during the sulfurization process (**4.2**). The Ni was further oxidized by the small amounts of dissolved O_2 with the help of thiourea and reacted with the OH^- ions to form $Ni(OH)_2$ (**4.3**) [19]. Thiourea not only acted as a sulfur source, but it also has a tendency to oxidize. The S^{2-} from the decomposition of thiourea combined with the $Ni(OH)_2$, forming

$Ni(OH)_xS_y$ (**4.4**). The continuous incorporation of S^{2-} and the replacement of OH^- lead to the transformation of $Ni(OH)_2$ to $Ni(OH)_xS_y$ and eventually Ni_3S_2 (**4.5**).

$$NH_2CSNH_2 + H_2O \rightarrow H_2S + 2NH_3 + CO_2 \quad (\mathbf{4.1})$$

$$NH_2CSNH_2 + 4OH^- \rightarrow 2NH_3 + CO_3^{2-} + S^{2-} + H_2O \quad (\mathbf{4.2})$$

$$Ni + O_2 + OH^- \rightarrow Ni(OH)_2 \quad (\mathbf{4.3})$$

$$Ni(OH)_2 + S^{2-} \rightarrow Ni(OH)_xS_y \quad (\mathbf{4.4})$$

$$Ni(OH)_xS_y + S^{2-} \rightarrow Ni_3S_2 \quad (\mathbf{4.5})$$

The decomposition of thiourea into S^{2-} increase with an increase in temperature and time and thus sometimes $Ni(OH)_2$ is a resulting product during the reaction of nickel and thiourea [20]. Hence, the presence of mostly $Ni(OH)_2$ peaks instead of Ni_3S_2 in BGNS could assumedly be attributed to this.

In the diffractograms of the products synthesized by physically mixing Ni_3S_2 and rGO, the relative intensities of the reflection planes of Ni_3S_s (PDF 00-030-063) decreased with an increase in the amount of rGO (PDF 00-008-0415) (**Fig. 4.1**c). In the 5% Ni_3S_2-rGO the nickel sulfide peaks were almost completely diminished due to its low content in the composite. Additionally, the refection planes of both nickel sulfide and rGO slightly shifted to higher 2θ values upon the formation of the composite (**Fig. 4.1**d).

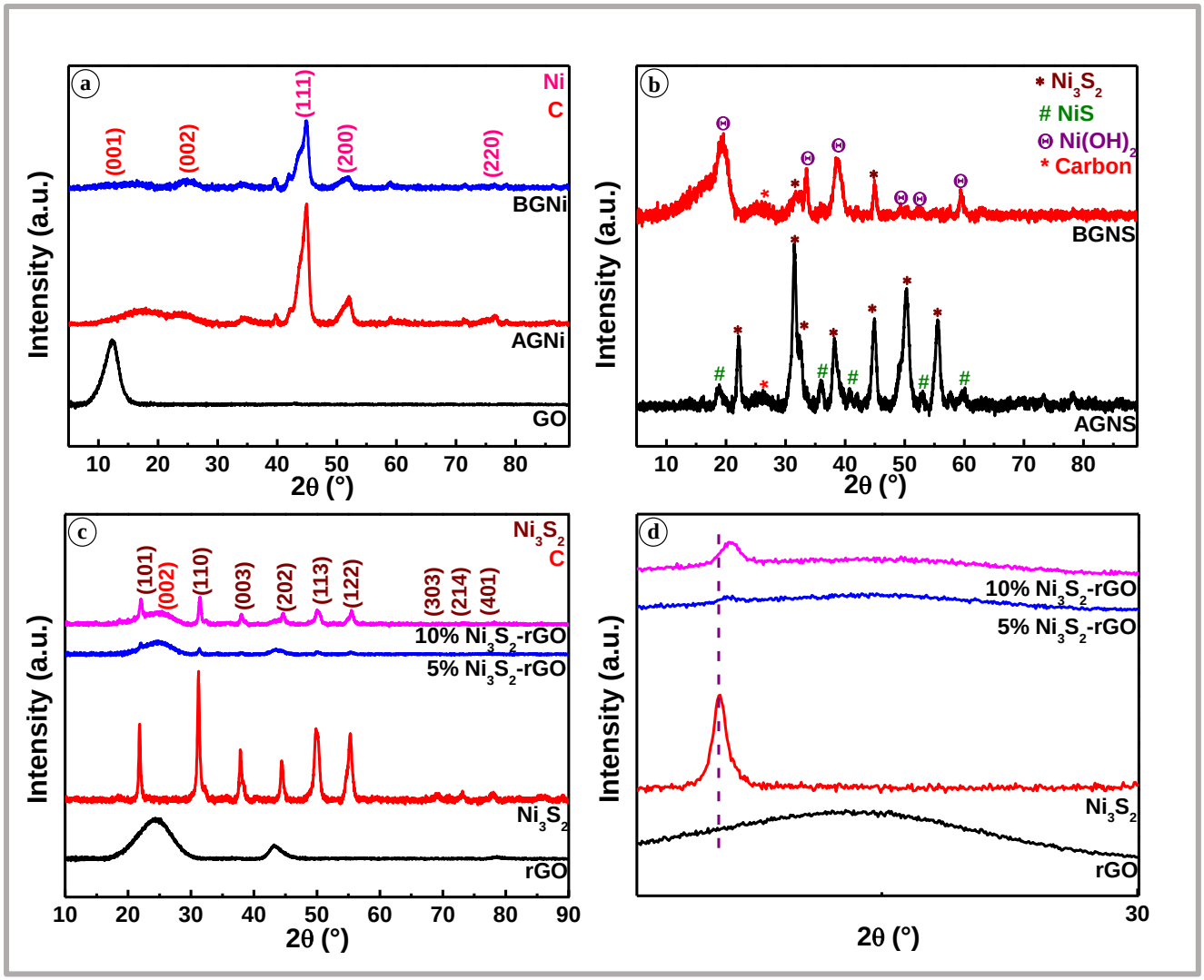

Figure 4. 1. X-ray diffractograms of GNi (a), GNS (b), NS-rGO (c) and zoomed-in image of NS-rGO spectra (d).

4.3.2. Microscopy analysis

The morphologies of the as-obtained material were investigated using TEM. Observed from **Fig. 4.2**a (AGNi), the Ni particles on the rGO sheets have a quasi-spherical morphology and appeared agglomerated covering most of the sheet. When a lower Ni concentration was loaded, the quasi-spherical particles appeared to be less and leaving some areas of the rGO sheet exposed (**Fig. 4.2**b). After sulfurization, there was not a noticeable difference between AGNi and AGNS (**Fig. 4.2**c). However, BGNS (**Fig. 4.2**d-f) had additional blade-like structures to the quasi-spherical structures in BGNi. The blade-like or rod-like structures could assumedly be the $Ni(OH)_2$ formed on the rGO sheets.

The samples synthesized by mixing the Ni_3S_2 and rGO prepared in the previous chapters are shown in **Fig. 4.3**. It was noticed that the initial sonication of nickel sulfide combined with the sonication during the mixing with rGO could have possibly broken down most of the initial quasi-spherical flower-like Ni_3S_2 structures (**Fig. 4.3**a) into layer-based flower-like structures (**Fig. 4.3**c,d) that were incorporated onto the rGO sheets. The high magnification TEM image showed the clear distinction between the Ni_3S_2 and rGO (**Fig. 4.3**e).

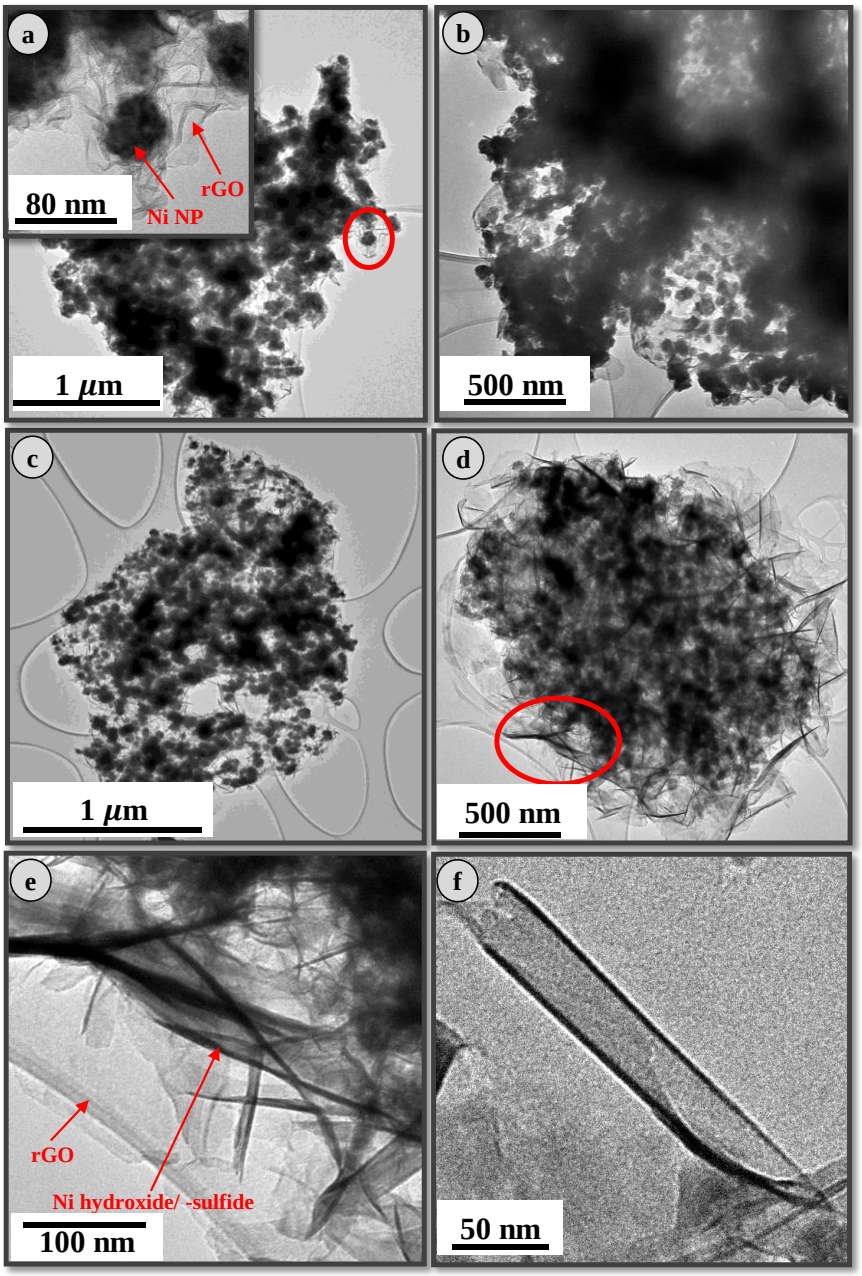

Figure 4. 2. TEM micrographs of AGNi (a), BGNi (b), AGNS (c), BGNS (d), and zoomed-in images of BGNS (e,f).

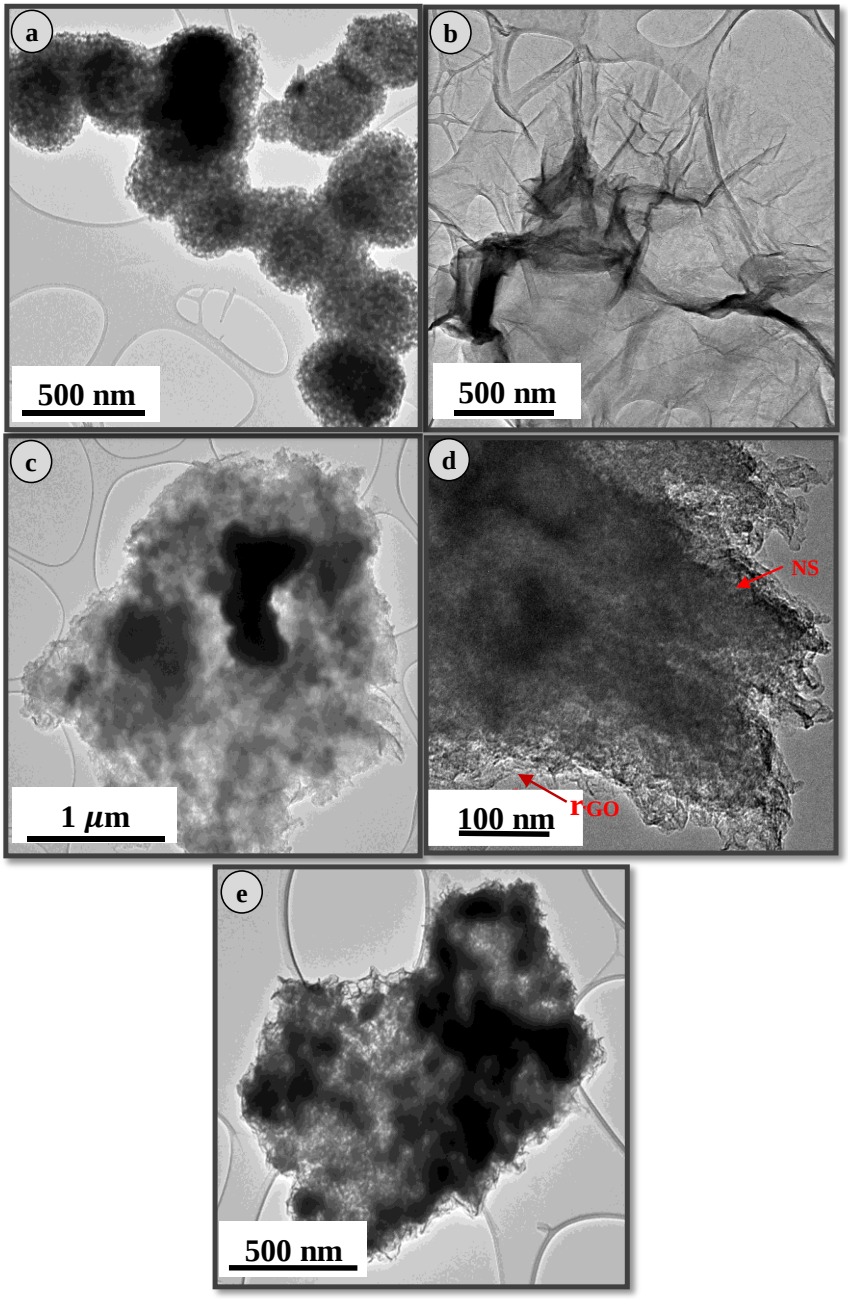

Figure 4. 3. TEM images of Ni_3S_s (a), rGO (b) and 5 % Ni_3S_s-rGO (c); high magnification TEM image of 5 % Ni_3S_s-rGO and TEM micrograph 10 % Ni_3S_s-rGO (f).

4.3.3. Functional group analysis

The FTIR spectra of the composites synthesized in situ and ex situ are represented in **Fig. 4.4**. The functional groups in GO (**Fig. 4.4**a) were clearly visible, namely; OH (3602 cm^{-1} and 1383 cm^{-1}), C=O (1623-1734 cm^{-1}) and C-O/ C-O-C (980 cm^{-1}, 1054 cm^{-1} and 1226 cm^{-1}) [21-24]. Upon incorporation of Ni with the addition of hydrazine, the –OH functional groups disappeared in both AGNi and BGNi. A NH_2 bending mode (1564 cm^{-1}) was present in both AGNi and BGNi possibly from the hydrazine [25, 26]. In BGNi, the presence of a C-N

stretching vibration at 1209 cm^{-1} that could be ascribed to the incorporated nitrogen from hydrazine was noticed [26,27]. Post sulfurization, AGNS as well as BGNS had a peak at approximately 1062 cm^{-1}, which indicated the presence of a sulfur containing group [28, 29]. The OH vibrational band reoccurred in BGNS at ~ 3639 cm^{-1} indicating the presence of $Ni(OH)_2$ [30, 31].

The 5 and 10% Ni_3S_2-rGO samples displayed peaks at 2986 cm^{-1}, 1582 cm^{-1}, 1461 cm^{-1} and 1073 cm^{-1} corresponding to symmetric stretching vibrations of CH_2, C=C stretching modes of aromatic alkenes, the in-plane scissoring of the alkyl C-H vibrations and the C-O of alkoxy groups of the rGO, respectively [23, 32]. The vibrations due to the Ni_3S_2 were weakened because of the low percentage loading.

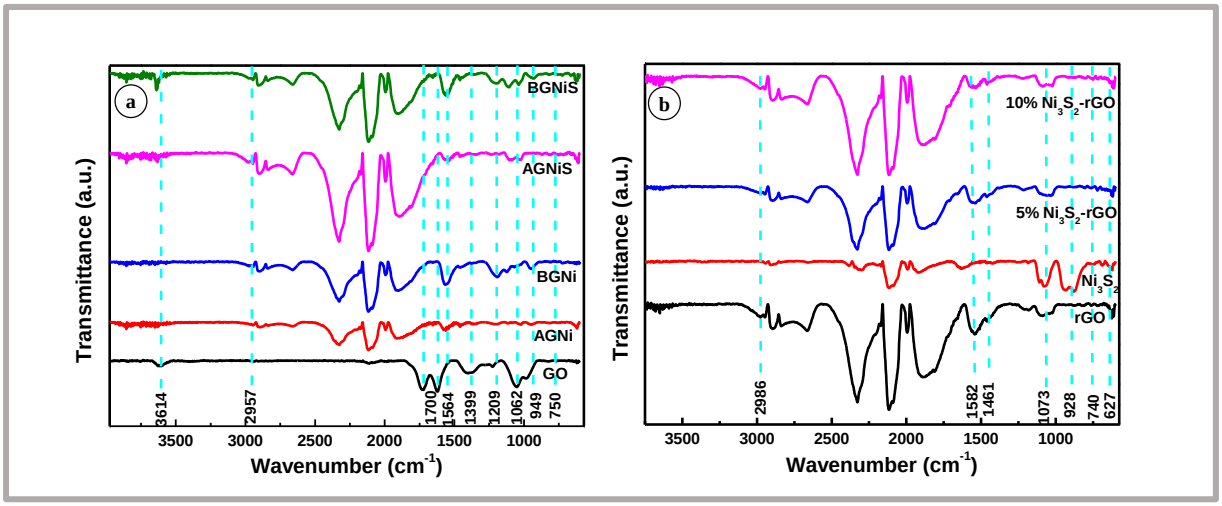

Figure 4. 4. FTIR spectra of samples prepared in-situ (a) and ex-situ (b).

4.3.4. Surface area and elemental composition analysis

The 5% Ni_3S_2-rGO composite was further analysed using BET and XPS. N_2 adsorption/desorption isotherm analysis was used to determine the specific surface area of 5% Ni_3S_2-rGO. As displayed in **Fig. 4.5**a, a typical type IV isotherm with a distinct hysteresis loop between a relative pressure of 0.4 and 1 was observed, revealing the existence of mesopores in the composite [33]. The BET surface area was determined as 772.7 m^2/g, which was larger than that of Ni_3S_2 (42.3 m^2/g) and lower than that of rGO (815.2 m^2/g). The composite had a pore volume of 0.61 cm^3/g. The large surface area suggested that the material had a good number of active sites desirable for gas adsorption [34]. The sizes of the pores were approximately centred at 3.5 nm as demonstrated in the pore size distribution curve (**Fig. 4.5**b).

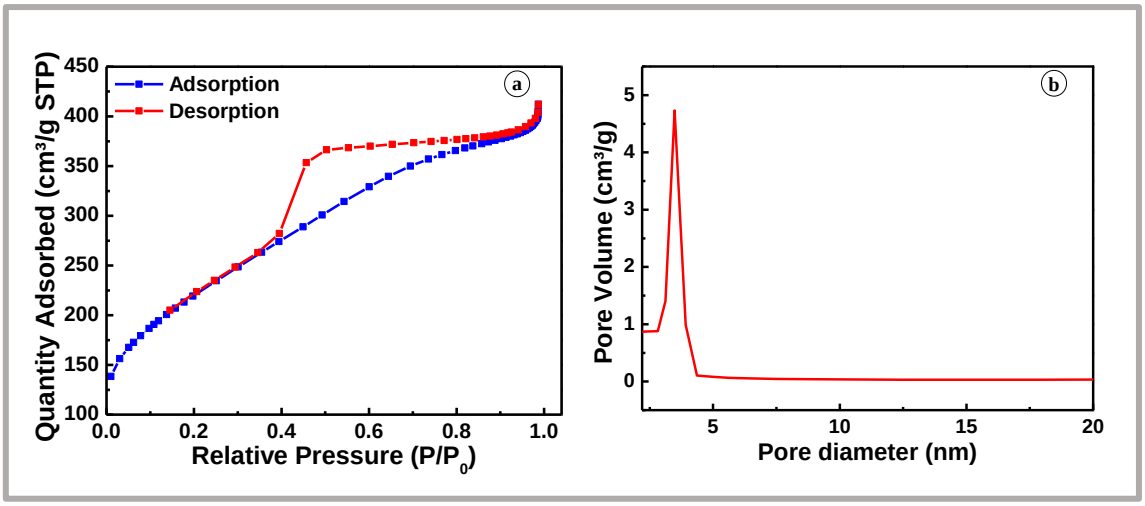

Figure 4. 5. N_2 adsorption/desorption isotherm (a) and pore size distribution curve (b) of 5% Ni_3S_2-rGO.

X-ray spectroscopy (XPS) was utilized to determine the chemical composition and the results are illustrated in **Fig. 4.6**. The survey spectra **(Fig. 4.6**a) has distinct peaks at 284.7 eV, 399.8 eV and 532.0 eV, which were attributed to C 1s, N 1s and O 1s of the rGO, respectively. Nitrogen was present from the hydrazine hydrate that was used to reduce the graphene oxide. The peaks associated with the nickel (~ 860 eV) and sulfur (~ 163 eV) were weakened due to the low concentration of Ni_3S_2 in the composite. The peaks in the C 1s spectra (**Fig. 4.6**b) could be deconvoluted into three peaks at 284.4 eV, 285.0 eV and 286.6 eV associated with C-C/C=C, C-O/ C-N, and C=O, respectively [35]. The O 1s spectra (**Fig. 4.6**c) of the composite was deconvoluted into two peaks centred at 531.1 eV and 532.9 eV, which corresponded to the O-C=C and C-O-C oxygen species in the composite, respectively [35]. The nitrogen species that were present in the composite were pyridinic N (398.6 eV), pyrrolic N (400.0 eV) and graphitic N (401.6 eV) in N 1s spectra as illustrated in **Fig. 4.6**d [26]. The peaks at 856.6 eV and 874.8 eV in the Ni 2p spectra (**Fig. 4.6**e) were in good agreement with the Ni $2p_{3/2}$ and Ni $2p_{1/2}$ orbitals in Ni_3S_2 [37]. The XPS core-level spectra of sulfur in **Fig. 4.6**f show a sulfur peak at 169 eV, which was ascribed to S $2p_{3/2}$ orbital of S^{2-} [38]. We also noted a shift in the peak positions in the different spectra when compared with the peaks in pristine Ni_3S_2 (**Chapter 2**) and rGO (**Chapter 3**). These shifts in binding energy suggested a strong interaction between the incorporated nickel sulfide and rGO leading to a redistribution of charge at the surface [39-41]. These XPS results indicated that the Ni_3S_2 was incorporated into rGO with success.

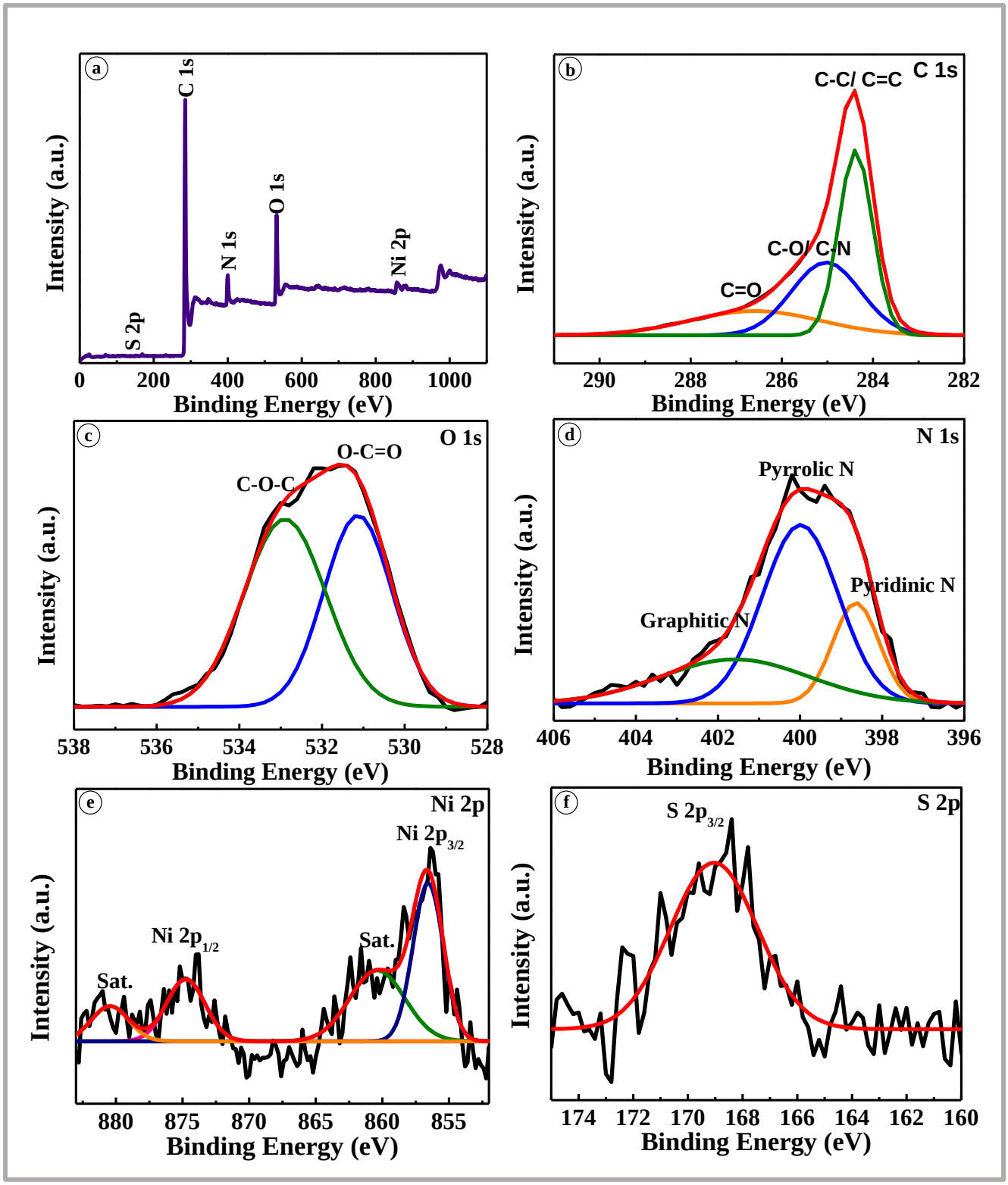

Figure 4. 6. Full-scan XPS spectra (a), C 1s XPS spectra (b), O 1s XPS spectra (c). N 1s XPS spectra (d), Ni 2p XPS spectra (e), and S 2p XPS spectra (f) of 5% Ni_3S_2-rGO.

4.4. Conclusions

A two-step microwave sulfurization method and an ex situ method have been used to prepare nickel sulfide-reduced graphene oxide composites. The sulfurization method embedded quasi-spherical nanoparticles consisting of a mixture of two nickel sulfide phases (NiS and Ni_3S_2) onto the reduced graphene oxide sheets. When the concentration of the catalysts was reduced, XRD revealed that the obtained rGO composite comprised of $Ni(OH)_2$ and Ni_3S_2. The morphological results of the latter displayed blade-like structures in addition to the nanospheres. Physical mixing of previously prepared Ni_3S_2 and rGO produced rGO composites with 5 and 10% Ni_3S_2. XRD, TEM and XPS analysis showed that quasi-spherical flower-like Ni_3S_2 nanostructures were broken down into nanosheets by ultra-sonication that were successfully incorporated onto the rGO sheets. The high surface area of the 5% Ni_3S_2-rGO composite suggest that it could be advantageous for application in catalysis and sensing.

References

[1] Bag, A., Lee, N.E., Journal of Materials Chemistry C **7** (2019) 13367-13383.

[2] Pomerantseva, E., Gogotsi, Y., Nature Energy **2** (2017) 17089.

[3] Deng, D., Novoselov, K.S., Fu, Q., Zheng, N., Tian, Z., Bao, X., Nature Nanotechnology **11** (2016) 218-230.

[4] Zheng, H., Li, Y., Liu, H., Yin, X., Li, Y., Chemical Society Reviews **40** (2011) 4506-4524.

[5] Walker, J.M., Akbar, S.A., Morris, P.A., Sensors and Actuators B **286** (2019) 624-640.

[6] Carbone, L., Cozzoli, P.D., Nano Today **5** (2010) 449-493.

[7] Bhagyaraj, S.M., Oluwafemi, O.S., Kalarikkal, N., Thomas, S, Synthesis of Inorganic Nanomaterials: Advances and Key Technologies, Woodhead Publishing **1** (2018) 89-117.

[8] Reddy, B.J., Vickraman, P., Justin, A.S., Applied Surface Science **483** (2019) 1142-1148.

[9] Xing, Z., Chu, Q., Ren, X., Tian, J., Asiri, A.M., Alamry, K.A., Al-Youbi, A.O., Sun, X., Electrochemistry Communications **32** (2013) 9-13.

[10] Wang, A., Wang, H., Zhang, S., Mao, C., Song, J., Niu, H., Jin, B., Tian, Y., Applied Surface Science **282** (2013) 704-708.

[11] Liu, X., Qi, X., Zhang, Z., Ren, L., Liu, Y., Meng, L., Huang, K., Zhong, J., Ceramics International **40** (2014) 8189-8193.

[12] AbdelHamid, A.A., Yang, X., Yang, J., Chen, X., Ying, J.Y., Nano Energy **26** (2016) 425-437.

[13] Lee, S.M., Ko, Y.N., Choi. S.H., Kim, J.H., Kang, Y.C., Electrochimica Acta **167** (2015) 287-293.

[14] Li, B., Li., Z., He, F., Pang, Q., Shen, P., International Journal of Hydrogen Energy **44** (2019) 30806-30819.

[15] Qin, W., Chen, T., Lu, T., Chia, D.H.C., Pan, L., Journal of Power Sources **302** (2016) 202-209.

[16] Hu, P. Liu, X., Liu, B., Li, L., Qin, W., Yu, H., Zhong, S., Li, Y., Ren, Z., Wang, M., Journal of Colloid and Interface Science **496** (2017) 254-260.

[17] Zhou, S., Huang, Y., Xu, L., Zheng, W., Ceramics International **44** (2018) 21786-21793.

[18] Sharma, P., Tuteja, S.K., Bhalla, V., Shekhawat, G., Dravid, V.P., Suri, C.R., Biosensors and Bioelectronics **39** (2013) 99-105.

[19] He, H., Chen, A., Lv, H., Dong, H., Chang, M., Li, C., Journal of Alloys and Compounds **574** (2013) 217-220.

[20] Yang, J., Duan, X., Qin. Q., Zheng, W., Journal of Materials Chemistry A **1** (2013) 7880-7884.

[21] Lavin-Lopez, M.P., Paton-Carrero, A., Sanchez-Silva, L., Valverde, J.L., Romero, A., Advanced Powder Technology **28** (2017) 3195-3203.

[22] Zheng, X., Peng, Y., Yang, Y., Chen, J., Tian, H., Cui, X., Zheng, W., Journal of Raman Spectroscopy **48** (2017) 97-103.

[23] He, D., Peng, Z., Gong, W., Luo, Y., Zhao, P., Kong, L., RSC Advances **5** (2015) 11966-11972.

[24] Alazmi, A., El Tall, O., Rasul, S., Hedhili, M.N., Patole, S.P., Costa, P.M.F.J., Nanoscale **8** (2016) 17782-17787.

[25] Muthu, N.S., Gopalan, M., Applied Surface Science **480** (2019) 186-198.

[26] Stankovich, S., Dikin, D.A., Piner, R.D., Kohlhaas, K.A., Keinhammes, A., Jia, Y., Wu, Y., Nguyen, S.T., Ruoff, R.S., Carbon **45** (2007) 1558-1565.

[27] Yin, P.F., Zhou, C., Han, X.Y., Zhang, Z.R., Xia, C.H, Sun, L.L., Journal of Alloys and Compounds **620** (2015) 42-47.

[28] Wang, X., Hu, J., Su, Y., Hao, J., Liu, F., Han, S., An, J., Lian, J., Chemistry A European Journal **23** (2017) 4128-4136.

[29] Kristl, M., Dojer, B., Gyergyek, S., Kristl, J., Heliyon **3** (2017) e00273.

[30] Xu, X., Yu, J., Liu, G., Cheng, B., Zhou. P., Li, X., Dalton Transactions **42** (2013) 10190-10197.

[31] Kumar, N.S., Ganapathy, M., Sharmila, S., Shankar, M., Vimalan, M., Potheher, I.V., Journal of Alloys and Compounds **703** (2017) 624-632.

[32] Fu, S., Ma, L., Gan, M., Wang, S., Zhang, X., Zhang, J., Zhou, T., Wang, H., Journal of Materials Science: Materials in Electronics **28** (2017) 3621-3629.

[33] Chen, J.S., Zhu, T., Hu, Q.H., Gao, J., Su, F., Qiao, S.Z., Lou, X.W., ACS Applied Materials & Interfaces **2** (2010) 3628-3635.

[34] Yang, F., Song, P., Ruan, M., Xu, W., FlatChem **18** (2019) 100133.

[35] Li, Q., Liu, J., Bai, A., Li, P., Li, J., Zhang, X., Yu, M., Wang, J., Sun, H., Journal of Chemistry **2019** (2019) 1-10.

[36] Gao, X., Jang, J., Nagase, S., Journal of Physical Chemistry C., **114** (2010) 832-842.

[37] Wang, Y.L., Wei, X.Q., Li, M.B., Hou, P.Y., Xu, X.J., Applied Surface Science **436** (2018) 42-49.

[38] Zheng, J.H., Zhang, R.M., Wang, X.G., Materials Letters **228** (2018) 191-194.

[39] Guo, D., Zhang, Z., Xi, B., Yu, Z., Zhou, Z., Chen, X., Journal of Materials Chemistry **8** (2020) 3834-3844.

[40] Qin, J.F., Yang, M., Hou, S., Dong, B., Chen, T.S., Ma, X., Xie, J.Y., Zhou, Y.N., Nan, J., Chai, Y.M., Applied Surface Science **502** (2020) 144172.

[41] Wu, C., Liu, B., Wang, J., Su, Y., Yan, H., Ng, C., Li, C., Wei, J., Applied Surface Science **441** (2018) 1024-1033.

Chapter 5: Application of nickel sulfide-reduced graphene oxide composites in sensing devices

5.1. Introduction

The quality of indoor-air has recently been threatened due to the increased presence of volatile organic compounds (VOCs), such as acetone, benzene, ethanol, methanol, toluene and xylene [1-3].VOCs are defined by the United States Environmental Protection Agency as "chemical compounds whose composition makes it possible for them to evaporate under normal indoor atmospheric conditions of temperature and pressure" [2]. Generally, these organic compounds are colourless, tasteless, have very low boiling points and often times are very difficult to detect because they are mixed with other interfering gases [1-2].

Reports reveal that the concentrations of VOCs indoors are almost 10 times higher in comparison to outdoor concentrations [2]. This is because nearly all products found in our homes, workplaces, hospitals and schools are sources of VOCs including aerosol products, food and beverages, paint, ink printers and medication. A prolonged exposure to some VOCs can adversely affect the health of human beings possibly causing digestive tract cancer, respiratory disease and sick house (or building) syndrome [2, 4].

Acetone is a highly volatile and combustible compound and when exceeding a concentration of 173 ppm, can cause damage to the nose, eyes and the central nervous system [2, 5]. Ethanol, an extensively used solvent, is also a highly flammable and colourless liquid [6]. Exposure to ethanol is not life-threatening, however, it can cause drowsiness, headaches and difficulty in breathing. Another extensively used solvent is methanol, which has an indoor concentration limit of 200 ppm [2]. The inhalation, ingestion or absorption of methanol on the skin can cause irreversible damage to the eyes and nervous system and even death if not immediately treated because it metabolizes into toxic formaldehyde and formic acid [7]. Toluene is another acutely toxic compound used in paint thinners, inks and fuel, pharmaceutical and chemical industries. It has the ability of negatively affecting the central nervous system, skin, kidneys and liver. The threshold limit for indoor exposure is 0.07 ppm [8]. In essence, it is important to develop tools for the efficient detection and monitoring of these substances in our environments.

Various analytical tools are capable of detecting VOCs with high accuracy and precision, for example high performance liquid chromatography, gas chromatography and mass spectrometry

[2, 8]. However, these techniques are time consuming, requiring on-site sampling of the indoor air before analysis [1-2, 8]. Additionally, these samples need to undergo pre-treatment prior to analysis and the operation of the equipment is complicated needing highly skilled operators. Employing these techniques are not advantageous as they are expensive and not possible for real-time applications. Researchers have devoted much time on developing miniaturized sensing devices using resistive principles as a less expensive, portable and simpler solution with the advantage of obtaining real-time data without the need of complex instrumentation.

Different hybrid materials made up of carbon materials, such as graphene and its derivatives [1, 9-10], carbon nanotubes [11, 12] and carbon spheres [5] with metals, metal oxides, metal sulfides and polymers have previously been suggested as possible candidates for detecting some VOCs. Kwon and colleagues [11] showed the selective detection of toluene gas in the ppm ranges at 150 ℃ using Pt-decorated multi-walled carbon nanotubes (MWCNTs). The authors observed that the incorporation of Pt nanoparticles onto the MWCNTs improved the sensor response by up to 311.4% and it also significantly decreased the response and recovery times. When Co_3O_4 was assembled on the surface of hollow carbon spheres, the hollow spheres enhanced the interaction between the acetone molecules and the Co_3O_4 [5]. In another study, Fe_3O_4 nanocubes embedded on flake-like carbon exhibited excellent low temperature sensing behaviour to 100 ppm ethyl acetate, acetic acid, ethanol and methanol vapours [1]. Liang compared this composite with other Fe_3O_4 based materials and reported that it showed superior sensing behaviour in terms of sensing temperature, detection limit and sensitivity.

Recently, Kim and colleagues used a Ni_3S_2 sensor to detect non-enzymatic glucose [13]. This electrochemical sensor exhibited high electro catalytic activity towards glucose oxidation, a wide detection range, a low detection limit and great selectivity in the presence of other electroactive species. Ni_3S_2 has also been used for humidity sensing [14]. The authors reported that the sensor showed a response of up to 116 for 63% RH, which was higher than other reported metal sulfide humidity sensors.

This study describes the potential application of nickel sulfide-reduced graphene oxide composites in the room temperature detection of VOCs. The linearity, sensitivity and response-recovery properties of the sensing material was investigated. Finally, a gas sensing mechanism was also proposed.

5.2. Experimental

The gas sensors were prepared using Ni_3S_2, rGO, (5%) Ni_3S_2-rGO, (10%) Ni_3S_2-rGO and in situ prepared NS-rGO as reported in **Chapter 2**, **3** and **4**. N, N-dimethylformamide ($HCON(CH_3)_2$, 99.8%), anhydrous ethylene glycol ($C_2H_6O_2$, 99.8%), acetone (CH_3COCH_3, 99.5%), ethanol (CH_3CH_2OH, 99%), methanol (CH_3OH, 99.9%) and toluene ($C_6H_5CH_3$, 99.5%) were used without any further purification, as obtained from Sigma Aldrich, South Africa.

5.2.1. Sensing device fabrication

An N, N-dimethylformamide/ethylene glycol (1:1) dispersed solution (1 mg/mL) of the sensing material (Ni_3S_2, rGO, (5%) Ni_3S_2-rGO, (10%) Ni_3S_2-rGO or NS-rGO) was prepared by ultra-sonication for an hour followed by stirring for another hour. The dispersion was deposited on interdigitated gold electrodes by drop casting. Thereafter, the sensing material was allowed to dry in a fume hood at room temperature for a week and then placed under vacuum in a dessicator to remove any of the organic solvent from the sensing material. The five sensors were labelled as Sensor 1, 2, 3, 4 and 5 for sensors fabricated using Ni_3S_2, rGO, (5%) Ni_3S_2-rGO, (10%) Ni_3S_2-rGO and in situ prepared NS-rGO, respectively.

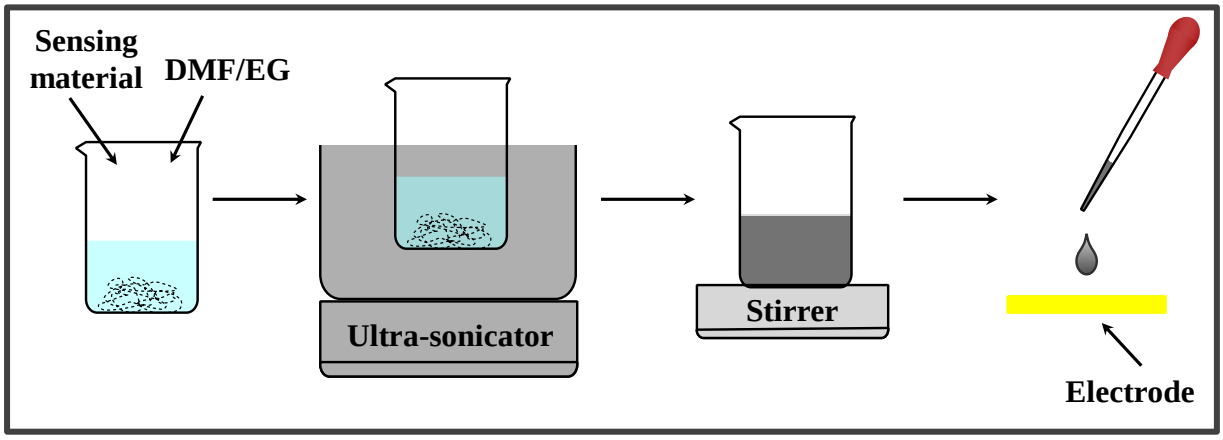

Scheme 5. 1. Preparation of sensing electrodes.

5.2.2. Gas sensing measurement setup and testing

The gas sensing properties of the fabricated sensing devices were studied by exposing the devices to the analytes (acetone, ethanol, toluene and methanol) and analysing the change in the electrical resistance. An ISOTECH LCR 821 LCR meter with an AC input signal was

employed for the electrical resistance measurements by applying a voltage of 0.5 V and a frequency of 25 kHz. **Fig. 5.1** gives a schematic representation of the sensing system used, where the sensing electrode was hosted inside a 20 L round bottom flask. The gas vapour of the different analytes was injected into the round bottom flask using a micro-syringe in volumes of 1, 2, 3, 4 and 5 μL at a time. The sensor was exposed to the analyte for 10 min after injection, thereafter the analyte was removed by vacuum suction at atmospheric pressure for 2 min and finally the sensor was allowed to recover for 3 min before the following volume injection.

The concentration of the analytes in ppm was calculated according to **Eq**. **5.1** [13]:

$$C_{(ppm)} = \frac{22.4\ \rho T V_s}{273 M_r V} \times 10^3 \qquad (5.1)$$

Where C is the concentration of the analyte gas in parts per million (ppm), ρ the density of the analyte in g·mL^{-1}, T the testing temperature in Kelvin (which was room temperature in this study), V_s the injected volume of the analyte in μL, M_r the molar mass of the analyte gas in g·mol^{-1}, and V the volume of the round bottom flask of 20 L.

In order to show the resistance change numerically, the sensor responses are reported as the resistance change between the response signal and the baseline ($\Delta R = R_{response} - R_{baseline}$).

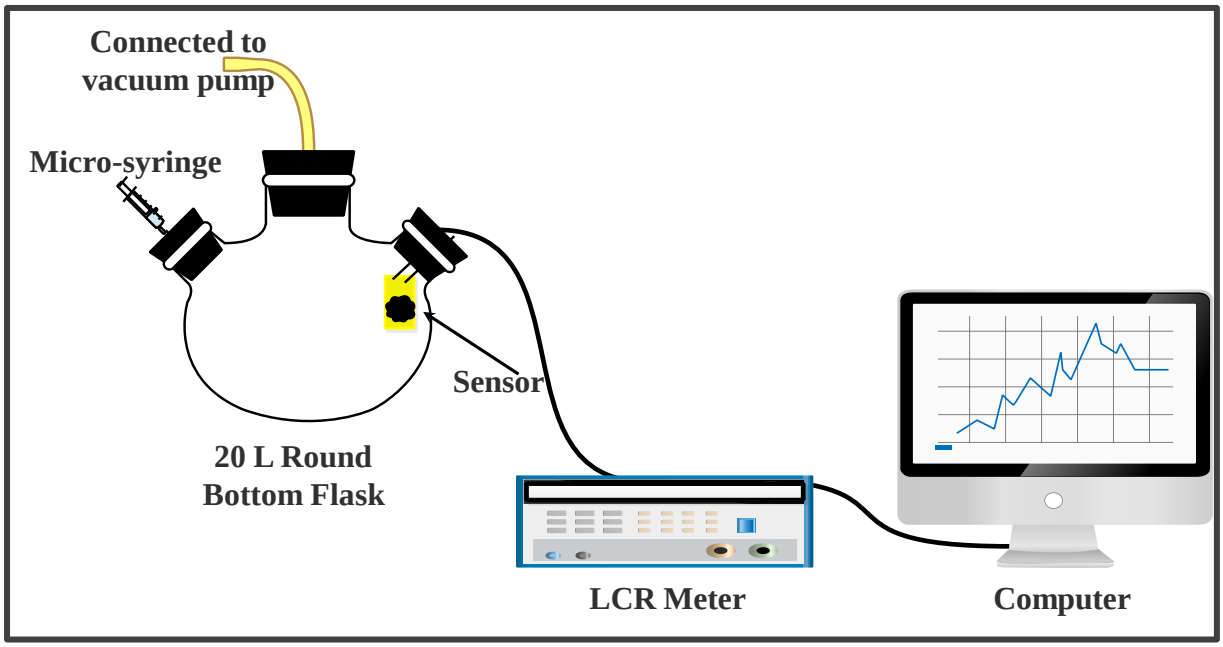

Figure 5. 1. Schematic of the gas sensing measurement setup.

5.3. Results and discussion

5.3.1. Gas sensing response

The fabricated sensors were all exposed to acetone, ethanol, methanol and toluene vapours at room temperature (25℃, RH 40%). Unfortunately, sensor 1 did not produce any noticeable change in response when exposed to any of the analytes giving only a signal with a large signal-to-noise ratio (Supplementary information, **Fig. S5.1**). **Fig. 5.2** shows the dynamic response curves of sensors 2-5 in ethanol gas. Sensor 3 produced dynamic response curves with the lowest signal-to-noise ratio for ethanol (**Fig. 5.2b**) and for all the other analytes. For all the sensors, as ethanol gas was injected into the round bottom flask an increase in ΔR was observed illustrating p-type sensing behaviour [16]. Sensor 2 (pure rGO) showed the highest change in resistance at 21 ppm ethanol exposure when compared to other sensors. However, the sensor did not show an increase in the ΔR signal with an increase in concentration but seemed to have reached saturation after the first injection of ethanol gas (**Fig. 5.2**a). Sensors 3-5 (composite materials where Ni_3S_2 is incorporated onto rGO) showed an increase in ΔR with an increase in ethanol concentration (**Fig. 5.2**b-d). **Figure 5.2**b shows that the (5%) Ni_3S_2-rGO composite (sensor 3) had the clearest increase in the ΔR with an increase in ethanol concentration when compared to the other composite materials.

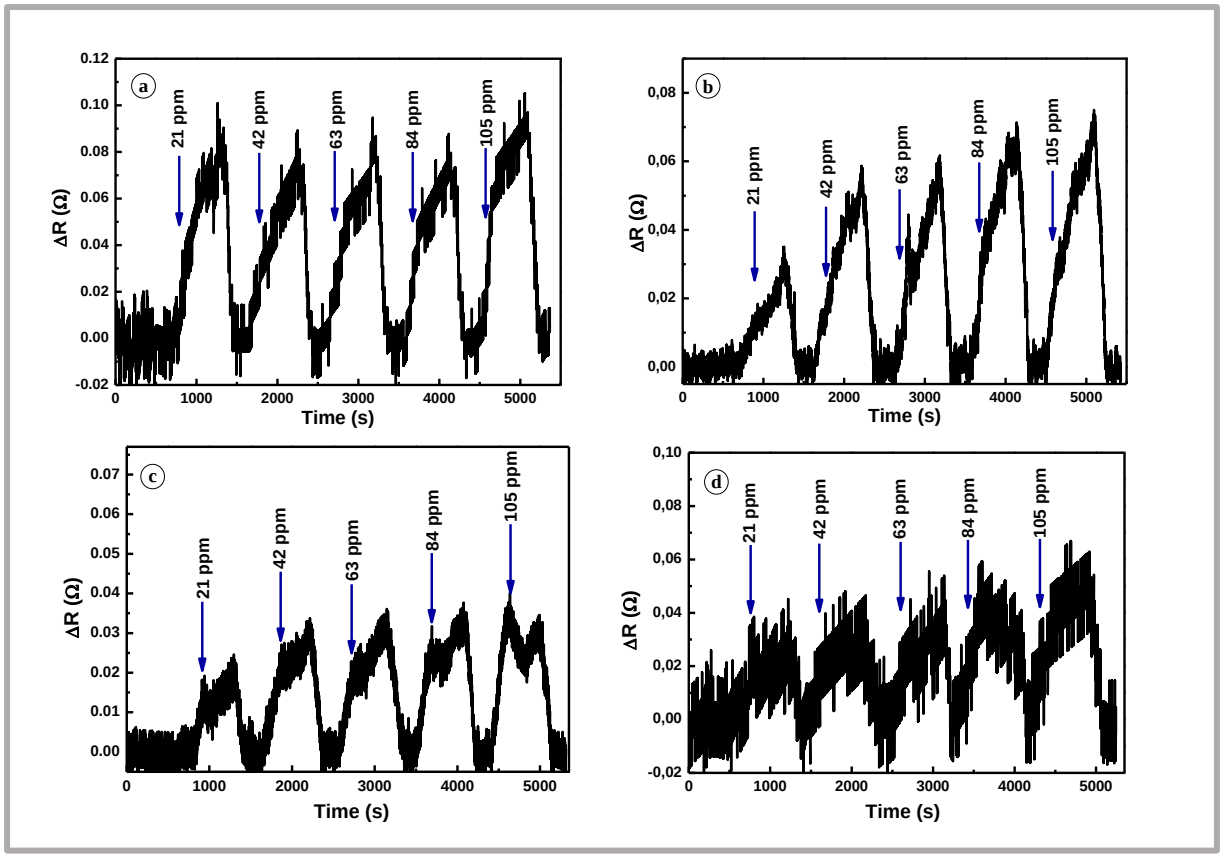

Figure 5. 2. Dynamic response curves in ethanol vapour for sensor 2 (a), sensor 3 (b), sensor 4 (c) and sensor 5 (d).

The sensor responses of the composites (sensors 3-5) for the first volume injections (**Fig. 5.3**) were lower than that of bare rGO (sensor 2) for most analytes (dynamic response curves for sensors in acetone, methanol and toluene (sensor 4&5) are found in supplementary information) implying that nickel sulfide hindered the rGO gas sensing reactions by reducing the contact probability of the analytes on the rGO. However, sensor 3 illustrated a higher response to toluene with the first two volume injections (**Fig. 5.4**b). The response of sensor 2 to toluene gas was only higher than sensor 3 after the third injection (**Fig. 5.4**a). This might be due to the dissociation energy of the analytes since the dissociation energy for toluene (376 kJ·mol^{-1}) is less than that of acetone (393 kJ·mol^{-1}), ethanol (436 kJ·mol^{-1}) and methanol (439 kJ·mol^{-1}). Sensor 3 showed a significant response to the first volume injection of toluene because during the adsorption process it released more electrons than the other analyte gases [17]. The decrease in the signal response with an increase in the concentration in toluene gas for sensor 3 could be attributed to the desorption ability of the gas on the surface of the sensor material. The presence of the Ni_3S_2 catalyst on the surface of rGO could possibly slow down the desorption process because of a stronger interaction with the toluene molecules.

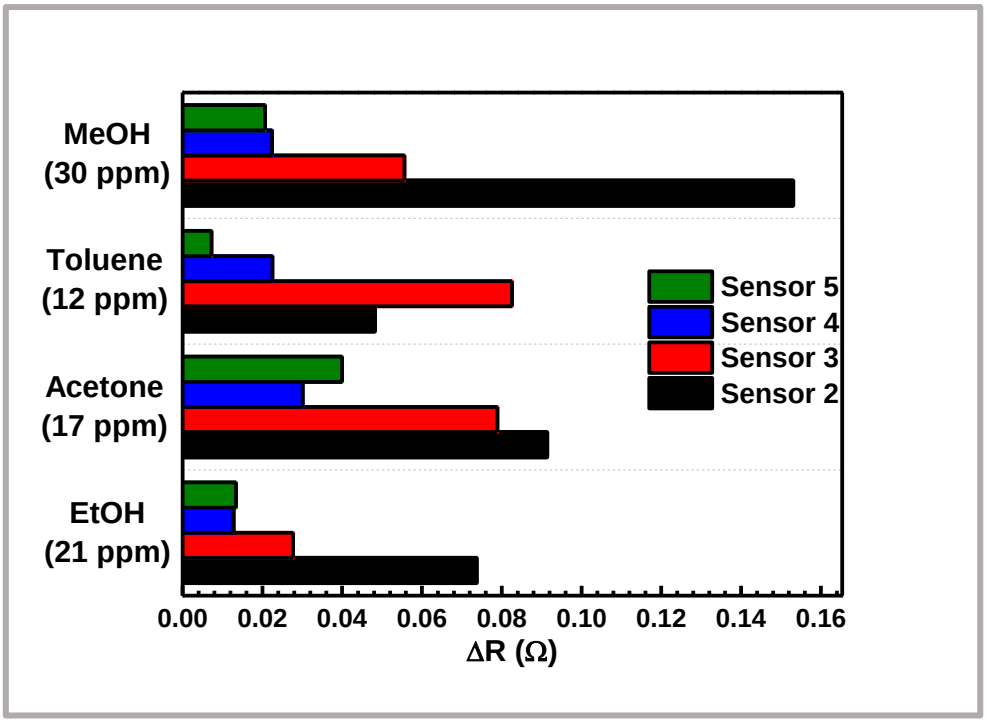

Figure 5. 3. Comparison of obtained responses of sensor 2-5 after injection of 1 μL of the analyte gases.

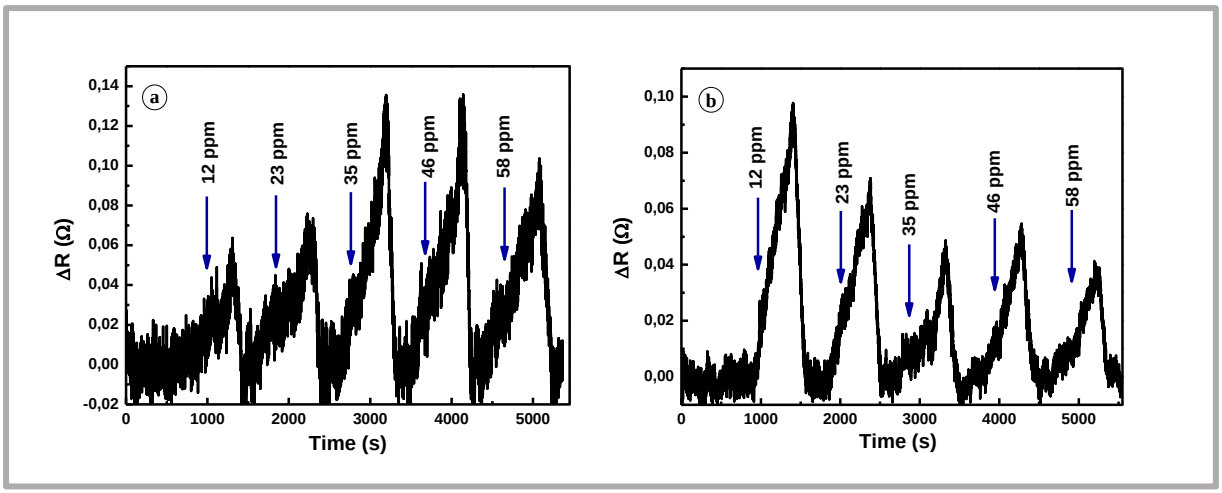

Figure 5. 4. Dynamic response curves of sensor 2 (a) and sensor 3 (b) to toluene gas.

5.3.2. Linearity and sensitivity

The high response of sensor 2 alone is not enough to conclude that it showed the best performance. A linear performance of a sensor with an increase in gas concentration also makes a sensor more reliable [16]. Sensor 2 did not show a consistent increase in the sensor response with an increase in the concentration of ethanol (**Fig. 5.2**a & **5.5**a) and thus resulted in a very low correlation coefficient, $\mathbf{R^2}$. Scattered points were also observed for acetone (**Fig. 5.5**b).

When exposed to toluene or methanol, the response decreased with an increase in concentration (**Fig. 5.5**c-d). This could be due to a strong adsorption of the analyte (toluene or methanol) molecules. The analyte molecules were not removed from the active sites when the gas was removed by vacuum possibly, implying poor recoverability. Even though methanol had a decreasing slope (**Fig. 5.5**d), it showed the best linear fit (the highest R^2).

Sensor 3 showed the most consistent (most linear) sensing performance with an increase in the analyte concentration for all the gases (**Fig. 5.6**a-d). However, just like sensor 2 for methanol and toluene, the ΔR for sensor 3 in acetone, methanol and toluene (**Fig. 5.6**b-d) decreased with an increase in gas concentration.

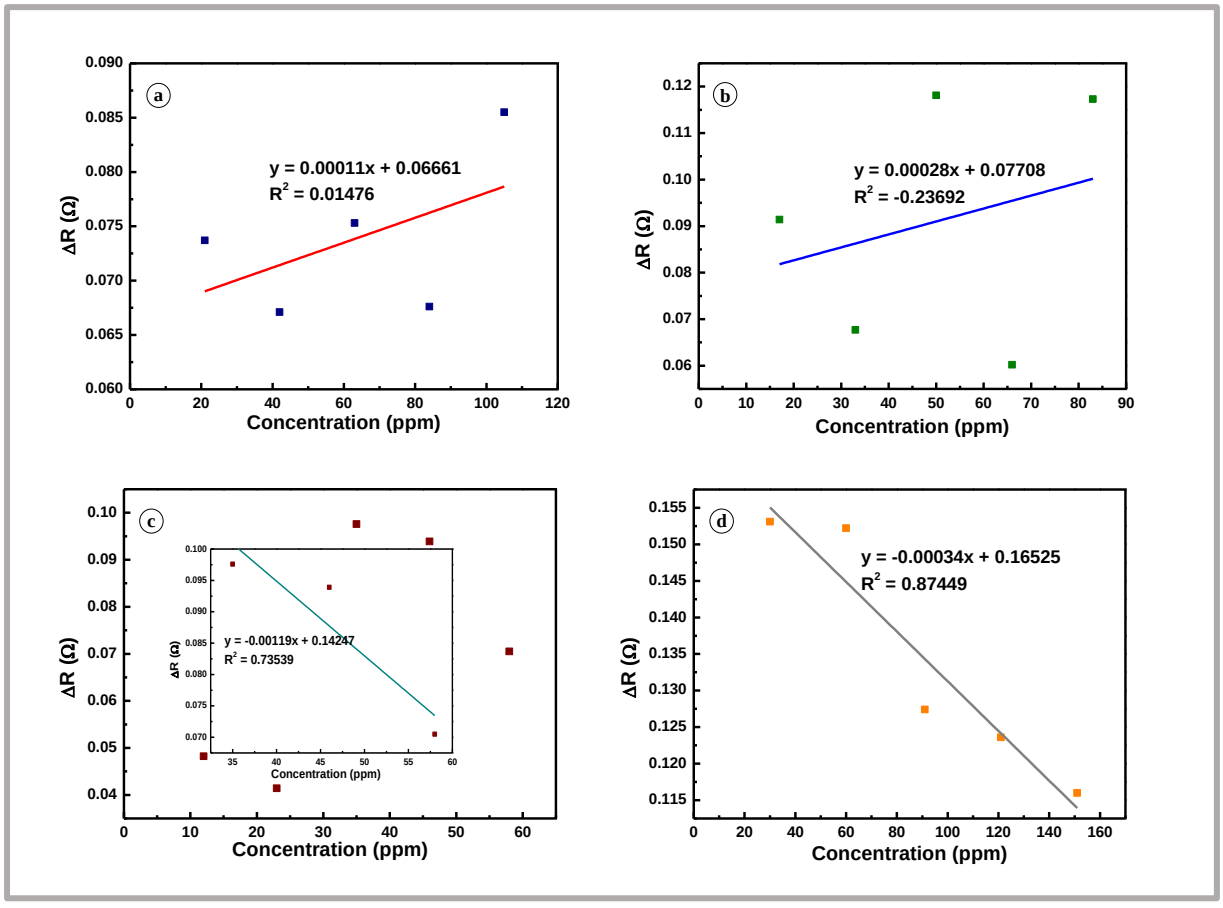

Figure 5. 5. ΔR vs concentration curves of sensor 2 in ethanol (a), acetone (b), toluene (c), and methanol (d) gas.

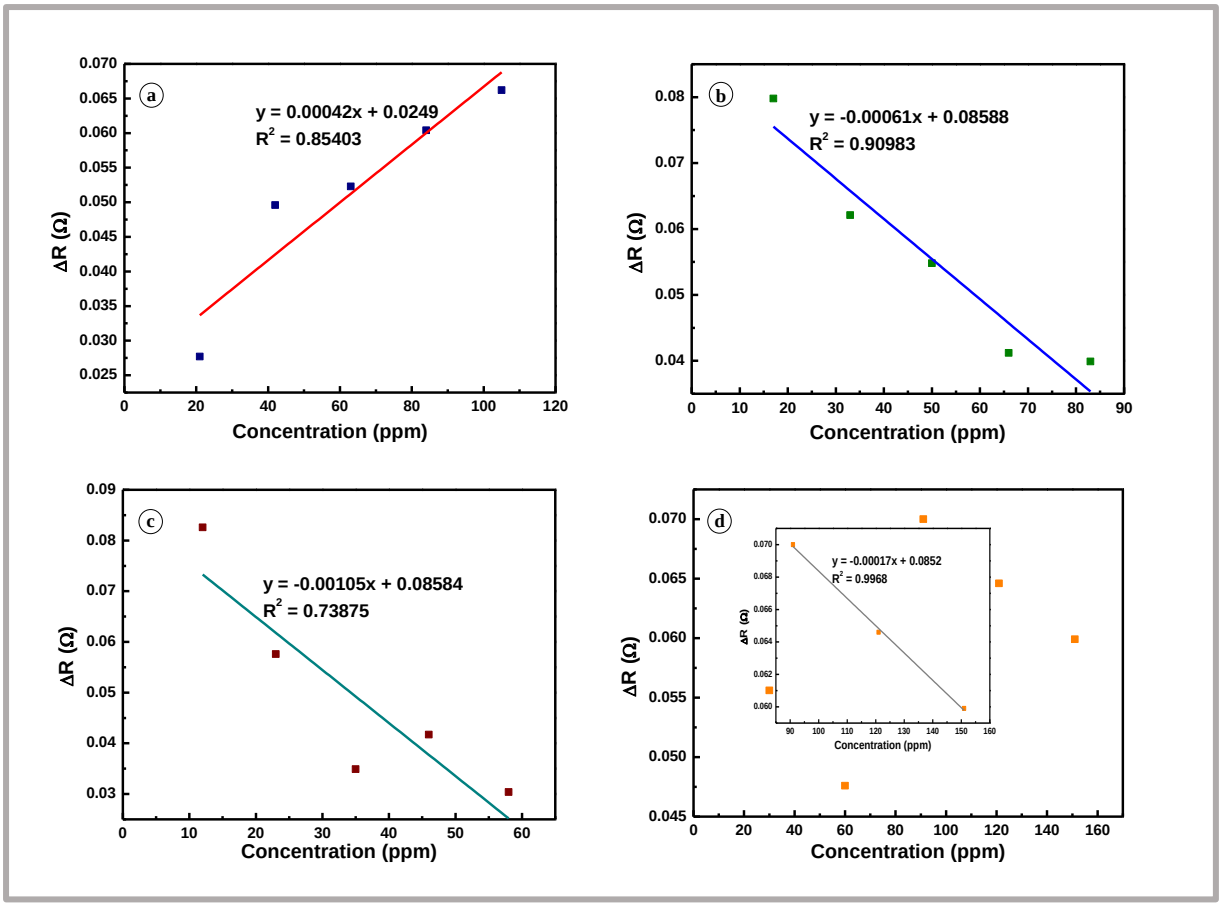

Figure 5. 6. ΔR vs concentration curves of sensor 3 in ethanol (a), acetone (b), toluene (c), and methanol (d) gas.

Another important characteristic property of sensors is sensitivity. Sensitivity can be defined as the lowest amount of gas that can be detected by the sensor [15]. The sensitivity of all the sensors towards ethanol gas was determined and is summarized in **Fig. 5.7**. According to the bar graph in **Fig. 5.7**, sensor 3 exhibited the highest sensitivity with a sensitivity of 0.00042 $\Omega \cdot ppm^{-1}$ followed by sensor 5 with a sensitivity of 0.00032 $\Omega \cdot ppm^{-1}$. Sensor 4 was the least sensitive to ethanol.

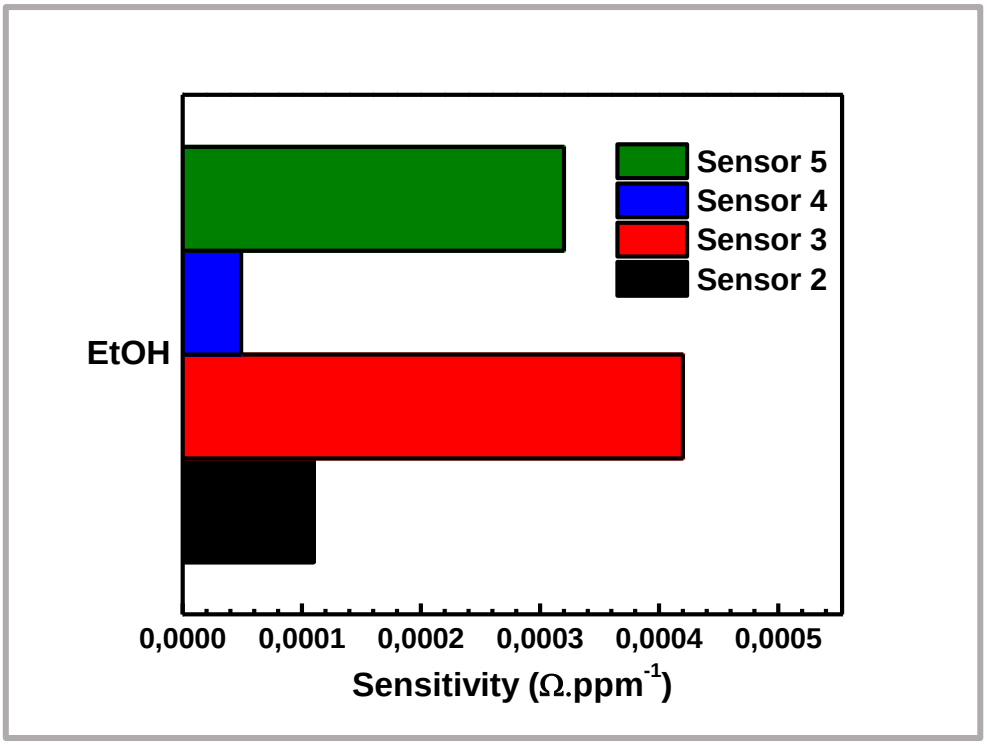

Figure 5. 7. Sensitivity of sensors to ethanol gas.

5.3.3. Response-recovery property

Also of importance, especially for practical applications, is the response and recovery times. The response time is usually defined as the period of time the sensors takes to reach 90% of the saturation response immediately after exposure to the gas, and the recovery time as the period required to recover to 90% of its initial response [15]. The response and recovery time for sensor 3 to a concentration of 105 ppm ethanol vapour was determined as 314 s and 129 s, respectively (**Fig. 5.8**). The response time was higher than the recovery time because desorption of ethanol molecules on the sensing material occurred much faster than adsorption.

Metal sulfides are rarely studied for the detection of VOCs while rGO has been used for sensing of VOCs in small percentages when combined with other materials (especially MOSs). There is thus few literature sources available to compare with this work. **Table 5.1** compares the work to recent studies by Huang [18] and Zolghadar [19] where they respectively employed NiS@In_2O_3 (7:3) and α-Fe_2O_3- rGO (3%) for ethanol sensing. The (5%) Ni_3S_2-rGO sensor showed longer response and recovery times than the ones reported in literature. However, the operating temperature was over 11 times lower than the operating temperatures of those reported sensors.

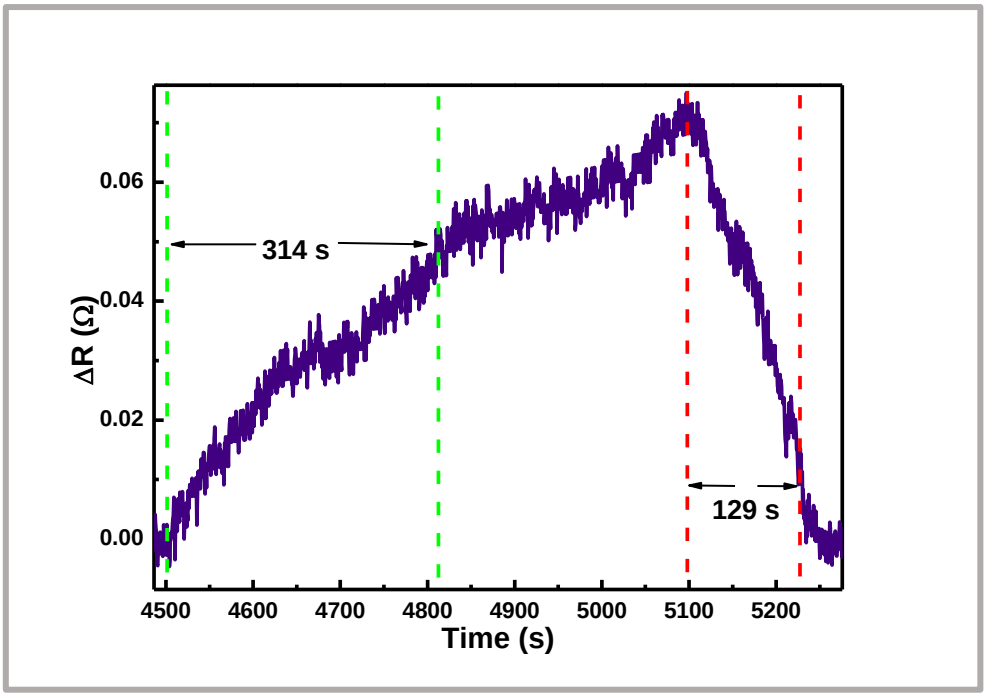

Figure 5. 8. Response and recovery time of sensor 3 to 105 ppm of ethanol gas.

Table 5. 1. Response-recovery properties of published ethanol sensors.

Materials	**Conc. (ppm)**	**Operating Temp. (℃)**	**Resp. (s)**	**Rec. (s)**	**Ref.**
NiS@In_2O_3 (7:3)	100	300	8	20	[18]
α-Fe_2O_3- rGO (3%)	100	280	9	12	[19]
(5%) Ni_3S_2-rGO	105	25	314	129	[This work]

5.3.4. Gas sensing mechanism

A material's characteristic surface properties determine the gas sensing mechanism. The surface modification of graphene and its derivatives with catalysts has shown to be a good approach in improving its sensing performance [20, 21]. Peng [20] decorated the surface of rGO with Pt and Pd nanoparticles for H_2 sensor fabrication. This sensor exhibited enhanced performance in terms of response, operating temperature and response and recovery times relative to pristine rGO. This was attributed to the catalytic activity of the two catalysts, which have a high reactivity and helped facilitate adsorption and desorption of the gas. In this study,

small percentages of the Ni_3S_2 catalysts were introduced to the surface of rGO to assist the surface reactions during sensing. However, to our knowledge there has not been any report in literature on its sensing mechanism.

Since rGO was the dominant material in sensor 3 ((5%) Ni_3S_2-rGO), the main conduction pathway can be due to the presence of the rGO sheets. rGO has been described as a p-type semiconductor [6, 19] meaning it has positive holes as majority charge carries. The exposure of a p-type semiconductor to atmospheric air below 300℃ allows the adsorbed molecular oxygen to be ionized to O^-, O^{2-} and O_2^- species (**Eq. 5.2-5.3**) [17]. When ethanol, a reducing gas, was adsorbed on the surface of the material, the ethanol molecules reacted with the adsorbed oxygen species to form CO_2 and H_2O (**Eq. 5.4-5.5**) [15]. The interaction of the ethanol molecules with the oxygen species adsorbed on the surface released electrons to the material, which became coupled to the holes (**Eq. 5.6**). A resultant decrease in the hole concentration consequently increased the sensor resistance.

$$O_{2\,(gas)} \rightleftharpoons O_{2\,(ads)} \quad (\mathbf{5.2})$$

$$O_{2\,(ads)} + 2e^- \rightleftharpoons 2O^-_{(ads)} + 2h^+ \quad (\mathbf{5.3})$$

$$CH_3CH_2OH_{(g)} \leftrightarrow CH_3CH_2OH_{(ads)} \quad (\mathbf{5.4})$$

$$CH_3CH_2OH_{(ads)} + 6O^-_{(ads)} \rightleftharpoons 2CO_2 + 3H_2O + 6e^- \quad (\mathbf{5.5})$$

$$h^+ + e^- \rightleftharpoons \text{null} \quad (\mathbf{5.6})$$

5.4. Conclusions

Sensors fabricated with Ni_3S_2, rGO, (5%) Ni_3S_2-rGO, (10%) Ni_3S_2-rGO and in situ prepared NS-rGO as active sensor materials were exposed to VOCs vapours. Pure nickel sulfide (sensor 1) did not produce a response when exposed to any of the tested VOCs. However, all the other materials were able to detect the gas vapours. Even though sensor 2 (rGO) showed the highest response to most analytes including ethanol, sensor 3 ((5 %) Ni_3S_2-rGO) produced the most linear dynamic response curves. Moreover, sensor 3 was the most sensitive to ethanol gas with a sensitivity of 0.00042 $\Omega \cdot ppm^{-1}$. The response and recovery time of sensor 3 in 105 ppm ethanol were found to be 314 s and 129 s, respectively. These results indicate that (5%) Ni_3S_2-rGO has the potential for sensing ethanol vapours at low operating temperature.

References

[1] Liang, X., Qin, Y., Xie, W., Deng, Z., Yang, C., Su, X., Journal of Alloys and Compounds **818** (2020) 152898.

[2] Mirzaei, A., Leonardi, S.G., Neri, G., Ceramic International **42** (2016) 15119-15141.

[3] Zito, C.A., Perfecto, T.M., Volanti, Sensors and Actuators B **244** (2017) 466 -474.

[4] Sinha, M., Mahapatra, R., Mondal, M.K., Krishnamurthy, S., Ghosh, R., Physica E **118** (2020) 113868.

[5] Zhang, C., Li, L., Hou, L., Chen, W., Sensors and Actuators B **291** (2019) 130-140.

[6] Modenes-Junior, M.A., Zito, C.A., Perfecto, T.M., Volanti, D.P., Materials Science & Engineering B **248** (2019) 114385.

[7] Van den Broek, J., Aegg, S., Pratsinis, S.E., Günter, A.T., Nature Communications **10** (2019) 4220.

[8] Kawamura, K., Vestergaard, M., Ishiyama, M., Nagatani, N., Hashiba, T., Tamiya, E., Measurement **39** (2006) 490- 496.

[9] Rodner, M., Puglisi, D., Ekeroth, S., Helmersson, U., Shtepliuk, I., Yakimova, R., Skallberg, A., Uvdal, K., Schütze, A., Eriksson, J., Sensors **19** (2019) 918.

[10] Park, H., Lee, E., Chung, Y., Lee, S., Ahn, H., Kim, D.J., ECS Transactions **69** (2015) 41-45.

[11] Kwon, Y.J., Na, H.G., Kang, S.Y., Choi, S.W., Kim, S.S., Kim, H.W., Sensors and Actuators B **227** (2016) 157-168.

[12] Zhou, Y., Jiang, Xie, G., Du, X., Tai, H., Sensors and Actuators B **191** (2014) 24-30.

[13] Kim, S. Lee, S.H., Lee, Y., Biosensors and Bioelectronics **85** (2016) 587- 595.

[14] Linganiso, E.C., Linganiso, Z.L., Motaung, T.E., Singh, T., Fischer, T., Mathur, S., Mhlanga, S.D., Mwakikunga, B.W., Coville, N.J., 2019 IEEE SENSORS, Montreal, QC, Canada (2019) 1-4.

[15] Olifant, G.E., Mavumengwana, V., Hümmelgen, I.V., Mamo, M.I.A., Journal of Materials Science: Materials in Electronics **30** (2019) 3552- 3562.

[16] Kuchi, P.S., Roshan, H., Sheikhi, M.H., Journal of Alloys and Compounds **816** (2020) 152666.

[17] Hussain, S., Liu, T., Javed, M.S., Aslam, N., Zeng, W., Sensors and Actuators B **239** (2017) 1243- 1250.

[18] Huang, X.Y., Chi, Z.T., Liu, J., Li, D.H., Sun, X.J., Yan, C., Wang, Y.C., Li, H., Wang, X.D., Xie, W.F., Sensors and Actuators B **304** (2020) 127305.

[19] Zolghadr, S., Kimiagar, S., Khojier, K., Journal of Electronic Materials **46** (2017) 6834 - 6842.

[20] Peng, Y., Ye, J., Zheng, L., Zou, K., RSC Advances **6** (2016) 24880-24888.

[21] Lu, X., Sing, X., Gu, C., Ren, H., Sun, Y., Huang, J., Journal of Physics and Chemistry of Solids **116** (2018) 324-330.

Chapter 6: Concluding remarks and recommendations

6.1. Conclusions

Nickel sulfide-reduced graphene oxide composites have been previously studied for their potential application in energy storage devices, but rarely in sensing applications. The main aim of this study was to produce Ni_3S_2–reduced graphene oxide composites for their potential application in chemiresistive gas sensing devices. The following conclusions were drawn from this study:

Rhombohedral Ni_3S_2 nanostructures were synthesized using a facile microwave-assisted technique. The influence of different solvent compositions of water, ethanol and ethylene glycol on the chemical and physical properties were evaluated. Nanostructures synthesized in ethanol or mixture of ethanol and water did not have a pure phase purity, however when only water and/or ethylene glycol was used, flowerlike Ni_3S_2 nanostructures with a high phase purity were obtained. The effect of post-thermal annealing on the phase purity, crystalline size and morphology has also been reported. Annealing in a hydrogen atmosphere at 300℃ produced highly crystalline Ni_3S_2 structures with rod-like flowers. An increase in the annealing temperature caused a phase transition and produced quasi-spherical nanostructures.

The use of a microwave reduction technique for GO reduction was investigated. GO reduced only under MW irradiation produced rGO with a comparable defect density with the GO sample reduced with hydrazine hydrate. Ascorbic acid had a lower defect density. All the MW reduced samples had an interlayer spacing of 0.37 nm and the in-plane crystal sizes ranged from 6 to 7 nm. The rGO sheets in the control sample were smaller in diameter and appeared to be more agglomerated. XPS results revealed that the hydrazine reduced sample had a C/O ratio of 7.8:1 and that nitrogen species were incorporated into the structure.

Different nickel-sulfide reduced graphene oxide composites were synthesized in situ and ex situ. The in situ prepared sample consisted of quasi-spherical nickel sulfide (NiS and Ni_3S_2) embedded on rGO sheets, whereas the composites synthesized by physically mixing Ni_3S_2 and rGO had a 2D morphology. XPS, XRD and FTIR results further confirmed the formation of the composites.

Furthermore, the study of Ni_3S_2, rGO and nickel sulfide-reduced graphene oxide composites as volatile organic compounds sensing material was reported. The (5 %) Ni_3S_2-rGO composite

showed superior sensing behaviour towards the tested analytes (acetone, ethanol, toluene and methanol). However, it exhibited a linear response with good recoverability only in ethanol gas. The composite also had the best sensitivity towards ethanol gas when compared to the other sensors with a response/recovery speed of 314 s/129 s.

6.2. Recommendations

The application of Ni_3S_2 and NS-rGO composites in chemiresistive gas sensing devices still need pursuing and to ensure that they are exploited to maximum capacity, the following can be investigated:

- Temperature studies could help establish the sensing performance of Ni_3S_2. Additionally, testing the Ni_3S_2 nanostructures synthesized using different solvents could show the influence of the solvents on the sensing performance of Ni_3S_2.
- Testing the ethanol response of the (5%) Ni_3S_2-rGO sensor in dry air and at higher RH could help in determining the effect of humidity on its sensing performance. Moreover, the development of filters or mathematical processing methods could be investigated to compensate for the influence of humidity.
- Researchers have investigated different strategies for the improvement of room temperature sensing devices. Light illuminations is one of the techniques that have shown promising results in improving the recoverability of sensing material by promoting desorption of gas molecules from the surface of the material. It could be interesting to study the influence of photoluminescence on the recovery of the (5%) Ni_3S_2-rGO sensor after sensing acetone, toluene and methanol.
- To check the stability and practicality of the (5%) Ni_3S_2-rGO sensor, comparing the response of a freshly prepared sensor and a sensor that has been exposed to different concentrations of ethanol gas in ambient air for one year could be useful.
- Finally, the ethanol gas sensing mechanism could be verified by analysing the sensing material with XRD, Raman, FTIR and XPS techniques after ethanol adsorption. The effect of ethanol adsorption and desorption on the morphology of the sensing material could also be interesting.

Supplementary Information

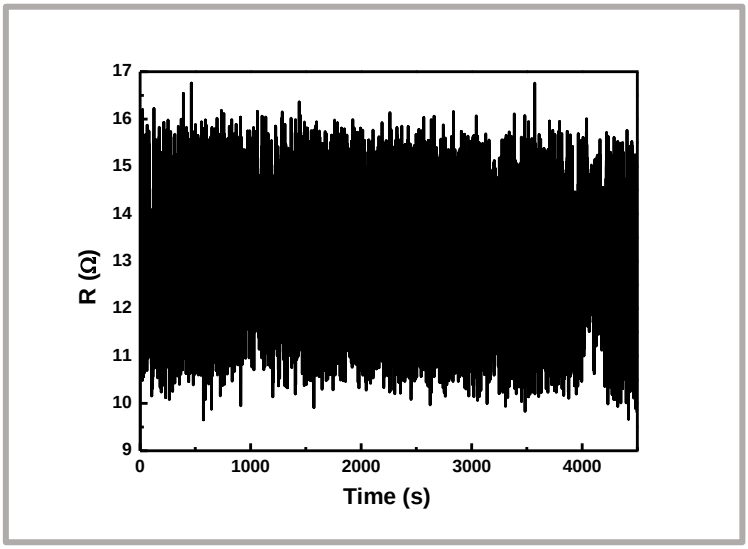

Figure S5. 1. Dynamic response curve for sensor 1 in ethanol gas.

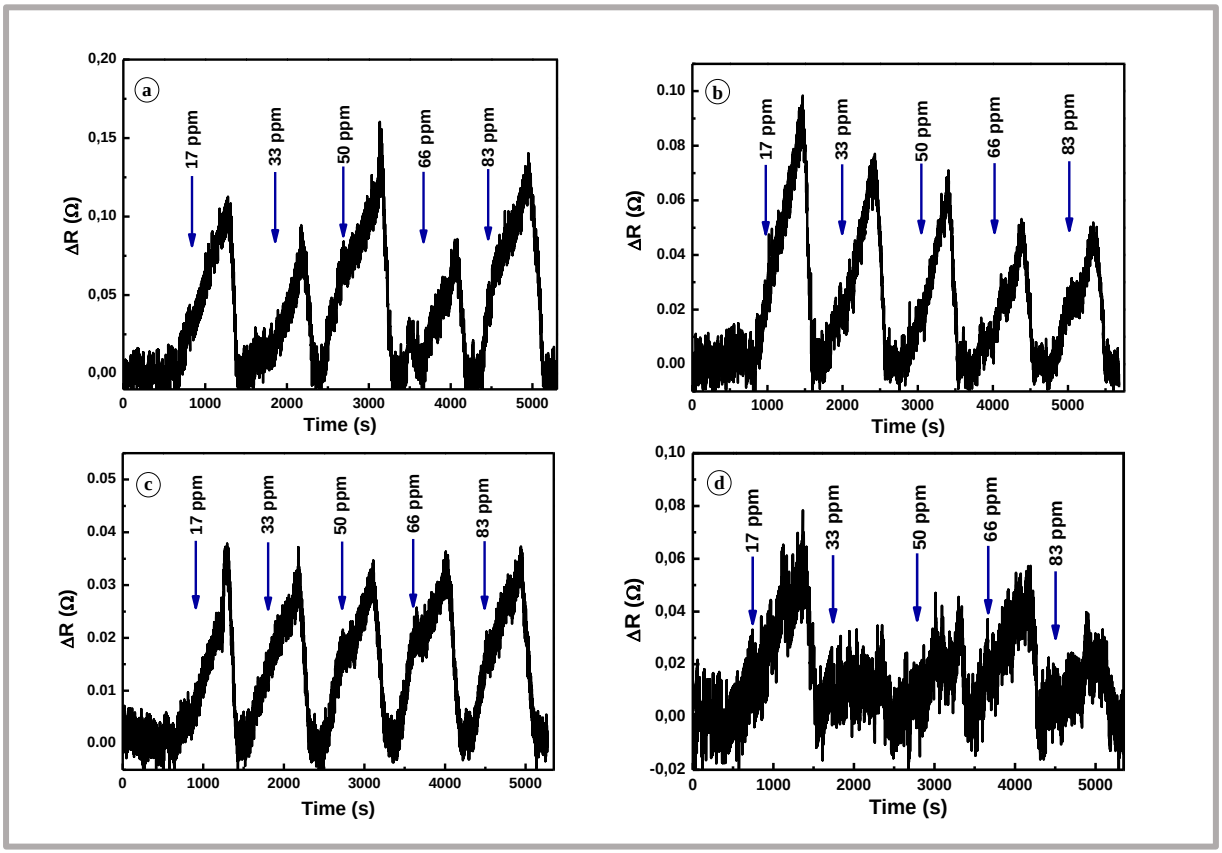

Figure S5. 2. Dynamic response curve for sensor 2 (a), sensor 3 (b), sensor 4 (c), and sensor (d) in acetone gas.

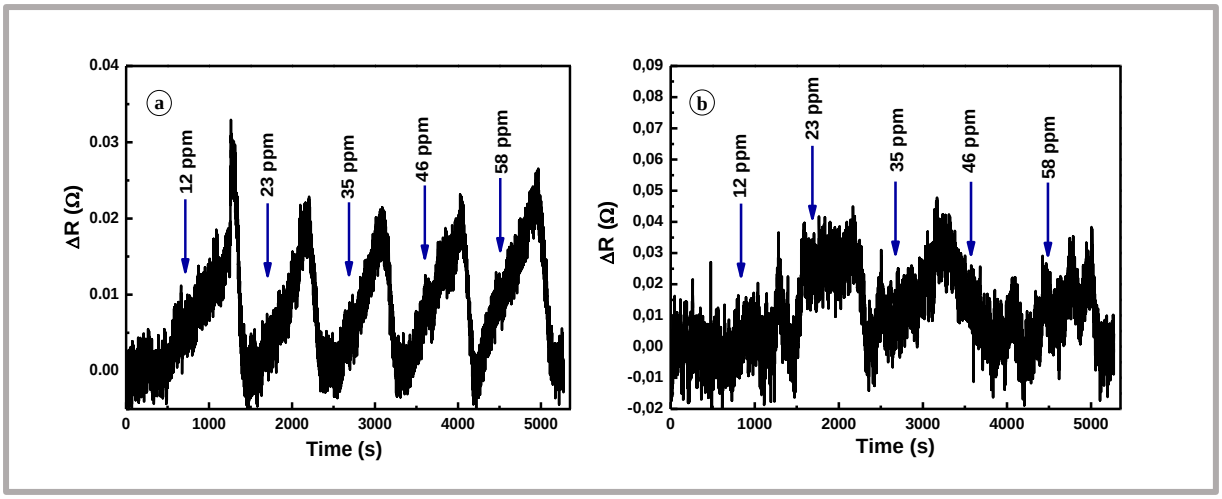

Figure S5. 3. Dynamic response curve for sensor 4 (a) and sensor 5 (b) in toluene gas.

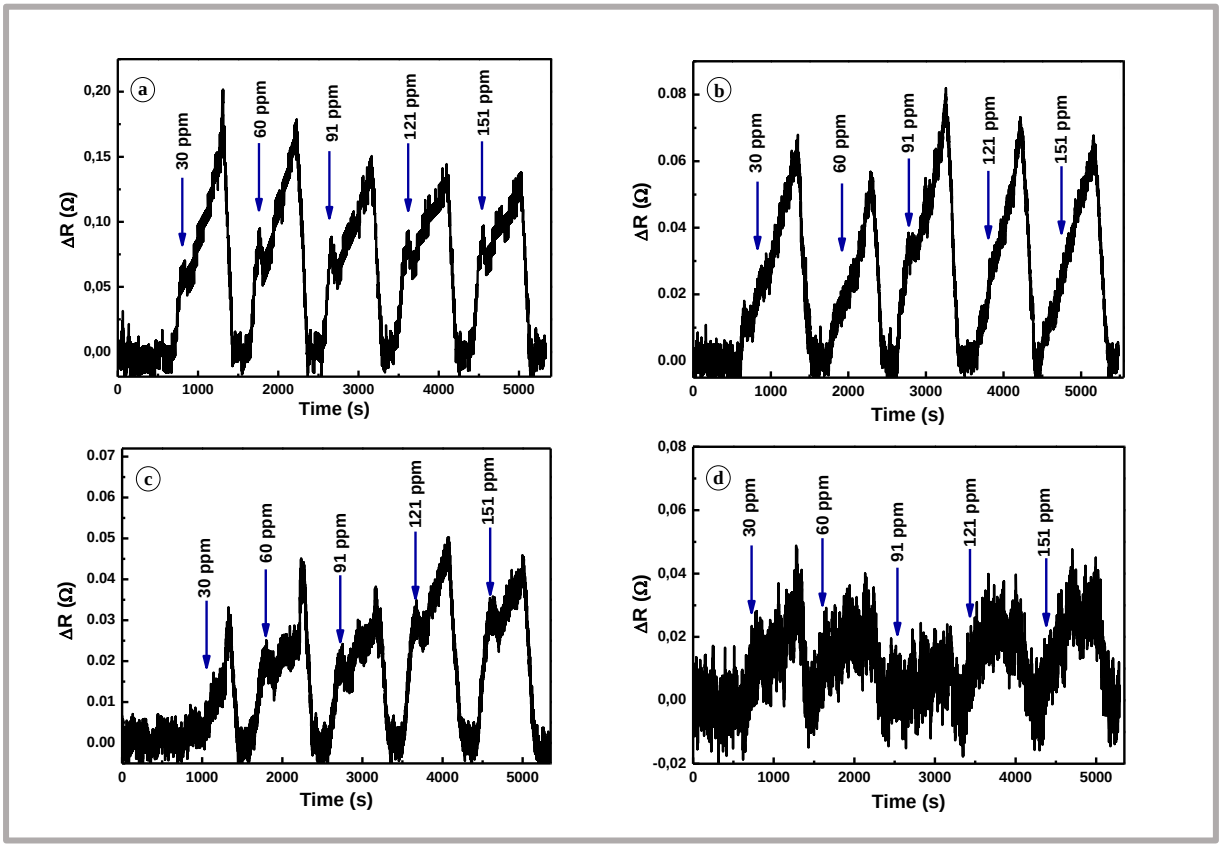

Figure S5. 4. Dynamic response curve for sensor 2 (a), sensor 3 (b), sensor 4 (c), and sensor (d) in methanol gas.